Title
Micro/Nano-Scale Phase Change Systems for Thermal Management and Solar Energy Conversion Applications

Author
Coso, Dusan

Publication Date
2013

Peer reviewed|Thesis/dissertation

Micro/Nano-Scale Phase Change Systems for Thermal Management and Solar Energy Conversion Applications

By

Dusan Coso

B.S. (University of California Berkeley) 2007

M.S. (University of California Berkeley) 2009

A dissertation submitted in partial satisfaction of the

requirements for the degree of

Doctor of Philosophy

in

Engineering – Mechanical Engineering

in the

Graduate Division

of the

University of California, Berkeley

Committee in charge:

Professor Van P. Carey, Chair

Professor Costas Grigoropoulos

Dr. Arun Majumdar

Professor Rachel Segalman

Spring 2013

Micro/Nano-Scale Phase Change Systems for Thermal Management and Solar Energy Conversion Applications

by

Dusan Coso

Abstract

Micro/Nano-Scale Phase Change Systems for Thermal Management and Solar Energy Conversion Applications

by

Dusan Coso

Doctor of Philosophy in Engineering – Mechanical Engineering

University of California, Berkeley

Professor Van P. Carey, Chair

The first part of the dissertation presents a study that implements micro and nano scale engineered surfaces for enhancement of evaporation and boiling phase change heat transfer in both capillary wick structures and pool boiling systems. Capillary wicking surfaces are integral components of heat pipes and vapor chamber thermal spreaders often used for thermal management of microelectronic devices. In addition, pool boiling systems can be encountered in immersion cooling systems which are becoming more commonly investigated for thermal management applications of microelectronic devices and even data centers. The latent heat associated with the change of state from liquid to vapor, and the small temperature differences required to drive this process yield great heat transfer characteristics. Additionally, since no external energy is required to drive the phase change process, these systems are great for portable devices and favorable for reduction of cost and energy consumption over alternate thermal management technologies.

Most state of the art capillary wicks used in these devices are typically constructed from sintered copper media. These porous structures yield high surface areas of thin liquid film where evaporation occurs, thus promoting phase change heat transfer. However, thermal interfaces at particle point contacts formed during the sintering process and complex liquid/vapor flow within these wick structures yield high thermal and liquid flow resistances and limit the maximum heat flux they can dissipate. In capillary wicks the maximum heat flux is typically governed by the capillary or boiling limits and engineering surfaces that delay these limitations and yield structures with large surface areas of thin liquid film where phase change heat transfer is promoted is highly desired. In this study, biporous media consisting of microscale pin fins separated by microchannels are examined as candidate structures for the evaporator wick of a vapor chamber heat pipe. Smaller pores are used to generate high capillary suction, while larger microchannels are used to alleviate flow resistance. The heat transfer coefficient is found to depend on the area coverage of a liquid film with thickness on the order of a few microns near the meniscus of the triple phase contact line. We manipulate the area coverage and film thickness by varying the surface area-to-volume ratio through the use of microstructuring. In some samples, a transition from evaporative heat transfer to nucleate boiling is observed. While it is difficult to identify when the transition occurs, one can identify regimes where evaporation dominates over nucleate boiling and vice versa. Heat fluxes of 277.0 (± 9.7) W/cm^2 can be dissipated by wicks with heaters of area 1 cm^2, while heat fluxes up to 733.1 (± 103.4) W/cm^2 can be dissipated by wicks with smaller heaters intended to simulate local hot-spots.

In pool boiling systems that are encountered in immersion cooling applications, the heat transfer coefficient (HTC) is governed by the bubble nucleation site density and the agitation in the liquid/vapor flow these bubbles produce when they detach from the surface. The nucleation site density and release rate is usually determined by the surface morphology. Another important parameter in pool boiling systems is the maximum heat flux (CHF) that can safely be dissipated. In practice, this quantity is about two orders of magnitude smaller than limitations suggested by kinetic theory. For essentially infinite, smooth, well wetted surfaces, hydrodynamic instability theories capturing liquid/vapor interactions away from the heated surface have been successful in predicting CHF. On finite micro and nano structured surfaces where applying the hydrodynamic theory formulation is not easily justified, other effects may contribute to phase change heat transfer characteristics. Here, we also present a pool boiling study on biporous microstructured surfaces used in capillary wick experiments. Structures are manipulated by reduction of pore size to determine if increased capillary pressure can enhance rewetting from heater edges and delay CHF. A comparative study between the two experimental systems indicates that while the capillary limitation is significant in capillary wick experiments, for these well wetted microstructured surfaces used in pool boiling systems the hydrodynamic limitation defined based on heater size causes the occurrence of CHF. Other hierarchical nanowire surfaces containing periodic microscale cavities are investigated as well and are seen to yield a ~2.4 fold increase in heat transfer coefficient characteristics while not compromising CHF compared to surfaces where cavities are not present. These studies indicate pathways for enhancement of heat transfer coefficient via implementing hierarchical structures, while no clear method in increasing CHF is determined for finite size surfaces of various morphologies.

In the second part of this dissertation, solar energy storage is sought in ‘phase change’ of photochromic molecular systems: the storage of solar energy in the chemical bonds of photosensitive molecules (a photochemical reaction) and subsequent recovery of the energy in a back reaction in the form of heat, reversibly. These molecular systems are interesting alternatives to photovoltaic and solar thermal technologies which cannot satisfy the needs of load leveling, or for portable municipal heating applications. Typically made of organic compounds, these molecules have become known for rapid decomposition, short energy storage time scales and poor energy storing efficiencies. Thus, they have been abandoned as practical solar energy storage systems in the past several decades. On the other hand, organometallic molecular systems have not been extensively probed for these applications. Recent research has indicated that organometallic (fulvalene)diruthenium $FvRu_2$ has demonstrated excellent energy storage characteristic and durability. Here, we report on a full cycle molecular solar thermal (MOST) microfluidic system based on a bis(1,1-dimethyltridecyl) substituted derivative of $FvRu_2$ that allows for long term solar energy storage (110 J/g), and “on demand” energy release upon exposure to a catalyst. The microfluidic systems developed here are excellent for photoconversion characterization and scrutinizing potential catalysts and can be extended to studying many other molecular systems. The objective of the work presented here is to demonstrate that “on demand” solar energy storage and release in MOST systems is viable and motivate future research on other photochromic organometallic systems.

Dedicated to my late brother Nebojša
Some things in life are getting better, but nothing will ever be the same…

Table of Contents

List of Figures

List of Tables

Nomenclature

A	Surface area of a plane structure or projected into a 2-D plane (m^2)
b	Cylindrical heat pipe radius (m)
c_l	Specific heat of the liquid (J/kg-K)
c_{solu}	Specific heat of solute (J/kg-K)
c_{solv}	Specific heat of solvent (J/kg-K)
C	Circumference (m)
CHF	Critical heat flux (W/m^2)
d	Pin fin diameter (m)
d_c	Rectangular/reentrant cavity mouth size (m)
D	Width of periodic pin fin array (m)
D_b	Secondary bubble departure diameter (m)
D_c	Rectangular/reentrant cavity depth from top of nanowires to the cavity base (m)
E_a	Energy barrier (J)
$\dot{e}$	Energy storage rate per unit area (W/m^2)
f	Frequency (Hz.)
f_B	Bubble bursting requency (Hz.)
g_{film}	Conductance of liquid film (W/m^2-K)
G_e	Gibbs free energy at equilibrium (J)
G_f	Gibbs free energy of the final state (J)
G_o	Gibbs free energy of the initial state (J)
h	Heat transfer coefficient 'HTC' (W/m^2-K)
h_{cap}	Capillary rise height (m)
h_{conv}	Free convection heat transfer coefficient (W/m^2-K)
HTC	Heat transfer coefficient (W/m^2-K)
H	Height of pin fins (m)
H_{nw}	Height of nanowires (m)
H_b	Height of vapor bubble (m)
$\hat{H}_A$	Hamacker Constant (Nm)
$\Delta H_{storage}$	Storage enthalpy in chemical bonds of photoisomer (J/kg)
$\Delta \hat{H}_{storage}$	Storage enthalpy in chemical bonds per mol of photoisomer (J/mol)
k	Thermal conductivity (W/m-K)
k_{epoxy}	Thermal conductivity of the thermal epoxy (W/m-K)
k_{Si}	Thermal conductivity of silicon (W/m-K)
l	Micropillar pitch (m)
L	Flow length (m)
L_b	Bubble length scale characteristic (m)
L_c	Capillary length scale (m)
L_{film}	Length of thin film surrounding each pin fin (m)
m	Mass of a single molecule (kg)
$\dot{m}$	Mass flow rate (kg/s)
m''	Mass flux rate (kg/m^2-s)
m_{solu}	Mass of solute (kg)
m_{solv}	Mass of solvent (kg)
M	Molar mass (kg/mol)

$\dot{M}$	Molar conversion rate (mol/s)
n	Number of moles
n_a	Nucleation site density (m^{-2})
N	Number of particles in the system considered
Nu	Nusselt number
Pr	Prandtl number
P	Pressure (N/m^2)
p	Pore size – pin fin spacing (m)
p_c	Pitch of cavities in a squre lattice ($p_c = d_c + s_c$) (m)
q	Heat flux (W/m^2)
Q	Heat flow adjusted for heat losses (W)
Q_{inp}	Heat generated via power supply (W)
Q_{loss}	Total measured heat loss by any means other than phase change heat transfer (W)
r_b	Bubble radius (m)
$r_{b,e}$	Equilibrium bubble radius (m)
$r_{b,max}$	Bubble radius at departure (m)
$r_{cav,max}$	Maximum cavity mouth radius (m)
$r_{cav,min}$	Minimum cavity mouth radius (m)
R	Thermal resistance (K/W)
R_{ad}	Thermal resistance of the adiabatic section of the heat pipe (K/W)
R_{conv}	Convective thermal resistance (m^2-K/W)
R_{film}	Thermal resistance of the liquid film (m^2-K/W)
R_{int}	Thermal resistance of the liquid/vapor interface (m^2-K/W)
R_L	Thermal resistance of the liquid filling the wick (m^2-K/W)
R_{matrix}	Thermal resistance of the solid liquid matrix (m^2-K/W)
R_{pins}	Thermal resistance of the solid pin fins of the wick (m^2-K/W)
$R_{substrate}$	Thermal resistance of the substrate (m^2-K/W)
Re	Reynolds number
$\acute{R}$	Electrical resistance (ohm)
$\hat{R}$	Specific gas constant (kJ/kg-K)
$\check{R}$	Ideal gas constant (kJ/mol-K)
s_c	Rectangular/reentrant cavity square lattice array spacing (m)
S-L-V	Solid-liquid-vapor three phase interface
t	Thickness (m)
t_{wafer}	Thickness of the silicon wafer (m)
T	Temperature (K)
$T_{substrate}$	Temperature of the substrate (K)
T_{vap}	Temperature of the vapor at saturation pressure (K)
T_{wall}	Temperature of the pin array base in contact with the liquid (K)
$\Delta T_{adiabatic}$	Adiabatic temperature rise (K)
u	Velocity scale (m/s)
u_c	Critical vapor velocity scale (m/s)
U	Uncertainty
v	Specific volume (m^3/kg)
$\bar{v}$	Average velocity scale (m/s)
v	Velocity scale (m/s)

w	Width of microchannel (m)
W	Wick edge length based on heater size (m)

Greek symbols

α	Accommodation coefficient
β	Exponent in the definition of disjoining pressure
γ	Ratio of actual surface area of a rough surface to its projected 2-D area
δ	Liquid film thickness surrounding a pin fin (m)
η	Roundtrip efficiency of the MOST system
η_{cat}	Photochrome efficiency
η_{he}	Heat exchanger efficiency
η_{pc}	Efficiency of the catalitically triggered reaction
θ	Apparent equilibrium contact angle (deg)
Θ	Temperature difference between two media (K)
κ	Permeability (m^2)
λ	Wavelength (m)
μ	Chemical potential
μ	Dynamic viscosity (Ns/m^2)
ρ	Density (kg/m^3)
σ	Surface tension (N/m)
ϕ	Wick porosity
ϕ_{flow}	Porosity of the flow cross section
Ω	Angle of inclination

Subscripts

ad	Adiabatic heat pipe section
α /a	Apparent property (e.g. contact angle)
cap	Capillary
cn	Condenser heat pipe section
d	Disjoining pressure
ev	Evaporator heat pipe section
eff	Effective
i	Counting incriment
int	Interface
lv	Liquid-vapor interface
l	Liquid
m	Modulation – geometry defined length scale related to wavelength
meas	Implies measured property
sat	Saturation conditions
surface	Projected surface in a 2-D plane
sl	Solid-liquid interface
sv	Solid-vapor interface
th	Subscript on an increment symbol
v	Vapor
vc	Vapor column
w	Wall

Acknowledgements

My experience as a graduate student here at University of California at Berkeley definitely had its ups and downs. The most striking experience was the passing of my brother Nebojša midway through 2009. This was an extremely difficult experience that permanently changed me in many ways, shattered my confidence, and made me feel that I would not complete many of my goals, one of those being this PhD dissertation. Without the support of many people, I am certain that I would not have the mental strength to be able to complete any of this work. I have tremendous appreciation for their help and support, not only on the academic level, but also on a personal level for helping me become stronger and in dealing with tough times.

First I would like to thank my brother Nebojša who always supported me and encouraged me to pursue my dreams and be involved in things that will keep me happy, be it related to work, research, sports or any other life style choice. His passing left a huge void in my life, but I will always look up to him and remember him for all the good times we shared. I would also like to thank my parents for always supporting and encouraging me, and especially for staying strong in the past several years. Sometimes I feel they suppress their emotions only to show me that we have to stay strong and move forward. I have great admiration for their courage and will. I would also like to thank my fiancé Neda who has been my main pillar over the last 3-4 years. She has absorbed a lot of my sadness, stress and frustration, and managed to stay positive and keep me as positive as possible through these years. Her support has been unconditional, be it related to personal matters or matters related to work and research. I would also like to thank her family for always being supportive, and always so optimistic.

In addition to my family members I would also like to thank my advisors, my co-workers, collaborators, and all other friends and family. Firstly, I would like to thank my advisor Arun Majumdar who has been very understanding, always encouraged me to try new things and "dig deeper" in both engineering and scientific aspects, and supported my progression through grad school. I am grateful that he took the risk to take me on as one of his students and to mentor me, and for making sure that I will be able to complete this graduate school experience with full moral and financial support. Since his ME109 class I attended, I have tried my best to absorb much of his knowledge, his optimism on every level, and his style of lecturing and presenting, and know that they will serve as critical components of my future endeavors.

I would also like to thank all of my lab members who have also given me a great deal of support on many different levels during my graduate studies. Working at UC Berkeley we are sometimes spoiled and do not realize that we are surrounded by so many smart and capable people. A lot of my lab members and collaborators deserve my most sincere praise and appreciation. I would first like to thank Kedar Hippalgaonkar and Jae Hun Seol. They have been not only good lab members but also good friends in good and bad times in and out of lab. I will always appreciate our discussions related to research and life in general and all the hard work we did together. I would also like to thank Kasper Moth-Poulsen who I worked with on the Molecular-Solar-Thermal project for being a great collaborator and for always being optimistic and positive. Although our academic background has been quite different, we have done a great job of working together quite effectively and I managed to learn much from him about a totally different field of research. I would also like to thank Ming-Chang Lu, Vinod Srinivasan and Chuanhua Duan who have worked with me on boiling and evaporation projects incorporated in this thesis. We have had great research discussions and good and productive experiences

working together which I will always appreciate. I also appreciate other lab members that I have not worked with so closely, but have also been good colleagues and friends. I will always remember our research discussions and coffee/lunch time. The list is long and includes Jayakanth Ravichandran, Renkun Chen, John Malen, Kaal Baheti, Joe Feser, Yang Zhao, Rong-Shiuan Chu, Yusra Satoglu, Robert Wang, Shannon Yee, Suzanne Singer, Keisuke Yokoyama, Dongyan Xu, Steve Meier, Nikolai Vinokurov, and many other colleagues and friends that I may have accidentally omitted.

I would also like to thank Professor Rachel Segalman for being a great mentor even though she was not officially my advisor, and for having time to advise me and have research related discussions with me. I would also like to thank Professor Van Carey for our insightful conversations and his contributions in regards to my pool boiling and evaporator wick structure projects. His advice and extensive experience has allowed me to get a different perspective on these projects, and thus a better understanding of what is new and important. I would like to thank Professor Peter Vollhardt for helping a mechanical engineering student get a better understanding of some organic and organometallic chemistry, and Professor Peidong Yang for financial support over the past couple of years. I would also like to thank Professor Grigoropoulos for being my qualifying exam chair and part of my dissertation committee and Professors Phillip Geissler, John Clarke and Samuel Mao for enduring my qualifying exam presentation. I would also like to thank Professor Chris Dames for being so understanding of our lab space and equipment situation and allowing us to complete our work, inviting us to participate in their group meetings and for the valuable discussions we had. It definitely gave me a new perspective on other projects in the heat transfer field that I could pursue.

I would also like to extend my appreciation for all the assistance, training, and tool maintenance to the Berkeley Marvell Nanolab. Without their contributions, fabrication of samples would be very difficult. I would also like to thank Mick, Gordon, Scott, Pete, Al, Mike and the rest of the ME machine shop staff for all the help and patience they provided during both my undergraduate and graduate studies here at UC Berkeley.

Lastly, I would like to thank all my other family and friends for being supportive, and sharing the bad and good times with me throughout my graduate school experience. These past five and a half years or so have been full of various experiences that have formed my character for the better, and I truly appreciate all the privileges I have had that enabled me to reach this stage in my life. I sincerely hope that from here on, not even the sky will be the limit.

1. Introduction

Current worldwide energy consumption of ~15 TW is steadily increasing and is projected to reach 25 TW by 2035. [1] Approximately 80 % of this energy is based on combustion of fossil fuels.[2,3] Heat generated in combustion is transformed into usable work via heat engines. In over 40% of fossil fuel based power plants, and most nuclear and solar thermal plants, a Rankine cycle is a primary heat engine used to convert heat into mechanical motion and ultimately electricity. In these heat engines, phase change heat transfer is the driving mechanism of energy conversion and transport via boilers, turbines, and heat exchangers. Large changes in entropy and enthalpy over very small temperature ranges when a working fluid undergoes phase change from liquid to vapor and vice versa serve to transport energy very effectively. Thus, in power generation systems, phase change heat transfer governs the quality of the vapor that is expanded in the turbine, the temperature of all components of the heat engine, and thus the efficiency of energy conversion. In addition to power generation, phase change heat transfer is important in thermal management of microelectronics (eg. heat pipes, thermal spreaders, immersion cooling, etc.),[4–8] safety of nuclear reactors,[9] latent heat energy storage and solar thermal applications,[10–14] heat exchangers,[15] etc. In all of these systems, effective phase change heat transfer ensures higher efficiency, safety, and durability of operation. For example, in thermal management applications, phase change heat transfer is used to mitigate large densities of heat from finite surfaces, e.g. microprocessors, so that they can operate with high performance safely at a desired temperature level. For these applications it is desirable to design systems which are driven by small temperature differences and able to dissipate very large heat fluxes thus minimizing thermal resistances to heat transfer. Considering the kinetic theory,[16,17] the maximum heat flux that can be dissipated via phase change heat transfer from a vapor-liquid interface of water is ~16.5 kW/cm^2. This is about two orders of magnitude higher than that of state of the art systems thus leaving much room for improvement in both power generation and thermal management systems.

Another aspect of global energy landscape that needs attention is the fraction of energy produced by renewable, sustainable and environmentally friendly energy resources, which is currently at ~8.5 % in the US.[18] Direct energy conversion of the most abundant energy source available to mankind, the sun (e.g. solar thermal, photovoltaic), comprises only ~0.17 % of the total power generation in the US,[18] and ~0.27 % globally.[3] In addition to photovoltaic,[13,19] and existing solar thermal technologies,[11,12,20] the alternative is to directly store solar energy in the form of chemical bonds of photosensitive molecules. Analogous to change of state in a solid-liquid-vapor (*S-L-V*) sense, the term phase change can also be applied to molecular systems here which exhibit reversible changes in molecular structure.[21–23] These molecules transform to a higher energy state upon direct exposure to solar irradiation, and release the stored energy in the form of heat upon thermal or catalytic excitation. If tailored appropriately, these molecular-solar-thermal (MOST) systems can serve for solar energy storage and as transportable solar fuels for on demand power generation, as well as for heating applications (eg. municipal, industrial etc.). They can also alleviate the inherent challenges of load leveling and intermittency of solar energy.[13,14] The maximum theoretical energy efficiency of these solar energy storage systems are limited to ~29 % for an idealized system,[24] and to 20% for more stringent scenarios.[25] However, over the past several decades, significantly lower efficiencies have been observed as in the extensively studied norbornadiene-quadricyclane system.[23] Additional research is needed to test new more durable molecules as

potential candidates for solar thermal power generation and solar energy storage applications, and to design practical systems capable of MOST energy conversion.

This dissertation will focus on utilizing micro and nano structured surfaces to enhance phase change heat transfer by means of evaporation and boiling for applications in thermal management of microelectronics via heat pipes and vapor chamber thermal spreaders, and pool boiling (immersion cooling) systems. In addition, the focus will be to explore manners in which phase change in photosensitive molecular systems can be utilized to store solar energy and release it in the form of heat, reversibly. In particular, the main focus will be on a recently synthesized bis(1,1-dimethyltridecyl) substituted (fulvalene)diruthenium molecule, its energy storage and conversion characteristics, and a microfluidic system designed to test these characteristics and those of other potential MOST candidates.

1.1 Heat Pipes and Vapor Chamber Thermal Spreaders

Since the establishment of Moore's law,[26] technological advances have done an excellent job of keeping up with the predicted trend of microchip production evolvement. However, in recent years the performance of microprocessors is becoming limited not by the ability to generate more densely transistor packed chips, but the inability to dissipate the heat generated during their operation.[27] In view of this challenge which limits performance and clock speeds of individual processors, companies have transitioned to multi core technologies.[27] Integration of CPUs and GPUs in microprocessors and other systems which generate even higher heat densities and operate in more extreme conditions (e.g. military, space applications, etc.) face even greater challenges in thermal management.[8] In particular, challenges in cooling local hot spots on the order of ~1mm or less in size with power densities in excess of 300 W/cm^2 that form due to non-uniform power distributions are of great concern.[6,28]

Passive systems for cooling such as heat pipes and vapor chamber heat spreaders are favorable for thermal management applications since they require no external energy source for operation, and have the potential to achieve better heat transfer characteristics at a much lower size and weight than slabs of high thermal conductivity materials such as copper.[4,29] A simple schematic of a vapor chamber heat spreader is illustrated in Fig. 1.1. Typically it is bonded to a heat generating chip via a thermal interface material (TIM). The chamber on the inside consists of a wick structure and a working fluid of appropriate thermophysical properties that minimize thermal resistances and enhance the rate of phase change. The heat from the chip is conducted through the chamber walls and through the wick structure to the liquid-solid interface where the heat induces phase change to generate vapor. Due to pressure differences, the vapor travels to the condenser where it condenses and the heat is typically dissipated by an external heat sink. The liquid is then wicked by capillary pressure to the evaporator to repeat this process cyclically. This passive cooling system is used to disperse high heat density from a smaller area to a large one, and in that way keep the temperature of the chip in a safe and favorable range. Analogous to vapor chambers, heat pipes have similar applications and operate in similar fashion to transport heat via phase change heat transfer.

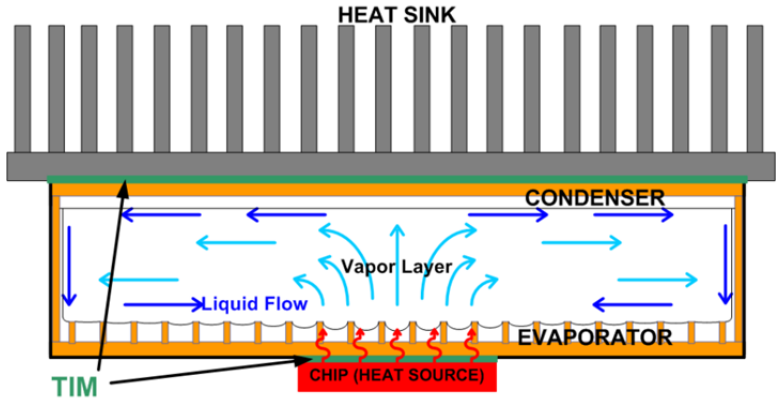

Fig. 1.1 Illustration of a vapor chamber thermal spreader; a heat source (e.g. a microprocessor chip) is bonded via a thermal interface material (TIM) to the vapor chamber which utilizes evaporation/boiling heat transfer to spread the heat to be dissipated at the heat sink.

In heat pipes and vapor chambers it is desirable to be able to dissipate high heat fluxes before burnout (CHF) is reached, and do this at very small temperature differences yielding high heat transfer coefficients (HTC).[1] In the past several decades, enhancing phase change heat transfer in evaporator and condenser wick structures has been of great importance. Generally, performance of thermal spreaders is limited by the capabilities to dissipate heat in the evaporator section.[4] Thus, much research has focused on theoretical aspects to better understand the principles of phase change at *S-L-V* interfaces and quantify rates of energy transfer. The experimental work has focused on designing, testing, and evaluating performance of various thermal spreader systems, with much of the focus on the evaporator wick.

Wayner et al. focused on understanding the role of disjoining pressure, capillary pressure and Kelvin-Clapeyron effects in phase change heat transfer evaporation at the liquid-vapor-solid contact line.[30–34] They determined that the contact line can be characterize by three regions (Fig. 1.2): a non-evaporating film where long range intermolecular forces suppress evaporation, a region of constant curvature where surface tension is dominant, and an interline (transition) region where both surface tension and intermolecular forces are important.[4,33,35] In addition, they have argued that pressure drops in the meniscus near the contact line are sufficient to drive large rates of evaporation.[30] These findings have also been supported in experimental studies.[36–38]

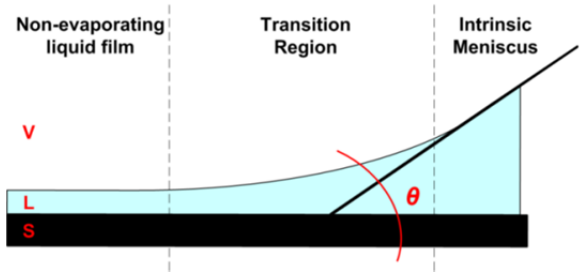

Fig. 1.2 Illustration of the *S-L-V* contact line where the meniscus forms; the meniscus profile is defined by the non-evaporating adsorbed liquid film, the transition and intrinsic meniscus regions.

[1] Throughout this dissertation, for practical purposes, dryout/burnout condition in both thin liquid film experiments and pool boiling experiments will be denoted as critical heat flux (CHF [W/cm^2]). In addition, HTC will be the terminology used to refer to the heat transfer coefficient h [W/cm^2-K].

In other studies, Wang et al. used an augmented Young-Laplace equation and kinetic theory to determine rates of evaporation for different channel sizes ranging from 2.5 μm to 210 μm.[39] They concluded that more than 50 % of heat transfer at a meniscus in a microchannel occurs in the interline region of (thickness ~1μm or less) for 210 μm wide channels and up to 97 % of heat transfer in the meniscus of 2.5 μm wide channels, and that this contribution is inversely proportional to the channel size.[39] Dhavaleswarapu et al. concluded via infrared temperature measurements that more that 70% of the heat transfer occurs in the region defined by a 10 μm film thickness near the contact line of an extended meniscus.[40] Wayner et al. used interferometry to study the effects of disjoining pressure on evaporation near the contact line and found that disjoining pressure controls the fluid flow at the contact line and thus affects evaporation supporting their theoretical predictions.[41,42] In his analytical model, Morris argued that for wetting systems, the heat transfer is defined by the shape of the contact region, and is governed by the apparent contact angle θ_α and macroscale Biot number.[43] All these findings are crucial in the design of wick structures that promote phase change heat transfer, and were considered in the design of the wick structure presented in this dissertation.

Other approaches to enhancing wick performance have incorporated structures which increased capillary pressures responsible for liquid resupply to the evaporator section, and geometries that promote evaporation and boiling. A variety of structures studied includes meshes, micro grooves, sintered particle structures, screens, carbon nanotubes, etc.[36,44–49] In some of these structures, evaporation is the dominant mode before the wick reaches dryout, and in others a combination of nucleate boiling and evaporation occurs prior to dryout. Although boiling is often deemed detrimental to heat pipe performance,[4,50,51] in some cases boiling actually enhances heat transfer without apparent disadvantages.[46–48,52,53] In micro grooved structures, evaporation is often the predominant mode of heat transfer and dryout occurs at relatively low heat fluxes.[36,47,54] In these structures performance does not typically exceed ~1 W/cm^2-K peak HTC and 30 W/cm^2 CHF.

In other investigations, better performance has been observed in mesh and sintered particle structures where boiling is clearly observed. Li et al developed copper mesh wicks capable of dissipating up to ~370 W/cm^2 with HTCs of ~25 W/cm^2-K and determined that both evaporation and boiling modes of heat transfer helped promote HTC, and also stressed the importance of good thermal contact of the porous wick media with the heated base and the resulting high effective thermal conductivity.[52,53] They argued that menisci formed between mesh wires in both horizontal and vertical direction increased capillary pressure and thus the maximum heat flux dissipated. Weibel et al have shown that due to the high capillarity of sintered porous media and high surface area for evaporation combined with boiling yield increased performance beyond 500 W/cm^2 for hot spot cooling.[48] In other systems with larger heater size, heat fluxes of ~90 W/cm^2 could be dissipated where thicker structures (>1mm) promoted nucleate boiling but yielded significantly worse HTC performance than thinner ones where only evaporation was observed.[45] A study by Davis and Garimella reported HTCs up to 12.8 W/cm^2-K at a CHF of 8.3W/cm^2 and claimed purely evaporative heat transfer.[55] Thus much disagreement exists in whether boiling or evaporation is the more effective mode of phase change heat transfer and if boiling is actually detrimental to wick performance. In addition, most of these structures yield poor performance in CHF, HTC or both, and additional innovation is necessary to improve it.

In more recent years, investigators have also implemented wick structures characterized by two length scales: small pores used to increase capillary pressure and promote wicking, and larger ones to alleviate viscous drag effects and facilitate flow in hopes of achieving higher heat fluxes. Semenic et al. used a wick consisting of large clusters of small copper particles and suggest that the small pores serve to transport liquid to the boiling sections by capillary suction, while large pores between the clusters facilitate vapor transport away from the wick thus enhancing the overall heat transfer performance.[56–58] In an earlier study of a similar system, Cao et al. observed a significant improvement of HTC in biporous vs. monoporous structures where the smaller particle size is equivalent and governs the smallest pore size in both.[59] Zhao and Chen use a similar reasoning to that of Semenic et al. to explain improved heat transfer from a surface consisting of microchannels in which the walls are made of compacted sintered copper particles.[46] In their study, samples with wider microchannels display higher CHF and HTC. From all these studies combined, the observed peak HTCs and CHFs range around ~25 W/cm^2-K and 990 W/cm^2 respectively. The insurgence of biporous wick structures has yielded significant improvements in recent years, particularly in augmenting CHF. However, lack of good thermal contact in sintered particle systems, and lack of control in their construction limits performance and hinders further improvements.

Part of the work in this dissertation is motivated by the findings of these researchers, and the focus is on developing evaporator wick structures with improved heat transfer characteristics to existing sintered copper systems. By noting that different microchannel sizes suggest different heat transfer performance at the menisci,[39] and noting that the bulk of the heat transfer in the meniscus occurs in a layer of liquid film less than 10 μm in thickness,[40] we decided on implementing microscale pin fin array wick structures in order to increase the total number and thus the areal coverage of menisci and promote evaporative heat transfer through a wick structure. We chose silicon as a material for a systematic study because of its good thermal properties, and many existing micro and nanofabrication techniques that allow for easy fabrication of desired structures. Use of silicon is also chosen in order to eliminate unwanted thermal resistances encountered in commonly used sintered structures,[52,53] and for better parameter control via microfabrication techniques. Deionized water is used in these experiments due to its good thermophysical properties. Ultimately, a biporous structure is implemented in attempts to sustain higher heat fluxes as was observed in other studies. [46,56,57,59] The results of this study will be discussed in more detail in Chapter 3.

1.2 Pool Boiling

In other applications such as immersion cooling, power generation via Rankine cycle heat engines, and other industrial processes, pool boiling is the driving mechanism for phase change heat transfer. In pool boiling, heterogeneous bubble nucleation is driven by phase change heat transfer at the *S-L-V* interface of surface cavities and imperfections, and is responsible for higher heat transfer capabilities than those of natural convection.

Extensive research has been done in pool boiling over the past century. For wetting systems where the characteristic system dimension L is large compared to the capillary or bubble length scale defined as $L_c = [\sigma/(g(\rho_l - \rho_v))]^{1/2}$, much of the data falls on a boiling curve resembling the one in Fig. 1.3. The boiling curve is characterized by several heat transfer regimes of different characteristics. It is typically plotted as the heat flux q [W/cm^2] as a function of superheat ΔT [K] ($\Delta T = T_w - T_{sat}$). In Fig.1.3 at low heat fluxes most of the heat from a solid body is dissipated via natural convection to the liquid (region A-B) yielding low HTC defined

locally as $h = q/\Delta T$. At low to intermediate heat fluxes the heat transfer rate is augmented by the onset of bubble nucleation evinced by a steeper slope on the plot, at times yielding a sudden drop of superheat (illustrated by the blue dotted line). This isolated bubble nucleation regime (region B-C) yields more effective heat transfer. As the heat flux is further increased bubble merge to form slugs and columns (region C-D). Further increase in heat flux results in the merging of bubbles at the surface of the solid body, and blanketing of the surface by a vapor film (region D-F). The poor heat transfer due to low thermal conductivity of the vapor film causes a temperature surge (red arrow) at the solid surface which can often cause meltdown and catastrophic failure.

The heat flux at which vapor blanketing occurs (point D) is deemed the critical heat flux (CHF). A high CHF contributes to the factor of safety in many applications. The higher it is, the heavier the heating loads a system can sustain without being damaged and thus causing other more severe safety hazards (e.g. as in meltdown of nuclear reactor). Once CHF is reached, and the applied heat flux reduced subsequently, often transition boiling is encountered (going along the dashed blue line F-D), here unsteady oscillations between liquid touching the surface and vapor blanketing yield very low HTC.

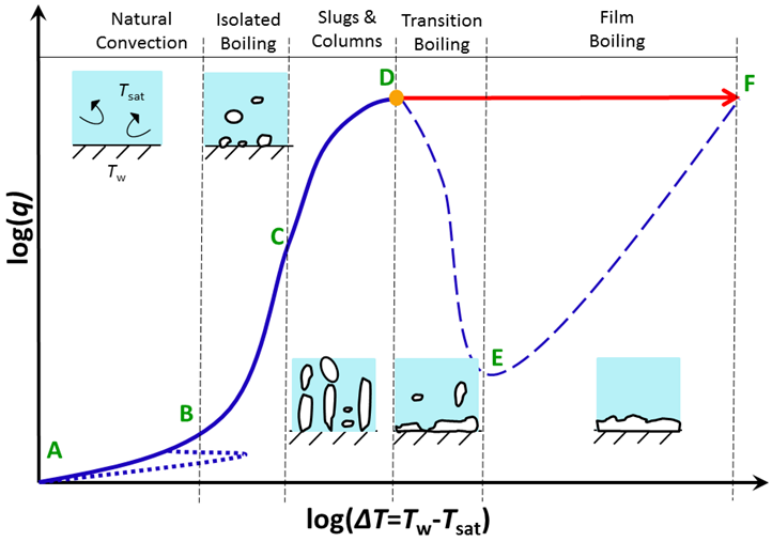

Fig. 1.3 Classical pool boiling curve for wetted surfaces for which the characteristic physical length scale L is large compared to the capillary length L_c.

In practice, a major engineering challenge has been increasing the CHF and HTC in pool boiling systems. Like in the case of evaporation/boiling in heat pipe wick structures, in pool boiling, significantly lower CHF values are observed in practice than suggested by kinetic theory.[16,17] Because of this, much research has focused on understanding other possible limiting factors to this form of phase change heat transfer. In 1959 Zuber proposed that CHF is a result of Taylor and Helmholtz hydrodynamic instabilities.[60] This theory was later modified by Lienhard and Dhir assuming that only instabilities of the most dangerous Taylor wavelength promote onset of CHF.[61] Their theoretical analysis yielded similar models which give limits in the range of 100 W/cm^2 for water based systems on wetting smooth horizontal surfaces, and often predict the CHF fairly well.[60,62]

Other researchers have argued that near the surface conditions (surface geometry, physical properties, bubble dynamics etc.) must also be crucial in defining the limit on CHF. More recent theories have been developed that do capture some near surface effects and are

capable of explaining certain data from the literature. For example, Kandlikar developed a model based on a force balance between surface tension and gravity which act to preserve the bubble intact, versus the force caused by the momentum of bubble growth induced by evaporation at the *S-L-V* contact line; the significance of contact angle is incorporated to address the liquid-solid interaction near the surface.[63] This model was found to agree well with data obtained by Liaw and Dhir for wetting systems with contact angles greater than ~20^{o}.[64] Using infrared imaging, and X-ray diffraction spectroscopy, Theofanous verified experimentally that local dry spots occur on a surface during pool boiling.[65,66] These can be reversible, but also irreversible and at a sufficiently high heat flux merge with other neighboring bubbles to blanket the surface with vapor and cause CHF; they stress that higher nucleation site density increases CHF on aged titanium film heaters (oxidized by pulse heating and repeated boiling) and claim that hydrodynamic theory is inappropriate for explaining their observations. In view of these disagreements in the scientific community, the proposed limits do not seem firm and researchers continuously engineer surfaces in hopes to promote both HTC and CHF and get a more firm understanding of the physical limits involved. Enhancing both HTC and CHF simultaneously may however prove to be challenging due to experimental evidence which indicates that wettability is extremely effective in suppressing bubble nucleation,[67–69] the dominant mode of heat transfer in pool boiling systems.

In recent years surface modifications and use of nanofluids have been incorporated for CHF enhancement. Kim et al showed that alumina, zirconia and silica nanoparticles suspended in water deposit on the surface during boiling thereby forming a porous layer and making the surface more hydrophilic and increasing CHF up to 200%.[69,70] They also note that the increased wettability yields significantly reduced HTC. In another study Kim et al. noticed a similar increase in CHF with titania and alumina nanoparticles in water on metal wire heaters.[71] Ahn et al observed a similar increase in CHF of water on micro/nano structured surfaces generated by anodic oxidation. They claimed that the surface structures increased both wettability and capillary wicking thus yielding CHF of ~190 W/cm^2 on horizontal heaters.[72–74]. Honda et al implemented silicon micropillar structures and observed CHF as high as ~63 W/cm^2 for dielectric liquids, more than a twofold increase to that of a plain surface and the limits suggested by hydrodynamic theories. [75,76] They argued that roughened pin fin arrays yielded higher CHF and HTC values due to increased nucleation site density and actual surface area enhancement due to presence of the pin array.[75] Li and Peterson observed CHF up to ~ 370 W/cm^2 on high conductivity porous mesh structures arguing that increased capillarity, nucleation site density and capillary evaporation were responsible for the enhancement.[77] More recent work of Chen et al and Lu et al. with silicon nanowire structured surfaces,[78,79] indicate these nanostructures are capable nearly doubling CHF as compared to a flat silicon surface due to higher capillary pressures and great wetting characteristics (~160 W/cm^2 with apparent contact angle of $\theta_\alpha \sim 0^o$); they also observe a substantial increase in HTC to that of a plain surface due to higher nucleation site densities especially at high heat fluxes.[78–80] A recent study by Li and Peterson also suggested that increased nucleation site density by means of nanostructuring can significantly augment HTC, without compromising CHF. They observed an HTC enhancement of ~60 % near CHF from a copper nanorod covered surface to a plain copper surface, and attributed this to smaller departure diameters, increased bubble release frequencies and nucleation densities that nanostructured surfaces provide.[80]

In many of these systems, significant enhancements of CHF are observed which contradict claims suggested by hydrodynamic theories. Researchers often attribute these

enhancements to several phenomena such as increased capillarity, wettability or nucleation site density, which are not considered in hydrodynamic theory. However, there still seems to be a lack of systematic approaches that can better isolate these phenomena and yield more conclusive results on the mechanisms of CHF. In addition to exploring the limits of CHF, engineering surfaces that promote high HTC is favorable for thermal management applications. Implementing hybrid micro/nano structured surfaces can potentially yield higher HTC and not compromise or even enhance CHF characteristics. Part of this dissertation will focus on testing this hybrid micro/nano structure hypothesis, and another part will attempt to distinguish phenomena that limit CHF by comparing thin liquid film and pool boiling experiments on similar capillary structured finite surfaces. This will be presented in Chapter 4.

1.3 Photosensitive Molecular Systems

When considering the landscape of power generation in the US,[18] and globally,[1,3] a very small fraction of it comes from renewable, sustainable, and environmentally friendly sources. Cost of solar energy conversion technologies,[81] and the dearth of effective solar energy storage technologies makes the sun, an essentially infinite energy source, quite a surprisingly small contributor to power generation worldwide (~0.27% worldwide).[3] The diurnal nature of solar radiation and dependence on climatic factors can make large scale solar energy power generation impractical for inclusion in our present electrical power grid. To overcome these obstacles and satisfy the needs of load leveling, new effective technologies for long term solar energy storage are necessary. In one hour ~ 440 EJ of solar energy reach our planet which is comparable to the total energy consumed globally in one year (~550 EJ) at current rates.[1] This fact is very motivating for establishing new or improving existing technologies which utilize the most abundant energy source to mankind.

In direct solar energy conversion to electricity and solar energy storage in the form of heat, research is mainly focused on photovoltaic (PV) systems,[13,82,83] and solar thermal systems (energy storage via latent heat or sensible energy) respectively.[11,12,20,84–87] The former is used for direct power generation, while the latter, can be used for direct power generation, heating, and limited thermal energy storage (several hours); ultimately the efficacy of both technologies depends on weather conditions.[1] Currently, the majority of solar thermal technology is implemented for municipal heating and industrial applications.[1]

An attractive alternative for solar energy storage and conversion is via photochromic molecular compounds.[21,22,88] Because they store energy in the form of chemical bonds, like fossil fuels, these molecular systems exhibit inherent perennial energy storage characteristics. Unlike PV and existing solar thermal technologies, solar energy storage in photochromic systems can be achieved volumetrically in remote locations with better weather conditions and the fuel can be transported for on demand use.[88] A minor drawback of using these molecules is that many are made of organic compounds and degrade at temperatures beyond ~200 ^{o}C. Therefore, applications of these photochromic systems are limited to low grade heat generation which can be converted to work in organic Rankine cycle power plants.[89] In 2005, ~4.5 EJ of fossil fuel based energy was used in water and space household heating in the United States alone.[18] If not for power generation, if durable these thermal batteries can be implemented as recyclable and transportable fuels for municipal heating and in this way trim fossil fuel consumption and resulting pollution.

Figure 1.4 shows a representative reaction scheme in these photochromic molecules. Upon solar irradiation, with some probability, energy (E_g) is absorbed by molecule A which transitions to an excited state A^*. E_g corresponds to the energy gap between the ground state energy of A and the photo excited state energy A^*. Since A^* is a short lived metastable state, the molecule relaxes back to stationary ground state A or a new higher metastable energy stationary state B. Molecules A and B differ in structure (eg. valence isomerization or a geometric cis-trans isomerization), but the chemical composition is preserved; as a result this can be considered a phase transition of the molecular structure. The difference in ground state energies of A and B is the energy storage enthalpy $\Delta H_{storage}$. In the schematic, E_a represents the activation energy that needs to be overcome in order for molecule in state B to transition back to state A. This energy barrier is associated with the free energy barrier ($\Delta G_a = \Delta H_a - T\Delta S_a$), and determines the probability of the back reaction occurrence (B → A). If too small, very small perturbations in energy (eg. thermal excitation) are sufficient to revert from B to A and thus prevent long term energy storage. With a sufficiently large E_a, molecule B can store the solar energy indefinitely and release it on demand via use of an appropriate catalyst. Typically these molecules are characterized by their energy storage enthalpy, photochrome efficiency, and their durability.[25,90,91]

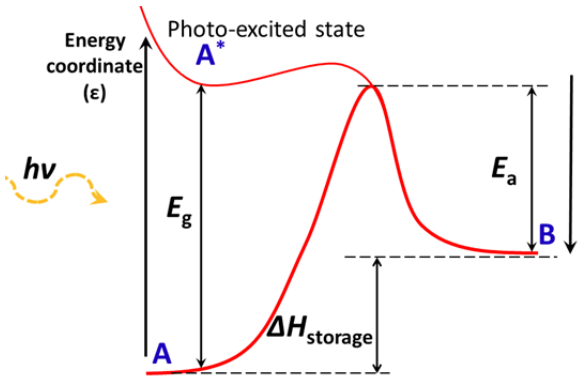

Fig. 1.4 Illustration of the phase transition of the photochrome A to a different configuration B at the higher ground state energy; the reaction is reversible and the stored energy $\Delta H_{storage}$ is the difference between the two ground state energies separated by an energy barrier E_a.

Extensive research has been done on several such molecular systems for solar energy harvesting. Norbornadien-Quadricyclane (*N*-*Q*, $\Delta H_{storage}$ ~1194 J/g) system is probably the most extensively studied system experimentally and theoretically.[92–95] Several researchers have studied the storage characteristics of these molecules and their derivatives. Reviews published by Bren et al. and more recently Dubonosov et al. summarize many modifications that have been implemented in this system to increase energy storage density, storage efficiency, and durability.[23,96] In some engineering endeavors, researchers have tried to implement these molecules in actual power generation systems, studied their recyclability and durability characteristics over many cycles of conversion, and investigated the economic viability in actual applications.[91,97–99] In majority of these cases, these molecules lack either good energy storage characteristics, or have many issues with degradation over time and repeated cycling. Additionally, a large disparity between theoretical limits of photochrome energy storage efficiency,[100,101] and that in existing systems,[23] suggests improvements are possible. In a study by Bolton, 10 % storage efficiency was deemed as a reasonable goal, and efficiencies exceeding 13 % highly unlikely in these molecular systems.[101] Bolton also suggested that

rather than energy storage efficiency, enhancing durability might be an even greater challenge for these systems.

Recently, a very stable organometallic ruthenium based $FvRu_2$ system shown in Fig. 1.5 has shown good storage characteristics.[102–105] The molecule is composed of a fulvalene bridged together by two ruthenium atoms with CO ligands as shown in Fig. 1.5. This system undergoes a reversible cis-trans transition and the chemical constituents remain unchanged.

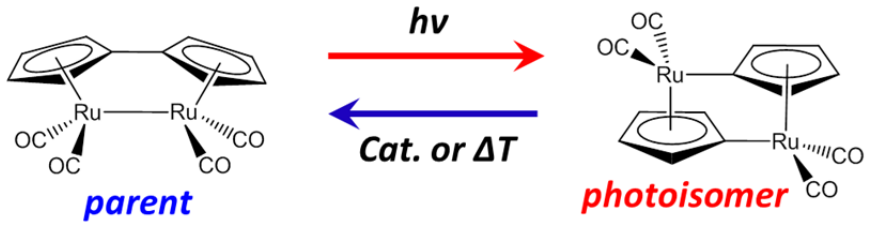

Fig. 1.5 Molecular structure of the original unsubstituted di-ruthenium fulvalene ($FvRu_2$) solar energy storage system undergoing a cis-trans structure transition from parent (left) to higher energy state isomer (right) when exposed to solar radiation.

There are several reasons for pursuing further investigation of solar energy storage characteristics in the $FvRu_2$ system:

a) This organometallic system has shown stable and perennial storage capabilities (photoisomer discharges at ~5% per year at room temperature),[88] unlike its purely organic predecessors.[23,96]
b) The measured storage energy of $FvRu_2$ suggests that if all ~195 J/g was converted to heat,[104] an adiabatic temperature rise up to 200 ^{o}C can be expected.
c) $FvRu_2$ molecules have shown great resistance to degradation at elevated temperatures (tested up to 350 ^{o}C).
d) Limited research on organometallic compounds and applications to solar energy storage and implications of stability over time and at elevated temperatures motivates a new direction where new molecules can be engineered based on the insight obtained from studies of the $FvRu_2$ system.

Based on energy density merit, pure $FvRu_2$ compound is currently comparable to existing latent and sensible energy storage systems and battery technologies as shown in Table 1.1. However, since photoconversion only occurs when the parent molecule in Fig. 1.5 is in solution, this energy density is significantly compromised to ~ 5 J/g due to poor solubility of $FvRu_2$ in common organic solvents (peak solubility of 21.6 mg/ml in THF).[106] As a result, a chemically modified $FvRu_2$ is implemented here to enhance the solubility of both parent and isomer and thus increase solution energy density. These ruthenium based molecules are scrutinized for energy storage capabilities (storage enthalpy, photochrome efficiency, specific heat) in a microfluidic system specifically built for testing these properties and screening potential catalysts for the back reaction (B→A Fig. 1.4) for heat release. For practical applications, synthesis of an iron based compound (eg. $FvFe_2$) would be desired because iron is more abundant and cheaper than ruthenium. However, thus far, implementation of iron indicates poor energy storage characteristics,[104] and more importantly has yet to yield a stable photoisomer. Although ruthenium is not readily available and cheap, the primary goal here is to demonstrate a proof of principle continuous solar energy conversion – heat generation scheme using organometallic compounds and test its durability and performance via a measurable temperature rise.

Table 1.1 Summary of energy densities of various energy storage technologies. Here only batteries are not directly associated with solar energy but are incorporated for comparison as alternate energy storage systems.

Material	Storage Technology	Peak Energy Density [MJ/kg]	Operation temperature range [^{o}C]
N-Q [23]	MOST	1.19	T < 150
$FvRu_2$ [104]	MOST	0.20	T < 350
Li-ion [13]	Batteries	0.54	N/A
Lead-Acid [13]	Batteries	0.14	N/A
Paraffins [12]	Latent Heat	0.17 – 0.27	5 < T < 75
Salt-Hydrates [12]	Latent Heat	0.07 – 0.30	14 < T < 117
Water	Latent Heat	2.26	100
Water	Sensible Heat	0.32	0 < T < 100
Oil	Sensible Heat	0.25	T < 160
Molten salt [107]	Sensible Heat	0.48	265 < T < 565

1.4 Organization of the Dissertation

The focus of this dissertation is two-fold. Firstly it will include findings related to enhancements in evaporation/boiling phase change heat transfer on engineered micro/nano surfaces. Secondly, the dissertation will focus on solar energy storage in phase transitions of ruthenium based photosensitive molecular systems. Therefore the structure of the dissertation will be as follows: In Chapter 2 the focus will be on the physical and thermodynamic fundamentals that govern heat transfer in heat pipe and pool boiling systems. These topics will include surface phenomena, theoretical and physical limits of operation, homogeneous and heterogeneous bubble nucleation, and other applicable theory. In Chapter 3 I will present my approach to increasing performance in heat pipe evaporator wicks by using biporous microstructures. In Chapter 4 I will also make a connection between CHF in pool boiling and CHF in thin liquid film phase change in these structures based on experimental findings, and discuss my approach to increasing pool boiling performance in micro/nano structure engineered surfaces. I will then shift the focus to the second part of this dissertation. In chapter 5 I will give some theoretical background on principles behind energy storage in photochromic molecular systems. I will discuss how energy is transferred in these systems, and the quantum yield and the overall efficiency of a photochrome. In chapter 6 I will then present a ruthenium based organometallic system for solar energy storage, and discuss its energy storage capabilities and my approach to demonstrating how such systems can be incorporated for solar energy conversion to heat and for screening of other candidate molecules. Finally Chapter 7 will contain concluding remarks about my research and findings, and a section about the outlook of these projects.

2. Fundamentals of Heat Pipes and Nucleate Boiling

The focus of this chapter is to introduce fundamental physical and thermodynamic theories involved in evaporative heat transfer and nucleate boiling. In addition, some basic relations for modeling phase change heat transfer in evaporative and boiling systems are introduced. The topics included are chosen because they are most relevant to the content of this dissertation. More detailed considerations of these topics, and broader analysis of these phase change phenomena can be found in textbooks by Schrage, Carey, Faghri, Israelachvili and Dunn and Reay. [4,17,50,108,109]

2.1 Heat Pipes and Vapor Chambers

A vital component of a vapor chamber thermal spreader or any heat pipe which allows for passive operation is the wick structure. Just like in oil lamps, or in wax candles, the wick serves to draw a liquid to a region of low pressure by capillary action. Along with capillary forces, other force fields and surface free energies at the solid-liquid-vapor (*S-L-V*) interface play an important role in governing the flow and liquid profile within a wick. These include disjoining pressure, surface tension and contact angle, and their significance will be discussed in the next section.

2.1.1. Solid-Liquid-Vapor (*S-L-V*) Phenomena

Surface Tension and Contact Angle

For a liquid droplet of resting on a solid surface as shown in Fig. 2.1, close to the *S-L-V* interface (e.g. point X in Fig. 2.1) liquid molecules feel a stronger net force from the solid than from the vapor due to the large density difference between the two phases. For a wetting scenario, the liquid is attracted more by the surface of the solid, and the interface is deformed to a minimum surface area experiencing a surface tensile force due to the deformation. This is true for any interface where there is a net force to be balanced (e.g. vapor bubble in a pool of liquid, rain droplet in air, at an interface of a polar and non-polar liquid etc.).

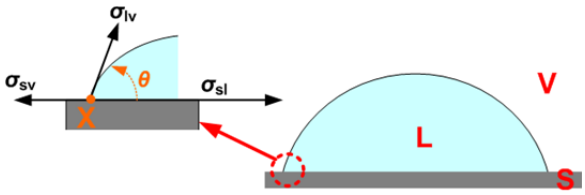

Fig. 2.1 Illustration of an equilibrium situation where a wetting droplet rests on a solid surface surrounded by a vapor phase; At point X, a force balance is considered to relate the surface energy properties of the three phases via the apparent contact angle θ_α.

Looking at this contact region more closely as depicted in Fig. 2.1, a force balance tangentially along the interfaces in the horizontal direction at the contact line (at point X) yields the relationship between properties of each interface

$$\sigma_{lv}\cos\theta - \sigma_{sv} + \sigma_{sl} = 0$$

$$\cos\theta = \frac{\sigma_{sv} - \sigma_{sl}}{\sigma_{lv}} \qquad (2.1a, b).$$

In this relation (Young's equation), θ is the apparent equilibrium macroscopic contact angle, σ_{sv} is the surface tension between solid and vapor phases, σ_{sl} the surface tension between

solid and liquid phases, and σ_{lv} the surface tension between liquid and vapor phases. Surface tension can be regarded as either the free energy per unit area, or force per unit length of surface/interface.[17] The vertical force component at the contact line in Fig. 2.1 is balanced by the reaction force in the solid in this situation.

Additional considerations of surface tension and contact angles can be found in textbooks by Faghri, Carey and Israelchvilli.[4,109] Also, early works by Wenzel, and Cassie and Baxter, focus on how surface structure can also affect wetting characteristics.[110,111] Wenzel argues that surface roughness can amplify both wetting and non-wetting characteristics by changing the surface free energy via change in interfacial surface area. This is depicted in Eq. (2.2) where the factor γ is the ratio of the actual area of a rough surface to the projected area onto a 2-D plane, θ is the contact angle predicted by Young's relation (Eq. (2.1b)), and θ_a the new apparent contact angle. Cassie and Baxter argued that for porous surfaces the Wenzel state is a special case of a more careful consideration. They argue that roughness can also act to trap vapor below a liquid layer thus reducing wettability

$$\cos\theta_a = \gamma \cos\theta \qquad (2.2).$$

In heat pipes, and particularly evaporator wicks, wetting systems are always used and all these effects must be considered in the design process. Effects of wettability on phase change heat transfer has been summarized in other works.[112,113]

Capillary Pressure

In wicks, the capillary pressure induced flow is caused by differences in the curvature at the liquid-vapor interface within the wick pores. In smaller pores the curvature is larger and local liquid pressure is lower. Thus the liquid flows in the direction of lower capillary pressure. The capillary pressure ΔP_{cap} for a liquid in a tube of radius r can be defined as:

$$P_v - P_l = \Delta P_{cap} = \frac{2\sigma\cos\theta}{r} \qquad (2.3),$$

where P_v is the local vapor pressure, P_l is the local liquid pressure, θ the apparent contact angle and σ the surface tension. From this expression it is apparent that liquids with high surface tension and small contact angles provide very large capillary pressures in small pores. This is one of the reasons that wetting liquids are always used in heat pipes. To illustrate the significance of the capillary pressure we consider Fig. 2.2 which shows a tube partially submerged in a pool of wetting liquid.

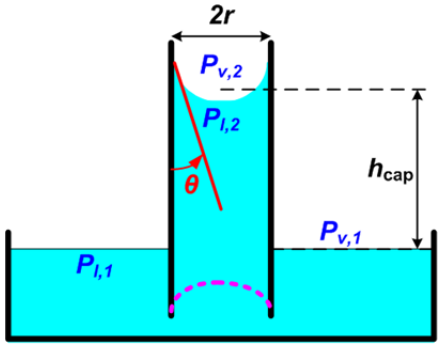

Fig. 2.2 Capillary rise of a wetting liquid inside a cylindrical tube of radius r; the liquid is drawn by capillary pressure to a height h above the free surface.

Considering pressure differences in the vapor of density ρ_v and liquid of density ρ_l and the capillary pressure as defined by Eq. (2.3) (in this case $\Delta P_{cap} = P_{v,2}\text{-}P_{l,2}$), the height of the liquid layer h_{cap} that the capillary pressure is capable of suspending above the surface against gravity can be obtained as shown in Eq. (2.4). This characteristic of capillary pressure is the driving mechanism behind passive operation of heat pipes and vapor chambers in the presence of gravity and potentially other external forces.

$$h_{cap} = \frac{2\sigma\cos\theta}{rg(\rho_l - \rho_v)} \qquad (2.4).$$

In non-wetting liquids, the liquid meniscus is concave down and below the free surface (indicated by the dashed magenta line in Fig. 2.2) and the same expression can be used to find the depression h_{cap} below the free surface. Thus, non-wetting liquids cannot be used in heat pipes because they would require external work to be done against the capillary force to force the working fluid within the pores.

Disjoining Pressure

The meniscus of the wetting system can be divided into three regions: a) a non-evaporating film where disjoining pressure P_d defines the film thickness and shape, b) a transition (interline) region where both capillary and disjoining pressures play a role in shaping the interface, and c) the intrinsic meniscus governed strictly by the capillary pressure P_{cap}.[30] This is better depicted in Fig. 2.3 where the local vapor pressure P_v is defined in terms liquid pressure P_l and all other relevant pressures in the system.

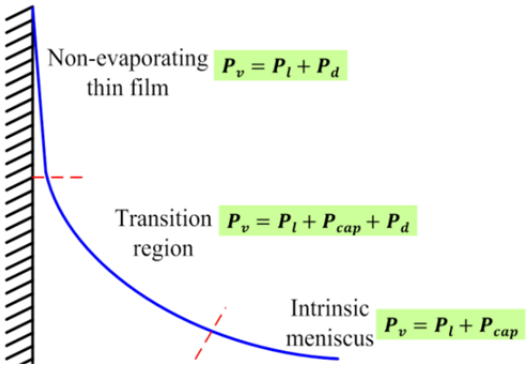

Fig. 2.3 Meniscus formed at the contact line of a wetting liquid; the liquid profile and flow dynamics within each of the regions are governed by disjoining and capillary pressures as indicated.

The disjoining pressure quantifies the strength of the force per unit area required to detach the adsorbed liquid film from the solid surface. In this force field, molecular (van der Waals) and electrostatic interactions (polar liquids) are significant. Typically, the disjoining pressure can be cast in the following power law form

$$P_d = -\frac{\hat{H}_A}{\delta^\beta} \qquad (2.5).$$

In this relation, $\hat{H}_A$ is the Hamaker constant which links the interactions of fluid molecules and those of the solid surface, β is the exponent (typically 3 or 4), and δ the liquid film thickness. Thus thinner films experience higher disjoining force. The major significance of disjoining pressure is two-fold: it is fundamental in formation of thin liquid films near the

contact line (e.g. menisci), and it becomes particularly significant during evaporation because of its role in fluid transport within the transition region (see Fig. 2.3).

This section briefly establishes force fields and surface phenomena essential in describing interactions of any *S-L-V* system. In heat pipes, porous structures are used which often produce many menisci similar to a profile shown in Fig. 2.3. A complete understanding of the phenomena involved allows for predicting the shape of the contact line profile accurately for better understanding of the phase change heat transfer there.

2.1.2 Thermal Resistances in Heat Pipes

In the design of passive thermal spreaders, understanding and being able to quantify and predict temperature drops in all components is very important. A vapor chamber heat spreader illustrated in Fig. 2.4 has several temperature drops: across the enclosure material (ΔT_1, ΔT_7), through the evaporator and condenser wicks (ΔT_2, ΔT_6), in the vapor space (ΔT_4), and at the liquid/vapor interfaces (ΔT_3, ΔT_5). At steady state, with knowledge of the applied heat flux, this system can be modeled as a thermal resistance network shown in Fig. 2.4. Typical thermal resistances encountered in applications corresponding to each component are summarized in the table of the figure. Resistances in the vapor space are typically very low,[29,50] as well as those at the liquid-vapor interfaces.[4,16,17] Enclosures are typically made of high thermal conductivity materials (e.g. copper, aluminum) and also have negligible thermal resistances. Thus, heat spreader performance is typically limited by the thermal resistance of the evaporator and condenser wicks. This section will give a brief overview of how these resistances can be quantified.

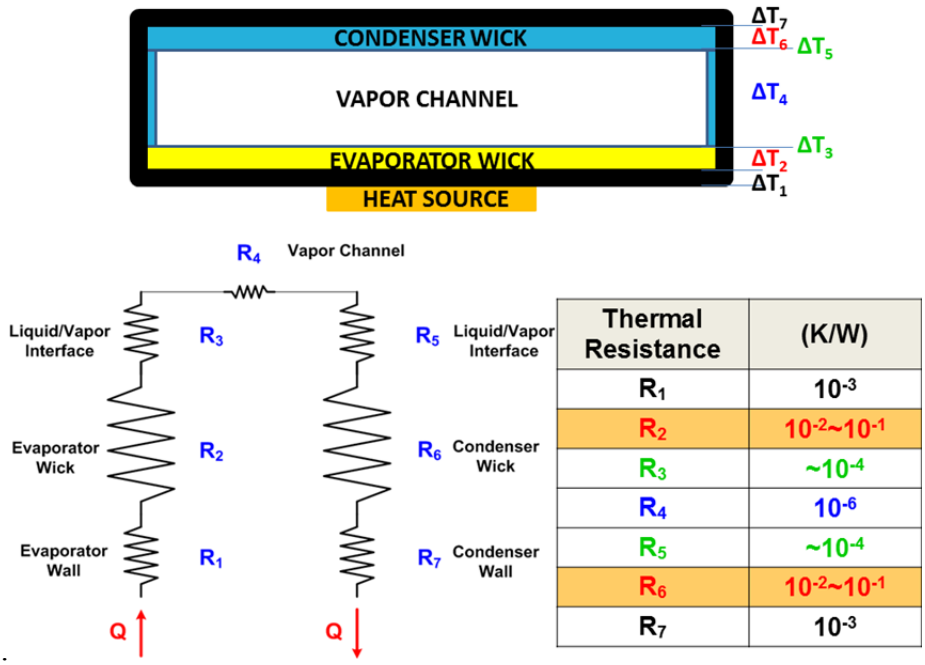

Thermal Resistance	(K/W)
R_1	10^{-3}
R_2	10^{-2}~10^{-1}
R_3	~10^{-4}
R_4	10^{-6}
R_5	~10^{-4}
R_6	10^{-2}~10^{-1}
R_7	10^{-3}

Fig. 2.4 (a) Illustration of a vapor chamber thermal spreader and the temperature drops ΔT_i of its integral components; (b) A schematic of the thermal resistance network that can be implemented in modeling heat transport inside vapor chamber and heat pipe devices with relevant thermal resistances numerically matched with the temperature drops in illustration (a); (c) Approximate order of magnitude of thermal resistances encountered in real application systems.

Evaporator/Condenser Wicks

In evaporator and condenser wick structures, the high thermal conductivity of the solid material is a key in minimizing thermal resistance. However, in order to promote phase change heat transfer a porous medium with high capillary pressure is necessary thus compromising some characteristics of the solid material. In a plane 2-D structure with constant average porosity, the effective thermal conductivity of the wick can be estimated by Eq. (2.6a) as:

$$k_{eff} = (1-\phi)k_s + \phi k_l$$

$$R_{wick} = \frac{t}{k_{eff} A} \qquad \text{(2.6a, b).}$$

Here ϕ is the wick porosity (ratio of void to total wick volume) and k_s and k_l are the solid wick material and working fluid thermal conductivities respectively. The thermal resistance R_{wick} is then defined in Eq. (2.6b) where A is the cross sectional area of the wick and t the wick thickness. For sintered copper particles which are typically used in thermal spreaders and heat pipes, k_{eff} is on the order of 20-150 W/m-K (this can be significantly lower than ~400 W/m-K in pure copper due to both porosity and poor thermal contacts between sintered particles) yielding a relatively high thermal resistances (10^{-1}~10^{-2} K/W).

Vapor Space and Enclosure Material

Figure 2.5 illustrates a schematic of a cylindrical heat pipe of cross sectional radius b, and L_{ev}, L_{ad} and L_{cn} which are the lengths of the evaporator, adiabatic, and condenser sections respectively.

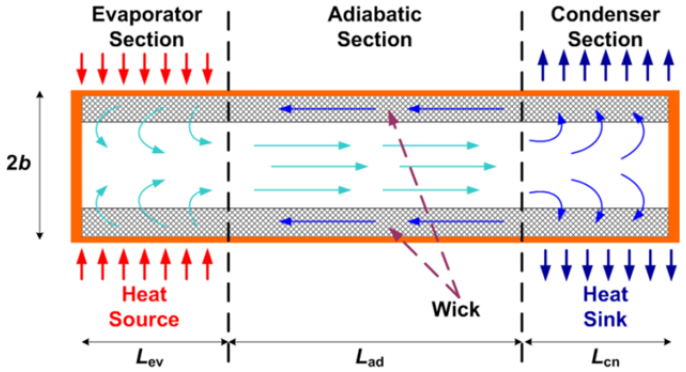

Fig. 2.5 Illustration of a cylindrical heat pipe of radius b that absorbs heat in the evaporator section via phase change heat transfer, transports it through the adiabatic section of the heat pipe where no heat transfer occurs between the vapor in the channel and liquid the wick structure, and dissipates the heat via condensation in the condenser section.

At steady state conditions, the effective thermal conductivity of the vapor in the adiabatic section can be derived.[29,50] For simplicity of analysis, a cylindrical heat pipe is considered and the vapor is assumed to behave as an ideal gas. The pressure drop $\Delta P_{ad\text{-}HP}$ in a pipe for incompressible, fully developed, laminar flow assumed in the adiabatic section is given by Poiseuille flow inside a circular tube

$$\Delta P_{ad-HP} = \frac{8\mu_v L_{ad}\dot{m}}{\pi\rho_v b^4} \qquad \text{(2.7).}$$

In Eq. (2.7), μ_v is the vapor dynamic viscosity, L_{ad} and b the length of the adiabatic section and heat pipe radius respectively, $\dot{m}$ the mass flow rate, and ρ_v the vapor density. By using the Clausius-Clapeyron equation (Eq. (2.8a)), and realizing from the ideal gas law that $v_v=\hat{R}T_v/P_v$ the pressure drop can be related to a temperature drop in the heat pipe vapor space $\Delta T_{ad\text{-}HP}$ (Eq. (2.8b)) as

$$\frac{dP}{dT}=\frac{h_{lv}}{T\Delta v}$$

$$\Delta T_{ad-HP}=\frac{8\hat{R}\mu_v L_{ad}\dot{m}T^2}{\pi h_{lv}P_v\rho_v b^4} \qquad (2.8a, b).$$

where the additional terms $\hat{R}$, P_v, Δv and h_{lv} are the specific ideal gas constant, the vapor pressure, the difference in specific volume of vapor and liquid phases, and latent heat respectively. Realizing that the heat $Q = \dot{m}h_{lv}$, the thermal resistance of the adiabatic section of a cylindrical heat pipe and any other section of length L can be approximated more generally as:

$$R_{ad-HP}=\frac{\Delta T_{ad}}{Q}=\frac{8\hat{R}\mu_v LT^2}{\pi h_{lv}^2 P_v\rho_v b^4}$$

$$R_{ad-VC}=\frac{\Delta T_{ad-VC}}{Q}=\frac{12\hat{R}\mu_v T^2}{P_v\rho_v h_{lv}^2}\left(\frac{z}{wt_{vc}^3}\right) \qquad (2.9a, b).$$

Similar analysis can be done to determine the thermal resistance of the vapor space in a rectangular vapor chamber (Eq. (2.9b)) illustrated in Fig 2.4.[29] To arrive at this expression it is assumed that its thickness t_{vc} (closest distance between evaporator and condenser across the vapor space not including the wick) is much smaller than its width w. Here z is the total thickness of the vapor chamber including the evaporator and condenser wicks.

For illustrative purposes, assuming a water as a working fluid in a b = 0.5 cm radius and L = 5 cm long pipe, the thermal resistance is approximately $R_{ad} \sim 10^{-6}$ K/W which is much lower than thermal resistances of other components as indicated in Fig. 2.4. This characteristic makes heat pipes and vapor chambers very effective at transporting and spreading heat.

Liquid/Vapor Interface

Another resistance to consider is the thermal resistance of the vapor/liquid interface as depicted in Fig. 2.6 In other words, it is important to quantify the rate of phase change at the interface and gauge it with respect to a driving temperature potential.

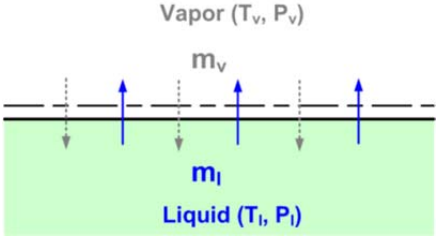

Fig. 2.6 Illustration of a flat liquid-vapor interface where molecules constantly transfer between liquid and vapor phases even at equilibrium.

From kinetic theory, the overall rate of evaporation is given by the difference of liquid molecules leaving the interface into vapor phase, and vapor molecules entering the liquid phase across the interface. From the analysis of Schrage,[16] for a system where this particle interchange across the interface occurs at equilibrium, the net mass flux m'' is given by Eq. (2.10)

$$m'' = \frac{2\alpha}{2-\alpha}\left(\frac{M}{2\pi\breve{R}}\right)^{1/2}\left[\frac{P_v}{T_v^{1/2}} - \frac{P_l}{T_l^{1/2}}\right] \qquad (2.10).$$

In these equations, $\hat{R}$ is the ideal gas constant, M the molecular weight, T_v the vapor temperature, T_l the liquid temperature, P_v the vapor pressure, P_l the liquid pressure and α the accommodation coefficient. The accommodation coefficient quantifies the fraction of molecules that actually cross the interface due to evaporation; the remaining $(1 - \alpha)$ gives the number of molecules already in the vapor phase that are just reflected at the interface. Thus, when accommodation coefficient is exactly 1 the evaporation/condensation mass flux is maximized in Eq. (2.10). Further manipulation of Eq. (2.10), (see refs. 16 and 17 for more detailed analysis) and multiplication by the latent heat h_{lv} yields the heat flux q across the interface as:

$$q = \frac{2\alpha}{2-\alpha}\left(\frac{M}{2\pi\breve{R}T_v}\right)^{1/2}\frac{h_{lv}^2}{T_v\Delta v}\left[1 - \frac{P_v\Delta v}{2h_{lv}}\right]\Delta T_{lv} \qquad (2.11).$$

In addition, the heat transfer coefficient of the interface can be defined by dividing Eq. (2.11) by the interfacial temperature difference ΔT_{lv} to get:

$$h = \frac{2\alpha}{2-\alpha}\left(\frac{M}{2\pi\breve{R}T_v}\right)^{1/2}\frac{h_{lv}^2}{T_v\Delta v}\left[1 - \frac{P_v\Delta v}{2h_{lv}}\right] \qquad (2.12).$$

Assuming an accommodation coefficient of 1 or 0.03, for which arguments have been made to be reasonable assumptions for water, [17] the value of h is ~1.51 kW/cm^2-K and ~24 W/cm^2-K respectively. Thus it is evident that the maximum heat transfer across an interface depends strongly on the accommodation coefficient, but typically, the interfacial resistance is considered negligible compared to that of other components in heat pipes.[4]

The film thermal resistance can then be approximated as $R_{int} = 1/hA$, which is on the order of $R_{int} < 10^{-3}$ K/W assuming $\alpha \approx 1$ as summarized in the table of Fig. 2.4.[4] Generally, to minimize contributions of interfacial thermal resistance, a system with a large surface area of interface is desired. This can be achieved via microstructuring. In this way the enhancement can be done in two ways simultaneously: by increasing interfacial surface area, and by having a large fraction of this area form at the thin liquid film region at the menisci where evaporation rate is higher.

In addition, from these considerations, the maximum theoretical heat flux is approximated when all molecules are leaving into vapor phase as $q = 0.741(\bar{v}\rho_v h_{lv})$. The factor of 0.741 was determined in the analysis of Schrage and depends on the velocity distribution at the interface.[16] This yields a maximum heat flux of ~16.5 kW/cm^2, which is significantly higher than that observed in actual systems discussed in the introduction.

2.1.3 Heat Pipes and Limits of Operation

Because the focus of this dissertation is more on the performance of the evaporator wick structure, this section will discuss some physical phenomena that limit its performance. Here, only more relevant limits to the geometries and working fluids implemented in this dissertation will be presented such as the capillary and boiling limit. A more in depth consideration of all limitations (eg, sonic, entrainment etc.) that hinder the performance of heat pipes and thermal spreaders can be found in a textbook by Faghri, and Dunn and Reay.[4,50]

Capillary Limit

Capillary limit in a heat pipe is reached when the capillary pressure ΔP_{cap} no longer exceeds the sum of all other pressure drops within the system

$$\Delta P_{cap} \leq \Delta P_l + \Delta P_v + \Delta P_g \tag{2.13}$$

This includes pressure drops in the liquid ΔP_l, vapor ΔP_v, and pressure drops due to gravitational effects ΔP_g. Thus in a typical heat pipe with the smallest pore size r_p which operates with a working fluid of surface tension σ, this can be approximated as:

$$\frac{2\sigma}{r_p} \leq \frac{\mu_l \dot{m} L}{\rho_l A \kappa} + \frac{8\mu_v \dot{m} L}{\pi \rho_v b^4} + \rho_l g L \sin\Omega$$

$$\kappa = \frac{d_p^2}{180} \frac{\phi^3}{(1-\phi)^2} \tag{2.14a, b).}$$

In this simplified expression, the left hand side is the maximum capillary pressure in the wick assuming a perfectly wetting working fluid. The first term on the right side is the pressure drop in the liquid from Darcy's law for a liquid flowing through a porous medium of flow cross sectional area A. Here κ is the permeability of a porous structure and can be quantified by the approximation in Eq. (2.14b) which is derived from the Kozeny-Carman equation for flow through a packed bed of particles (e.g. sintered copper wick of particle diameter d_p).[114] Kays and London give a more in depth overview of empirical data and correlations on flow resistances encountered in porous media of various geometries.[115] The second term on the right side is the overall pressure drop in the vapor within a cylindrical heat pipe of total length L (e.g. Fig. 2.5) assuming Poiseuille flow (this was also discussed in section 2.1.2). Finally, the last term includes pressure drops in the liquid due to gravity effects, where Ω is the angle of inclination of the heat pipe. Equation 2.14a is based on a very simplified model, and is not intended to be very accurate but rather illustrate quantitatively the pressure drops involved in heat pipe operation that capillary pressure needs to overcome in order for the system to function properly. When only considering the evaporator wick structure, only the first and last term on the right side of Eq. (2.14a) may be important, because the capillary limit might be due to the liquid flow within the wick. Noting that $\dot{m}$ is the mass flow rate and is related to the heat flow via the expression $Q = \dot{m} h_{lv}$, then rearranging and solving for the maximum heat flow Q_{HP} that can be dissipated in a heat pipe before the capillary limit is reached in a heat pipe, and evaporator wick respectively yields:

$$Q_{HP} \approx \frac{h_{lv}(2\sigma / r_p - \rho_l g L \sin\Omega)}{L(\mu_l /(\rho_l A \kappa) + 8\mu_v /(\pi \rho_v b^4))}$$

$$Q_{E\_wick} \approx \frac{2\sigma \rho_l A \kappa h_{lv}}{\mu_l L r_p} \qquad \text{(2.15a, b).}$$

In general, a meaningful prediction of Q relies heavily of the nature of the flow within the porous medium, and the knowledge of the permeability κ.

Boiling Limit

The boiling limit within a heat pipe is reached when bubble nucleation occurs within the evaporator wick. If these bubbles grow, they can act to prevent rewetting of certain areas of the evaporator and cause local temperature spikes and promote burnout. Typically, boiling is not favored due to these effects, and is thus considered a limit of operation. However several researchers have suggested enhanced performance when boiling is encountered.[47,48,52,53] Boiling in heat pipes and thermal spreaders is initiated by heterogeneous nucleation. More detail on the fundamentals of boiling will be presented in section 2.2.

2.2 Nucleate Boiling

A very effective mode of heat transfer within any system involving phase change is nucleate boiling. Nucleate boiling can be distinguished into two categories: homogeneous nucleate boiling which is driven by localized fluctuations (e.g. in energy and/or density) in a pure system otherwise in thermodynamic equilibrium, and heterogeneous nucleation which happens when the liquid is in contact with another phase, usually a solid. More in depth considerations can be found in textbooks by Faghri and Carey.[4,17,108]

2.2.1 Homogeneous Nucleation

Bubble nucleation within a liquid that is superheated is referred to as homogeneous nucleation. In particular, if a liquid is in a state near normal saturation conditions, localized fluctuations in density and energy may cause localized phase transitions thus yielding formation of vapor embryos. To determine if this bubble will nucleate and be stable in equilibrium with the surrounding liquid, a system in Fig. 2.7 is considered. At equilibrium, the chemical potential and temperature in each phase must be equal ($\mu_l = \mu_v$, $T = T_l = T_v$). Additionally, the pressure in the liquid and vapor are related by Young's equation as:

$$P_v - P_l = \frac{2\sigma}{r_{b,e}} \qquad \text{(2.16),}$$

where the pressure difference in vapor and liquid phases is balanced by the ratio of the surface tension σ and the equilibrium vapor bubble radius $r_{b,e}$.

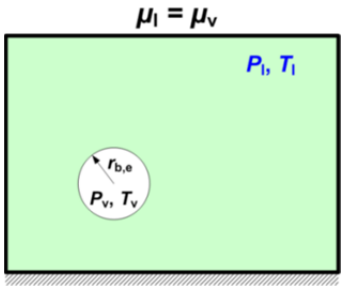

Fig. 2.7 Illustration of a nucleated vapor bubble of radius $r_{b,e}$ in thermodynamic equilibrium with the surrounding saturated liquid.

By considering the Gibbs-Duhem Eq. (2.17a), and integrating at constant temperature (saturation conditions, $dT = 0$), a relation for the chemical potential of vapor and liquid phases at equilibrium can be obtained

$$d\mu = -sdT + vdP$$

$$\mu_{v,e} = \mu_{v,sat} + \hat{R}T\left(\frac{P_{v,e}}{P_{sat}(T)}\right)$$

$$\mu_l = \mu_{l,sat} + v_l\left(P_l - P_{sat}(T)\right) \qquad (2.17a\text{-}c).$$

In these expressions $\hat{R}$ is the specific ideal gas constant, v_l is the specific volume of the liquid, $\mu_{v,e}$ is the chemical potential of the vapor at its equilibrium pressure $P_{v,e}$, μ_l the chemical potential of the liquid, T the temperature of the system, P_l the liquid pressure, and P_{sat} the saturation pressure at temperature T. To derive Eq. (2.17b, c) it is assumed the vapor behaves as an ideal gas, and that the liquid is incompressible. Equating these two relations based on the equilibrium condition, the vapor pressure at equilibrium is related to the liquid and saturation pressures as:

$$P_{v,e} = P_{sat}(T)\exp\left\{\frac{v_l(P_l - P_{sat}(T))}{\hat{R}T}\right\} \qquad (2.18).$$

Using Eq. (2.16) to substitute for P_l and realizing that $P_{v,e} - P_{sat}(T) << 2\sigma/r$, the expression can be approximated sufficiently well as

$$P_{v,e} = P_{sat}(T)\exp\left(\frac{-2\sigma v_l}{\hat{R}Tr_{b,e}}\right) \qquad (2.19).$$

Equation 2.19 has very important implications. Firstly, if Eq. (2.19) is rearranged to solve for $r_{b,e}$, it yields the radius of a vapor bubble that is in equilibrium with the defined saturation conditions. This relation can be further simplified by considering the linearized form of Clausius-Clapeyron equation Eq. (2.8a) and realizing again that the difference between $P_{v,e}$ and $P_{sat}(T)$ is small compared to the capillary term $2\sigma/r$ and that $\Delta v = v_v - v_l \approx v_v = 1/\rho_v$,

$$\frac{dP}{dT} = \frac{P_l - P_{sat}(T)}{T_{sat}(P_l) - T_l} = \frac{h_{lv}}{T\Delta v}$$

$$\frac{dP}{dT} = \frac{P_{v,e} - 2\sigma / r_{b,e} - P_{sat}(T)}{T_{sat}(P_l) - T} = \frac{\rho_v h_{lv}}{T_{sat}(P_l)}$$

$$r_{b,e} = \frac{2\sigma T_{sat}}{\rho_v h_{lv}(T - T_{sat}(P_l))} \qquad \text{(2.20a-c).}$$

Secondly, since the term inside the exponent is negative, $P_{v,e}$ is always smaller than P_{sat}, and because of the implications of Young's equation P_l is even smaller. Therefore, in order for a vapor bubble to be in equilibrium, both the liquid and vapor phases must be superheated relative to the normal saturation state. This is illustrated in the μ–P diagram of Fig. 2.8 in which the variation of μ with P along an isotherm is obtained from the van der Waals equation of state.[17,108] If the liquid is superheated (point a), then the vapor in equilibrium is also superheated (point b) relative to normal saturation conditions. This would not be the case for a flat interface where $P_{v,e} = P_l = P_{sat}(T)$.

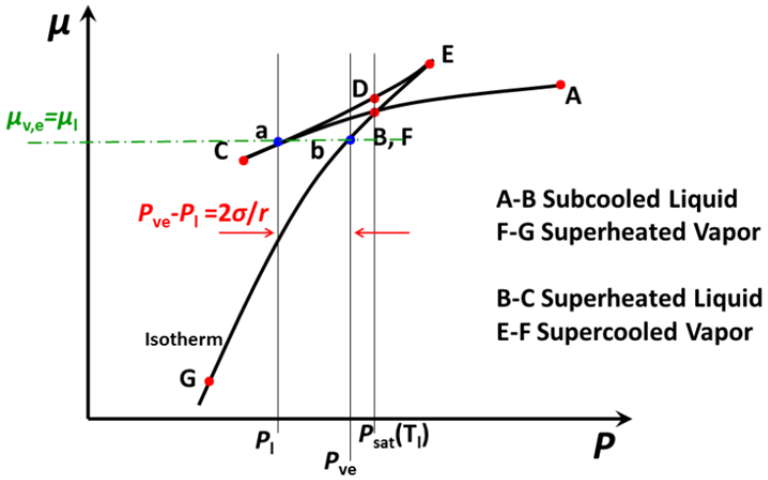

Fig 2.8 Chemical potential (μ) variation with pressure (P) along an isotherm as predicted by the equilibrium condition and the van der Waals equation of state.

Although the preceding analysis establishes conditions under which the bubble is in equilibrium with the surroundings, the stability of the system must be considered. Equation 2.21c is a result of stability analysis by considering the Gibbs free energy of the system shown in Fig. 2.7 that can be found in textbooks by Carey,[17,108] and indicates that a local maximum in ΔG exists at $r = r_{b,e}$.

$$\Delta G = G_f - G_O$$

$$\Delta G_e = \frac{4}{3}\sigma\pi r_{b,e}^2$$

$$\frac{\Delta G}{\Delta G_e} \approx 1 - 2\left(\frac{r}{r_{b,e}} - 1\right)^2 \qquad \text{(2.21 a-c).}$$

However, because at stable equilibrium the change in Gibbs free energy ΔG (before and after bubble formation) must be a minimum, the local maximum suggests that $r = r_{b,e}$ is unstable equilibrium. Any bubble with a radius smaller than $r_{b,e}$ will spontaneously collapse because the

system will tend to decreasing Gibbs free energy. Conversely, any larger bubble will spontaneously grow. Thus, if local fluctuations within any system are large enough to nucleate vapor bubbles larger than $r_{b,e}$ homogeneous nucleation will occur. In actual systems, the magnitude of fluctuations must be large, and one way they can be observed is by increasing the system superheat drastically at given saturation conditions.[17] Thus, in practical systems, homogeneous nucleation is not likely to be an integral mode of heat transfer; however, it is crucial in understanding the mechanisms of bubble growth and stability.

2.2.2 Heterogeneous Nucleation

Conversely to homogeneous nucleation which is bubble nucleation in a superheated liquid, heterogeneous bubble nucleation occurs where a vapor embryo is in contact with both solid and liquid phases and often depends on other factors than solely local energy and density fluctuations (e.g. interface shape). On an atomically smooth surface, requirements for vapor embryo nucleation are analogous to those discussed in section 2.2.1. This is also the case for surfaces that contain very well wetted cavities. For instance, at atmospheric conditions, superheat of around 300 ^{o}C is required for bubble nucleation.[17] In practice, this is not actually observed. On rough, porous, surfaces with crevices and cavities of various sizes the scenario is quite different and onset on nucleation occurs at much lower superheat (e.g. 10-20 ^{o}C at atmospheric conditions). This is typically attributed to the ability of cavities to trap vapor and noncondensable gases due to either cavity geometry (reentrant) and/or bubble dynamics.

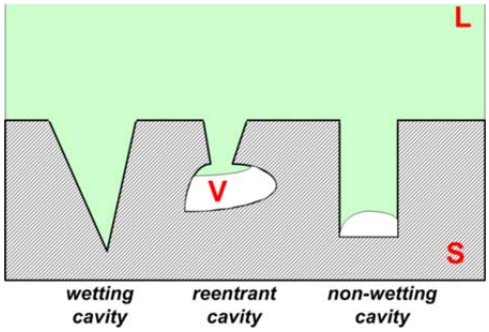

Fig. 2.9 Several types of cavities and crevices that can be encountered on surfaces used in phase change heat transfer applications.

Figure 2.9 illustrates several cavity geometries and types that can be encountered on surfaces commonly used in boiling applications. These cavities are often formed during the machining, and finishing processes. All these cavities can be pretty effective in trapping vapor/noncondensable gases because bubble nucleation from these surface features is a dynamic process and as the bubbles leave the surface, the process of re-wetting can cause vapor/gas to be trapped within cavities and further promote nucleation. In all cases, the trapped vapor/gas promotes evaporative heat transfer at the *S-L-V* interface, and thus reduces the required superheat for bubble nucleation. In well wetting systems however, bubbles can often be de-activated and re-activated thus yielding unpredictable heat transfer rates. In addition, in longer boiling processes, noncondensable gases are eventually completely replaced by vapor and a cavity may be deactivated in this manner as well if the remaining vapor were to condense or be replaced by liquid.

Reentrant type cavities (see Fig. 2.9) are designed in such a way to keep a nucleation site active practically indefinitely. This is attributed to the liquid-vapor interface profile inside the

cavity. Due to the curvature of the interface, the equilibrium vapor pressure in the vapor is higher than the saturation pressure as indicated by Eq. (2.22a), where now the exponential term is positive for the scenario of a liquid-vapor interface inside the reentrant cavity.

$$P_{v,e} = P_{sat}(T)\exp\left(\frac{2\sigma v_l}{RTr_{b,e}}\right)$$

$$P_l > P_{v,e} > P_{sat}(T) \qquad (2.22a, b).$$

By looking at the condition in Eq. (2.22b) and considering the diagram in Fig.2.8 again, both the liquid and vapor are subcooled at equilibrium. This implies that in order to condense out the vapor within a reentrant cavity, both the liquid and vapor need to be subcooled. This is not likely to occur in a superheated system and if properly designed, reentrant cavities should remain active indefinitely as long as some vapor is trapped within them.

To better understand heat transfer characteristics near a solid surface, it is necessary to determine the range of cavity sizes that remain active at a given superheat. In the analysis presented thus far, the liquid temperature is assumed uniform, however, near a solid heated surface this is not the case. Hsu developed a model to determine the range of active cavity sites, assuming that these cavities already have trapped vapor in them. The model is based on a system depicted in Fig. 2.10.[116]

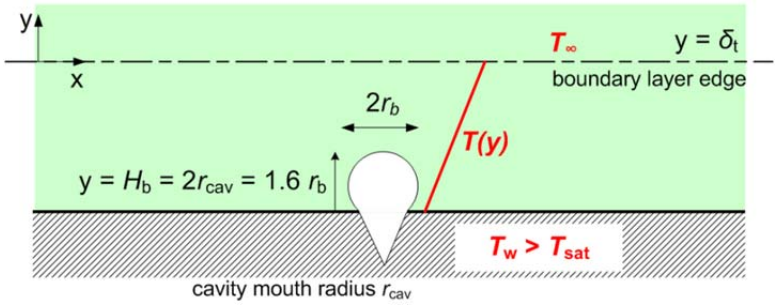

Fig. 2.10 Illustration of the system used in Hsu's analysis. Bubbles are assumed to nucleate from cavities with trapped vapor and mouth radius r_{cav}. At steady state, the temperature profile the bubble feels is not uniform due to the presence of a thermal boundary layer of thickness δ_t.

In his 1-D transient conduction model Eq. (2.23a-d) governed by the set of included boundary and initial conditions, Hsu assumed that within the boundary layer of thickness δ_t, there is a temperature profile T(y) due to the ebullition of the vapor bubble and the waiting period that precedes it. Outside and beyond δ_t he assumed that the bubbles released from the surface interact turbulently thus effectively mixing the surrounding liquid and yielding uniform temperature T_∞.

$$\frac{\partial\Theta}{\partial t} = \alpha_l\left(\frac{\partial^2\Theta}{\partial y^2}\right)$$

$$\Theta = T - T_\infty = 0 \,@\, t = o$$

$$\Theta = \Theta_w = T_w - T_\infty \,@\, y = 0$$

$$\Theta = 0 \,@\, y = \delta_t \qquad (2.23a\text{-}d).$$

In his analysis, Hsu also assumed the following ratio between the bubble height H_b, cavity mouth radius r_{cav}, and the bubble radius r_b, and that the wall temperature exceeded the saturation liquid temperature at the given conditions:

$$H_b = 2r_{cav} = 1.6r_b \tag{2.24}$$

Hsu suggested that the bubble would grow if the superheat everywhere around it was equal to or exceeded the equilibrium liquid superheat defined as:

$$T_{l,e} - T_{sat}(P_l) = \frac{2\sigma T_{sat}(P_l)}{r\rho_v h_{lv}} \tag{2.25}$$

The solution of Eq. (2.23) at steady state conditions yields a condition for cavities to be active. From further analysis, the range of active cavities can be expressed as:

$$\begin{Bmatrix} r_{cav,\min} \\ r_{cav,\max} \end{Bmatrix} = \frac{\delta_t}{4}\left[1 - \frac{\Theta_{sat}}{\Theta_w}\begin{Bmatrix} + \\ - \end{Bmatrix}\sqrt{\left(1 - \frac{\Theta_{sat}}{\Theta_w}\right)^2 - \frac{12.8\sigma T_{sat}(P_l)}{\rho_v h_{lv}\delta_t \Theta_w}}\right] \tag{2.26}$$

The above relation is plotted in Fig.2.11 and it indicates a range of cavities that are active in nucleate boiling at the given conditions. Any cavity smaller than $r_{cav,min}$ is inactive because not enough superheat can be supplied to nucleate a bubble. Alternatively, any cavity larger than $r_{cav,max}$ generates bubbles that protrude beyond the boundary layer of thickness δ_t; there the liquid is cooler at T_∞, and local condensation of vapor may occur and offset vaporization that occurs at the wall thus preventing the bubble from growing sufficiently to release from the surface thus making it also inactive.

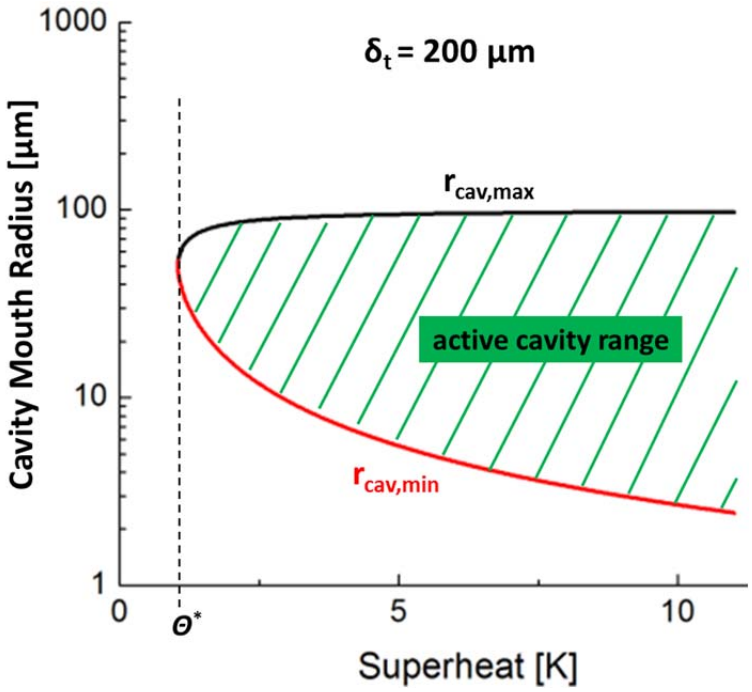

Fig. 2.11 Results of Hsu's analysis where the area shaded with lines indicates the range of active cavity sizes at a given superheat. A threshold superheat Θ^* for onset of bubble nucleation is indicated and strongly depends on the boundary layer thickness δ_t.

Hsu's model incorporates the effects of fluid properties, subcooling, and boundary layer presence and thickness, and is good at illustrating that near surfaces, bubble nucleation is influence by all these factors. In addition, the threshold superheat Θ^* at which nucleation occurs is governed by the boundary layer thickness, and increases as δ_t reduces. Thus, enhancing bulk convection away from the solid surface suppresses nucleation.

2.2.3 Heat Transfer in Pool Boiling Systems

In heat pipes and thermal spreaders, nucleate boiling is often considered detrimental. This is not the case in immersion cooling, thermal management of nuclear reactors, and power generation systems where nucleate boiling is a very effective mechanism of heat transfer. In this and the following section, the heat transfer coefficient in pool boiling systems is discussed, and some attention is paid to the heat transfer limitations (CHF condition) and the governing mechanisms. More in depth analysis can be found in a textbook by Carey.[17]

To understand the heat transfer characteristics of a pool boiling system, several factors must be taken into consideration. Since bubble generation occurs at the solid surface, nucleation frequency and bubble diameter at departure are relevant since they can be used to quantify the rate of energy dissipated via phase change. In combination with the knowledge of the nucleation site density, this can be combined to estimate the total heat flux dissipated, and if the surface temperature is known, the total heat transfer coefficient (HTC) of the system.

One of the most well-known theories of modeling nucleate boiling heat transfer was proposed by Rohsenow who developed a model assuming that heat is actually convected away via the liquid that is drawn to the surface by the vapor bubbles generated there. Based on this reasoning, Rohsenow proposed a single phase forced convection heat transfer model for correlating pool boiling data. This relation is of the form

$$Nu_b = \frac{hL_b}{k_l} = E\,\mathrm{Re}_b^{(1-r)}\,\mathrm{Pr}_b^{(1-s)} \qquad (2.27),$$

where $\mathrm{Nu_b}$ is the Nusselt number of the liquid with heat transfer coefficient h, thermal conductivity k_l, length scale of the bubble L_b, Reynolds number $\mathrm{Re_b}$, Prandtl number , fitting constant E, and fitting exponential parameters r and s.[17,117] By defining the bubble velocity as $u_\mathrm{b} = q/(\rho_\mathrm{v} h_\mathrm{lv})$, L_b as the bubble departure diameter defined as $L_\mathrm{d} = C_\mathrm{b}\theta\,[2\sigma/(g(\rho_\mathrm{l}-\rho_\mathrm{v}))]^{1/2}$ where C_b is a system specific constant, and the heat transfer coefficient in the Nusselt number relation as $h = q/(T_\mathrm{w} - T_\mathrm{sat}(P_\mathrm{l}))$, the final correlation by Rohsenow yields:

$$q_R = \mu_l h_{lv}\left(\frac{g(\rho_l-\rho_v)}{\sigma}\right)^{1/2}\left(\frac{1}{C_{sf}}\right)^{1/r}\mathrm{Pr}_l^{-s/r}\left(\frac{c_l[T_w - T_{sat}(P_l)]}{h_{lv}}\right)^{1/r} \qquad (2.28).$$

This is a modified version of the original expression where, $C_\mathrm{sf} = 2^{1/2} C_\mathrm{b}/A$ is a constant specific to the system depending on system geometry and wetting characteristics,[17,117] and the values of the exponents are recommended to be $r = 0.33$ and $s = 1.7$ ($s = 1$ is recommended for water).

More detailed considerations of these and other approaches for modeling heat transfer data can be found in a textbook by Carey.[17]

2.2.4 Mechanisms of Critical Heat Flux (CHF)

In pool boiling, the ultimate goal is to increase the maximum heat flux the surface can dissipate before burnout (CHF) and to do it with the smallest superheat yielding a high heat transfer coefficient (HTC). The latter of the two depends primarily on vapor bubble nucleation rate and density, and is thus limited by the rate at which phase change occurs. Underlying mechanisms for bubble nucleation and methods for increasing them have already been discussed in previous sections. Here, the focus is on the maximum heat flux condition, the CHF. In literature, typically two approaches are considered when defining CHF. The far field mechanisms involve hydrodynamics, and relative vapor and liquid flow far away from the surface that can ultimately cause CHF. On the other hand, some argue that CHF occurs due to near field mechanisms which include surface effects such as wetting and capillarity, and claim that these are responsible for the onset of CHF.

Far Field Mechanisms of CHF

One of the earliest theories was derived based on the analysis of Zuber who assumed that the CHF condition on horizontal infinite surfaces is reached when instabilities occur at the vapor/liquid interface of the vapor jets leaving the surface due to relative velocities of the two phases. According to Zuber, when the liquid/vapor interface becomes Helmholtz unstable, the vapor columns drag away the liquid from the surface preventing rewetting and CHF condition is reached.[60] He further postulated that CHF actually results from a combination of Taylor and Helmholtz instabilities, by observing that when CHF is approached from the transition boiling region, the vapor film is unstable at the interface giving wave-like nodes that form in a square pattern array spaced by Taylor unstable wavelength λ_T of a large liquid layer overlaying a vapor film.[17,60]

Based on these observations Zuber suggested that at CHF, the Helmholtz unstable wavelength λ_H is equal to Taylor wave node spacing λ_T, and that the unstable vapor columns have a radius equal to $\lambda_T/4$. He also claimed that only disturbances with wavelengths longer than the jet circumference are stable and grow, thus relating the vapor column circumference $C = \lambda_H$, and ultimately the critical Taylor wavelength to the Helmholtz unstable wavelengths as $\lambda_H = \pi\lambda_{T,c}/2$. From the instability analysis, the critical vapor velocity u_c and the and the critical wavelength $\lambda_{T,c}$ are determined to be

$$u_c = \left(\frac{2\pi\sigma}{\rho_v \lambda} \right)^{1/2}$$

$$\lambda_{T,c} = 2\pi \left(\frac{\sigma}{g(\rho_l - \rho_v)} \right)^{1/2} \qquad (2.29a, b).$$

Since the velocity of the vapor is significantly larger than the velocity of the liquid due to substantial density differences, the critical velocity can also be determined from the heat flux as

$$u_c = \frac{q}{\rho_v h_{lv}} \left(\frac{A_{total}}{A_{columns}} \right) \qquad (2.30),$$

where A_{total} is the total projected area of the square pattern unit cell of side length $\lambda_{T,c}$ containing the vapor columns, and $A_{columns}$ the total cross sectional area of vapor columns of radius $\lambda_{T,c}/4$.

Thus combining Eq. (2.29) and Eq. (2.30) and lumping all the numerical constants with some approximations into $\pi/24$, the CHF condition according to Zuber is:

$$q_{\max,Z} = 0.131\rho_v^{1/2} h_{lv} \left(\sigma g(\rho_l - \rho_v)\right)^{1/4} \quad (2.31).$$

Lienhard and Dhir further noted that CHF is better approximated when the Helmholtz unstable wavelength is equal to the most dangerous Taylor unstable wavelength $\lambda_{T,D}$,[61]

$$\lambda_{T,D} = \sqrt{3}\lambda_{T,c} \quad (2.32).$$

From this analysis they obtained an almost identical result (Eq. (2.31)) apart from the value of the numerical constant which can be written in terms of Eq. (2.31) as

$$q_{\max,L-D} = 1.14 q_{\max,Z} \quad (2.33).$$

Although derived into a practical analytical form, these relations fail to address effects of surface conditions (wettability, capillarity, etc.), and how near the surface effects can affect the CHF limitation. Thus, a major drawback of the hydrodynamic instability analysis is that the CHF is defined solely on the liquid and vapor properties and no geometry or solid surface properties are taken into account.

Near Field Mechanisms of CHF

In contrast to the hydrodynamic-far field CHF theories, other researchers have proposed that near the surface effects also govern the onset of CHF. Haramura and Katto proposed that hydrodynamic instabilities are important in defining the CHF condition on a wettable surface, but that these instabilities are even present prior to reaching CHF.[118] They suggested that the CHF is actually achieved when columns formed by small vapor jets merge over the interference region very near the surface (macrolayer) to form large vapor clouds that prevent surface rewetting. The only manner in which the surface can be rewetted is when these vapor clouds periodically release from the surface. Based on this reasoning, Haramura and Katto came up with the following relation for CHF on an infinite flat horizontal surface:

$$q_{\max,H-K} = 5.505 q_{\max,Z} \left(\frac{A_{vc}}{A_{surface}}\right)^{5/8} \left(1 - \frac{A_{vc}}{A_{surface}}\right) \left[\frac{\rho_l/\rho_v - 1}{\left((11/16)(\rho_l/\rho_v) + 1\right)^{3/5}}\right]^{5/16} \quad (2.34).$$

In this expression $q_{\max,Z}$ is the CHF condition defined by Zuber's relation in Eq. (2.31), and A_{vc} and $A_{surface}$ are the projected cross sectional area of vapor column within the microlayer on the heater surface and heater surface area respectively.[17,118]

Kandlikar explored the importance of surface effects, and solid-liquid interaction by considering the effects of wettability. In his model, Kandlikar suggested that CHF occurs locally near the heated surface, when bubbles generated by evaporation near the *S-L-V* contact line grow with a momentum high enough to overcome surface tension and gravitational retaining forces in the direction parallel to the surface.[119] When this condition is met, these vapor bubbles expand rapidly thus merging and blanketing the surface and causing CHF. The relation obtained by Kandlikar in Eq. (2.35) relates CHF to the contact angle θ as well angle of inclination Ω of an otherwise flat surface.

$$q_{\max,K} = \rho_v^{1/2} h_{lv} \left(\sigma g(\rho_l - \rho_v)\right)^{1/4} \frac{1+\cos\theta}{16}\left[\frac{2}{\pi} + \frac{\pi}{4}(1+\cos\theta)\cos\Omega\right]^{1/2} \quad (2.35).$$

Dhir and Liaw claimed that for very wetting systems ($\theta < \sim 20^o$) far field hydrodynamics govern the CHF as suggested by Zuber and Lionhardt and Dhir, while for systems with poorer wetting characteristics, CHF occurs due to merging of bubbles near the surface.[61,64,68,120]

In all the preceding theories on the CHF conditions analysis is focused on surfaces of infinite or large dimensions where the characteristic length scale exceeds the capillary lengths scale defined as

$$L_c = \sqrt{\frac{\sigma}{g(\rho_l - \rho_v)}} \quad (2.36).$$

which is defined by assuming the Bond number which is the ratio of the buoyancy forces to the surface tension forces is Bo = $\Delta\rho_{lv} g L^2/\sigma$ = 1.[17] For systems where $L < L_c$, the CHF onset is found to depend on surface size and shape and is typically defined as

$$q''_{\max} = q''_{\max,Z} f(L/L_c) \quad (2.37)$$

Lienhard and Dhir suggested that CHF on finite surfaces is affected by the number of vapor columns present.[121] For surfaces where the characteristic length L is smaller than three times the Taylor most dangerous wavelength $\lambda_{T,D}$ (Eq. (2.32)) and they related the heat flux to the CHF obtained by Zuber in Eq. (2.35) as

$$q_{finite\_L-D} = 1.14 q_{\max,Z}\left(\frac{\lambda_{T,D}^2 N_j}{A}\right) \quad (2.38).$$

Here N_j is the number of vapor jets on the finite surface, A the heater projected area. They reported enhancements up to 235 % of the $q_{\max,Z}$ for smaller heaters.[121]. Additional relevant works will be discussed in the context of Chapter 4.

2.3 Summary

The purpose of this chapter is to address some theoretical and practical limitations in phase change heat transfer encountered in evaporation and boiling systems. In heat pipes and vapor chambers, typically capillary and boiling limitations along with high thermal resistances of integral components diminish the heat transfer performance with respect to the kinetic theory limits. Similarly, in pool boiling, nucleation site density and bubble release frequency, as well as hydrodynamic and surface effects can act to limit heat transfer performance. All these basic principles discussed here will serve as either a reference to related works or as background to the scope of the work presented in Chapters 3 and 4 where the focus will be on enhancing heat transfer performance via phase change in wick structures and pool boiling systems by engineering surfaces with micro and hybrid micro/nano structures.

3. Enhanced Heat Transfer in Biporous Evaporator Wick Structures

In this chapter, phase change heat transfer performance of silicon made structures composed of arrays of microfabricated pin fins is explored. These structures can be characterized by two length scales intended to simultaneously increase the capillary pressure and reduce flow drag in order to dissipate large heat fluxes. Also, the large number of pins is intended to produce menisci with many thin liquid film contact lines where phase change heat transfer would be promoted. The results of a systematic study of these structures is presented and discussed here.

3.1 Background, Motivation and Survey of Previous Work

The integration of graphical processing units (GPUs) with central processing units (CPUs) as well as the use of multi-core processors can pose two severe challenges in thermal management, namely: (i) how to cool local hot spots on the order of 1 mm in size with power densities exceeding 500 W/cm^2; and (ii) how to dissipate more than 100 W over a chip area of about 1 cm^2, i.e. for average chip power densities exceeding 100 W/cm^2 [6,28] Vapor chamber heat pipes have received attention for thermal management of these processor chips since they have a high heat transfer coefficient for heat spreading and require no external source of power or liquid pumping making them ideal for portable or handheld devices.[8,29] Ideally, a heat pipe spreader is designed such that it can dissipate a given heat flux while maintaining a minimal temperature rise. This heat dissipation capability depends significantly on the performance of the evaporator section of the heat pipe, which is typically composed of a porous wick.

In general, two factors restrict the operating envelope of a heat pipe, namely: (i) the capillary suction limited mass flow rate, and (ii) the initiation of nucleate boiling in the evaporator wick. Evaporator wicks are typically made of sintered copper particles. In these types of structures, the twin goals of increasing both the dissipated heat flux and the overall heat transfer coefficient are in conflict.[29] Reduction of particle size and increase in wick thickness favor higher capillary driven mass flow rate, thus increasing the heat flux dissipated. However, particle size reduction also increases liquid flow resistance and the density of point contacts between particles thus reducing the effective thermal conductivity of the wick. These and other factors for the optimal design of porous wick structures have been examined in great detail by Faghri, and Dunn and Reay.[4,50] With these tradeoffs in mind, there is likely an optimum particle size, wick height, and wick porosity that maximize the heat transfer coefficient and the heat flux that can be dissipated.

During heat pipe operation, most of the heat transfer at the top surface occurs in the liquid region (thickness ~ few microns) near the triple-phase contact line.[35,36,122] The observed heat transfer coefficient is governed by the area coverage and thickness of this thin liquid film region, and the effective conductivity of the porous matrix.[51] Figure 3.1 shows an idealized sketch of the thermal resistance network of a sintered copper particle wick operating at steady state conditions. Here, $R_{substrate}$ is the substrate thermal resistance on which the particles are sintered, R_{matrix} is the effective thermal resistance of the particle/liquid matrix, R_{film} is the thermal resistance of the thin liquid film that forms at the meniscus and R_{int} is the thermal resistance of the liquid/vapor interface. Additionally, Q, T_{vap} T_{wall}, and $T_{substrate}$ are the heat flow, vapor temperature, temperature at the wall in contact with the liquid, and temperature at the base of the substrate respectively. Thus, given that the interfacial thermal resistance is not the

dominant resistance in such a system,[4] one can tune other resistances to maximize wick performance.

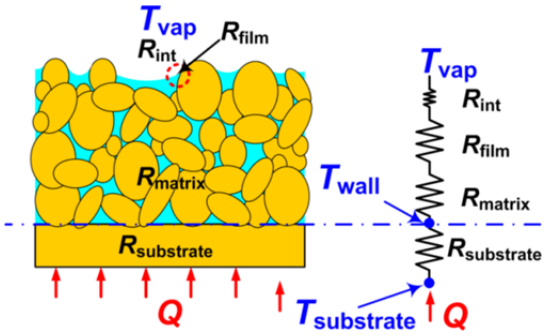

Fig. 3.1 Thermal resistance network for a typical sintered copper particle porous wick structure; Q is the applied power, T_{wall} is the temperature at the base of the particle matrix, $T_{substrate}$ is the temperature at the base of the wick substrate, $R_{substrate}$ the thermal resistance of the substrate, R_{matrix} is the overall thermal resistance of the particle/liquid matrix, R_{film} is the resistance of the liquid thin film that forms at the meniscus, R_{int} is the thermal resistance of the liquid/vapor interface, and T_{vap} is the vapor temperature.

In the introductory Chapter 1.1, a literature overview was given comparing performance of monoporous and biporous wick structures. Wicks with sintered particles in the range 40-400 μm and typically of 1-4 mm thickness have been tested by several researchers.[46,51,55,56,59] The highest observed heat transfer coefficient in the evaporative mode of heat transfer using sintered particle wicks is 12.8 W/cm^2-K at an applied flux of 8.3 W/cm^2.[55] All other wicks that display capillary evaporation show values in the range 1-10 W/cm^2-K. In other structures, nucleate boiling is observed at relatively low superheats, accompanied by enhancements in HTC.[46,52–54,56] As already discussed in the introductory chapter, the benefits of implementing biporous structures (the work of Semenic et al,[56] Zhao and Chen,[46] and Cao and Chen [59]) have been reflected through increased heat transfer performance in mainly CHF performance. Significant increases in HTC have not been demonstrated in biporous structures, presumably due to low solid thermal conductivity of such structures and thus a large thermal resistance of the liquid/particle matrix (R_{matrix}) as illustrated in Fig. 3.1.

The present study implements designed biporous structures to simultaneously increase the heat dissipation capacity as well as the heat transfer coefficient of the evaporator wick. In order to avoid point contact between particles that yield increased thermal resistances in sintered particle structures, establish greater control over porosity and pore size, and allow for a more systematic investigation of performance, bulk crystalline silicon wick structures composed of pin fin arrays periodically separated by large microchannels are implemented in this study. These structures are developed using standard microfabrication techniques and engineered to increase capillary pressure and surface area for evaporation, as well as to reduce the maximum thickness of liquid film through which conduction occurs at the liquid-vapor interface near the meniscus. This geometry is motivated based on the predictions and findings of other works,[39,40,43] and the hypothesis that through a combination of the fin effect (enhanced surface area) and microstructuring, enhanced heat transfer performance can be achieved. In the following sections, heat transfer performance is quantitatively measured in the evaporative and nucleate boiling regimes to identify the optimum wick parameters, such as pin fin characteristic size, pin fin spacing, wick height, and microchannel width for fixed wick porosity. Furthermore, applicability of these geometries to amelioration of hotspot cooling in microprocessors is examined by considering heat sources of varying area.

3.2 Materials and Methods

3.2.1 Parameter Range

As illustrated in Fig. 3.2(top), the wicks of depth H are fabricated in the form of parallel microchannels of width w that periodically separate arrays of micro pin fins. The pin fins of square cross section and size d (throughout the text we denote this size d as 'diameter d') and spacing p are arranged in an in-line array of width D. Table 3.1 shows the parameter space over which the experiments are performed. Pin fin array width D is varied from ~150 μm to ~290 μm in order to maintain the same porosity among samples ($\phi \approx 0.79 \pm 0.02$). This is done so that the effective thermal resistance of the solid pin fin wick R_{pins} and the bulk liquid thermal resistance R_L in Fig. 3.2(bottom) are approximately constant among samples of similar depth H. In addition, samples are made so that the wick substrate thermal resistance $R_{substrate}$ in Fig. 3.2(bottom) is not the dominant resistance in the network. In this way, by varying the size and thus the surface area of the pin fins it is possible to determine how the thin liquid film thermal resistance R_{film} affects the overall performance of the wick. To arrive at values for the pin fin diameter d and pore size p we note that the thermal resistance of a 5 μm-thick planar layer of water is ~0.074 cm^2-K/W (approximate value for the desired performance of the wick). By choosing the pore size p to vary from 28 μm down to 4.9 μm, we can generate a range of meniscus film thicknesses that yield thermal conductances in the range of the desired performance. Total number of pins per cm^2, total pin surface area, and substrate and wick thermal resistance (Eq. 2.6b) are also summarized in Table A1.1 of the Appendix.

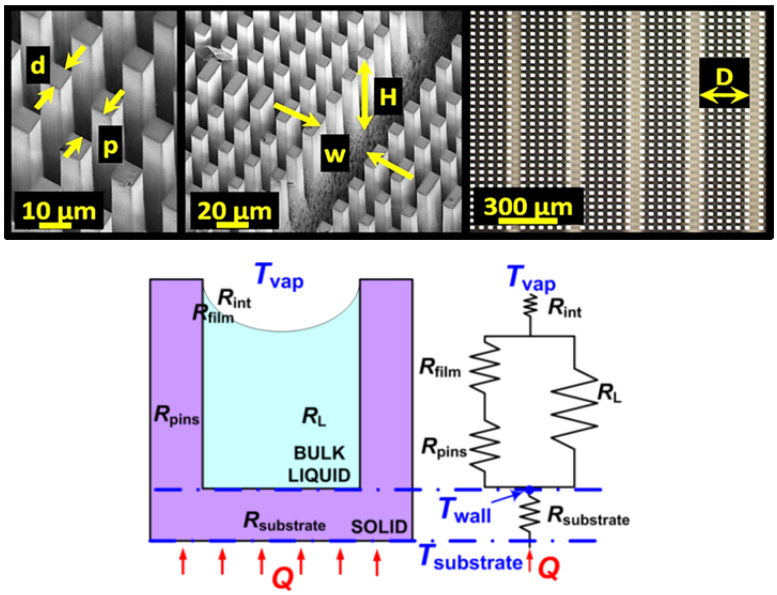

Fig. 3.2 (top) Cross-section and plan views of the evaporator geometry showing arrays of pin fins with periodic microchannels; Here d is the side length of a pin of square cross section, p is the pin spacing, H is the depth of the wick, w is the channel width, and D is the width of the pin fin array; (bottom) Heat flow path and the corresponding thermal resistance network for the silicon wick structures investigated here: Q is the applied power, T_{wall} is the temperature at the base of the pin fin array, $T_{substrate}$ is the measured substrate temperature, $R_{substrate}$ is the thermal resistance of the substrate from which the pins are protruding, R_{pins} is the thermal resistance of the pin array, R_L is the bulk liquid resistance which fills the pores, R_{film} is the resistance of the liquid thin film that forms at the meniscus, R_{int} is the thermal resistance of the liquid/vapor interface, and T_{vap} is the vapor temperature.

Table 3.1 Dimensions (in μm) of the various length scales defining the wick geometry.

Pin fin array width ***D***	**Microchannel width** ***w***	**Pin fin diameter** ***d***	**Pore size** ***p***	**Wick depth** ***H***
156	30	3.1	4.9	135
152	30	6.9	9.2	145
144	31	13.5	16.5	56, 145, 207, 243
232	61	7.1	8.5	150
272	61	15	16.8	149
264	61	22.5	24	152
288	61	29	28	158

3.2.2 Sample Fabrication and Preparation

Figure 3.3 (left) illustrates the process used to fabricate test samples on a 100 mm diameter (~525 μm thick) silicon wafer. Photolithography using positive photoresist is used to define regular pin fin array patterns over a 2 × 2 cm^2 area. Subsequently, deep trenches are etched in the wafer using inductively-coupled SF_6 plasma (Fig. 3.3a-c). The photoresist is then removed by immersion in photoresist stripper (FujiFilm PRS3000) and cleaned with piranha (H_2SO_4-H_2O_2, 4:1) and de-ionized water. A thin silicon dioxide layer is deposited on the wafer in order to increase wettability. This is achieved by Plasma-Enhanced Chemical Vapor Deposition (PECVD) with oxygen plasma inside an Oxford Plasmalab-80plus System at 350 ^oC. Ellipsometry is used to measure the film thickness at the base of the microchannels of the pin fin array. The nominal measured thickness across samples is approximately 200 nm. This yielded an average contact angle of 12 ± 2.5 degrees measured by a Kruss goniometer among different samples in contact with DI water. The oxide thickness is not measured along the side of the pins, but energy-dispersive x-ray spectroscopy is performed to confirm the presence of oxide at multiple locations along the pins. Resistive heating is accomplished by depositing a thin ~250 nm layer of Indium Tin Oxide (ITO) on the back side of the silicon substrate. Lithography is used to define the heater area of 1 cm^2 (Fig. 3.3d), and ITO is deposited using a radio frequency argon plasma sputtering chamber. A similar process is used to deposit ~1.5 μm of copper, overlapping the edge of the ITO heater, which defines the electrodes. An array of 3 special limit of error (SLE) Omega Engineering T-type thermocouples spaced ~2 mm apart are bonded to the heater using electrically insulating epoxy ($k_{epoxy} \approx 2.0$ W/m-K).

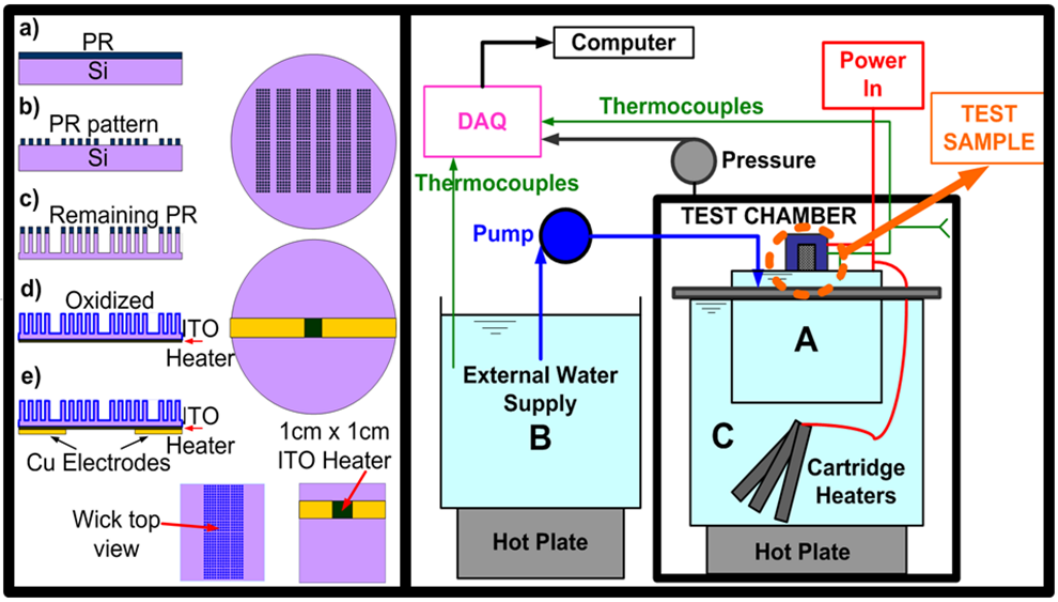

Fig. 3.3 (left) Schematic of fabrication process used to generate the evaporator wick geometries: (a) Photoresist (PR) is deposited (b) Lithography is used to define and develop the pattern (c) Deep silicon etching is used to obtain a wick of desired depth (d) After cleaning, the sample is oxidized to improve wettability, and an ITO heater is deposited subsequently (e) Copper electrodes are deposited and the sample is cut to a desired size; (right) Experimental apparatus used to measure the heat transfer performance of the evaporator wicks.

3.2.3 Experimental Setup

Figure 3.3 (right) shows a schematic of the experimental system for measurement of wick performance. In order to ensure that the wick is not flooded with liquid, but draws up only as much liquid as necessary to maintain it wetted, the experiments are performed with the wick suspended in a vertical orientation. The test sample is immersed in a liquid reservoir (labeled A in Fig. 3.3 (right)) such that the bottom edge of the ITO heater is 5 mm above the reservoir liquid level. The reservoir is replenished by liquid supply from another beaker (B) in which water is maintained at ~100 ^{o}C. The temperature of the reservoir is kept constant by immersing the reservoir in a tank (C) maintained at ~100 ^{o}C by a hot plate as well as immersed cartridge heaters. The liquid level in the reservoir is maintained by using an overflow system.

To replicate the saturation conditions in a vapor chamber heat pipe, experiments are conducted in a saturated water vapor environment at $T_{sat} \approx 100$ ^{o}C and $P_{sat} \approx 1$ bar. This is achieved by evacuating the test chamber multiple times, sealing it, and boiling the water from the overflow tank to evaporate until the chamber pressure is close to 1 bar. Thermocouples monitor the temperatures at multiple locations near the wick sample surface, in the water reservoirs, and in the vapor atmosphere as illustrated in Fig. 3.3 (right). Typically, the temperature everywhere inside the chamber attains a value between 96 ^{o}C – 100 ^{o}C after 6 cycles of pumping out the chamber. This is an indication that the chamber atmosphere consists mainly of water vapor. Electrical power is then applied via a power meter (Agilent N5750A DC Power Supply – 150V/5A/750 W) at regular intervals to the ITO heater while simultaneously measuring temperature at various points along the height of the sample. Vapor is allowed to bleed out of the system through a one-way valve in order to maintain a constant pressure.

From these experiments we extract the heat transfer coefficient based on the heater area as follows:

$$h = HTC = \frac{Q / A_{heater}}{T_{wall} - T_{vap}} \quad (3.1).$$

Here, T_{wall} is the wall temperature at the wick base in contact with the liquid, T_{vap} is the saturation temperature of water vapor at ~1 bar ($T_{vap} \approx 100\ ^{o}C$), A_{heater} is 1 cm^2 in all tests except when otherwise specified, and Q is the power dissipated by phase change heat transfer. The uncertainty analysis of all the measurements discussed in this chapter is included in Appendix A.1.

3.3 Results and Discussion

3.3.1 Effect of Wick Depth on Performance: Predominantly Evaporative Regime

Wick samples are tested in a vertical orientation as depicted in Fig. 3.3 (right). When water saturates the wick, the thermal resistance of the bulk liquid R_L between the pins as seen in Fig. 3.2(bottom) is roughly two orders of magnitude higher than the resistance through the silicon pins R_{pins}. Therefore, most of the heat travels through the solid substrate and the pin structures to the thin liquid film that forms at the meniscus where the bulk of the evaporative heat transfer occurs. With these considerations in mind, the resistance network in Fig. 3.2(bottom) can be simplified as a series network with R_L omitted and including the substrate, pin fin array, thin liquid film, and interfacial thermal resistances designated as $R_{substrate}$, R_{pins}, R_{film} and R_{int} respectively. Furthermore, if we only consider the thermal resistances in the pin fin array of the wick of 1 cm^2 area we obtain

$$\frac{1}{g_{pins}} = \frac{H}{(1-\phi)k_{Si}} \quad (3.2),$$

where the term on the right hand side is the thermal resistance of the pin fin array R_{pins}. Here, H is the depth of the pin array, ϕ the porosity, k_{Si} the thermal conductivity of silicon at 115 ^{o}C and g_{pins} is the thermal conductance of the pin fin array. As channel depth is increased from H = 56 μm to H = 243 μm in experiments considered here, the conductance of the solid pins with porosity $\phi \sim 0.79$ drops from $g_{pins} = 1/R_{pins} = 43.2$ W/cm^2-K down to $g_{pins} = 9.9$ W/cm^2-K. For the range of pore sizes investigated here, the effective liquid film thickness at the meniscus has been estimated by several investigators to be under 5 μm,[39,51] giving a thin film conductance to be $g_{film} = 1/R_{film} = 13.6$ W/cm^2-K. Therefore, pin fin arrays deeper than 145 μm ($g_{pins} = 1/R_{pins} < 15.9$ W/cm^2-K) contribute the dominant thermal resistance. This implies that in the range of depths considered here, a transition is likely to occur in the thermal resistances that dominate (between R_{film} and R_{pins}) and thus yield different trends in heat transfer performance among samples investigated.

Figure 3.4 (top) shows the effect of varying the depth H of the micro pin fin structures on wick performance for the case d = 13.5 μm, p = 16.5 μm, w = 31μm and porosity $\phi \sim 0.79$. Predominantly evaporative heat transfer is observed only in wicks of depth H = 145 μm and below. Here we presume that bubble nucleation at the measured temperatures is suppressed due to high wettability of water on SiO_2 precluding vapor trapping.[67] For these samples, the pin array conductance estimated by Eq. (3.2) ($g_{pins} > 15.9$ W/cm^2-K) remains comparable or larger than the liquid film conductance g_{film}. In this scenario, the film conductance governs the heat transfer and the initial slope of the curves remains independent of wick depth (similar slopes for H = 56 μm and H = 145 μm).

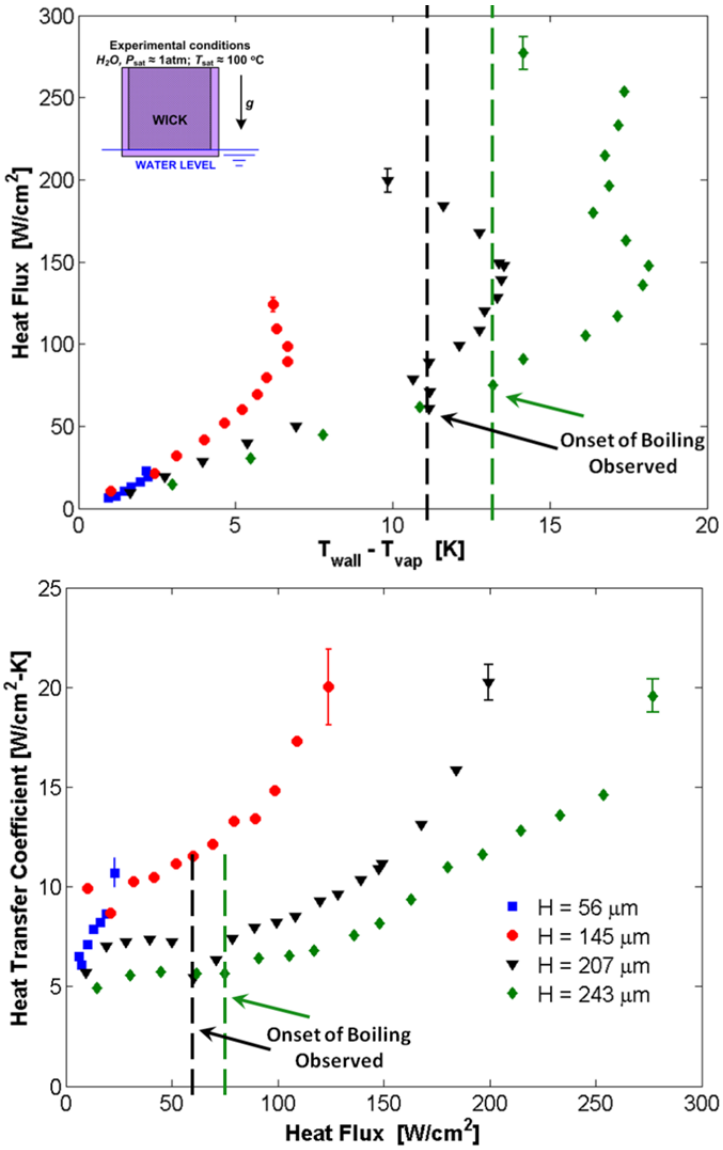

Fig. 3.4 (top) Heat transfer data for a wick tested in vertical orientation with pin fin arrays of variable depth *H,* for constant pin fin size d = 13.5 µm, pore size p = 16.5 µm, pin array width w = 144 µm, and microchannel width w = 31 µm; (bottom) Heat transfer coefficient variation with wick depth *H*. Only error bars at dryout heat fluxes are shown for each data set. The inset image shows experiment conditions and wick orientation (vertical).

At low to moderate heat fluxes, when the wick is saturated with liquid (Fig. 3.5), the liquid film conductance g_{film} is a function of thin liquid film thickness and the total length of the contact line, i.e. the total area of the thin liquid film surrounding the pin. As the applied heat flux and mass flow rate increase the capillary limit is reached near the center of the heater and local dryout occurs evinced by a visible dry spot on the wick surface. We conjecture that there must be a radial variation of the liquid level away from the dry spot, rising from zero at the edge of the spot to the top of the pin fins far away from the spot, as depicted in Fig. 3.5. As a result, the effective area of thin film is significantly enhanced just prior to dryout, with evaporation occurring in the thin film around the pin fins as well as from the base on which the pin fins stand.

In addition, at high heat fluxes the contact angle is at the minimum possible value, the receding contact angle for water on SiO_2. It is possible that this recession further thins down the liquid film where the bulk of the evaporation occurs, and slightly increases the film thermal conductance. We presume that these two effects working in tandem increase the slope at high heat fluxes, most clearly apparent for $q > 90$ W/cm^2 in a wick of $H = 145$ μm (Fig. 3.4 (top)), and translate into a higher heat transfer coefficient (Fig. 3.4 (bottom)). Once observed the dry spot remains stable and gradually grows to cover up to about 10 % of the heater area. Further increase in heat flux causes the dry spot to spread dramatically and blanket the whole surface of the wick with vapor. We deem this as the dryout heat flux and observe a sudden increase in average superheat. At this point the wick can no longer be considered operational. In most samples we observe the dry spot to occur and be stable within 10–15% of the dryout heat flux. The dryout condition corresponds to the last data point for each sample plotted in Fig. 3.4. From these experiments we observe that in the predominantly evaporative regime of heat transfer, dryout occurs at larger values of applied heat flux as the pin fin height is increased from 56 μm to 145 μm, presumably due to the increased cross-sectional area available for flow through the taller microchannels.

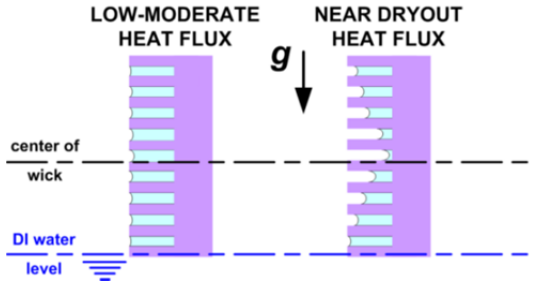

Fig. 3.5 Sketch of the wick and liquid level based on observations at low to moderate and high heat fluxes.

3.3.2 Effect of Wick Depth on Performance: Predominantly Boiling Regime

As the wick depth H is increased beyond 145 μm, the conductance of the pin array g_{pins} decreases (see Eq. (3.2)) and is lower than the liquid film conductance g_{film}. The initial slope of the heat transfer curve becomes a function of the pin fin height, as seen in Fig. 3.4(top) for $H =$ 207μm and $H = 243$ μm. Consequently, high values of superheat are observed at relatively low heat fluxes (~ 50 W/cm^2). Here, nucleate boiling is visually observed at several locations on the wick as indicated by the dotted lines in Fig. 3.4. For samples that demonstrate nucleate boiling, the heat transfer curve has two distinct slopes: one corresponding to predominantly evaporation at low to moderate heat fluxes, and another corresponding to predominantly nucleate boiling at high heat fluxes. The slope of the heat transfer curve in the nucleate boiling regime is increased due to enhanced thin film area caused by ebullition of the generated bubbles. Escaping bubbles are constrained in the lateral direction and elongated along the pores of the wick. This creates a thin film along the height of the pin fin instead of only near the meniscus as in evaporation. The thickness of the film on the sides of the pins depends on the bubble velocity and the pore size.[123,124] While it is generally observed that boiling in microchannel based heat pipes causes flow blockage and stops heat pipe operation, in the present study, a steady boiling regime could be maintained for heat flux increases up to 185 W/cm^2 beyond nucleation incipience for 1 cm^2 heaters. The occurrence of nucleate boiling in biporous particle structures and layered meshes has been previously shown to yield high-performance wicks.[46,52–54,56] The structure and dynamics of the flow have remained a matter of conjecture. In this study we supplement the

heat transfer measurements with flow visualization of a stable nucleate boiling regime that is observed.

The visualization of boiling in wick structures is performed outside the test chamber using a Fastec Imaging (IN100M2GB) CCD camera. Images are taken at 250 frames per second. Figure 3.6 shows the boiling process for a wick of depth H = 207 µm, with d = 13.5 µm pin fins, p = 16.5 µm pore size, and w = 31µm microchannels. At a heat flux of 52 W/cm^2, bubble nucleation occurs in the microchannels (Fig. 3.6a), with the bubbles typically growing to a diameter equaling the combined width of two pin fin arrays (~ 350 µm) before collapsing. As the heat flux is increased to 107 W/cm^2, the superheat increases. Bubbles nucleating in microchannels collapse at smaller sizes, while nucleation also occurs in the smaller pores formed by the pin fins (Fig. 3.6b). In actual experiments, these bubbles appear and disappear very rapidly (~0.01s). As the heat flux is further increased to 136 W/cm^2, the frequency of bubble generation increases. Bubbles are intermittently formed at discrete nucleation sites on the wick surface, and collapse when they grow beyond the wick height. In addition to these discrete locations, large areas in the pin fin array are seen to nucleate simultaneously (large dark spots in Fig. 3.6c), resulting in audible loud bursting and violent ejection of liquid droplets. This bursting phenomenon causes the slope of the data to increase abruptly or even become negative giving a significant increase in heat transfer coefficient that causes a reduction in average superheat. This is evident in Fig. 3.4 (top) for the wicks of depth H = 207 µm and H = 243 µm, at average values of superheat of ~13 K and ~18 K respectively, where this bursting phenomenon is initially observed. This phenomenon commences at a larger average superheat than that corresponding to the isolated bubble nucleation indicated by the dashed lines in Fig. 3.4.

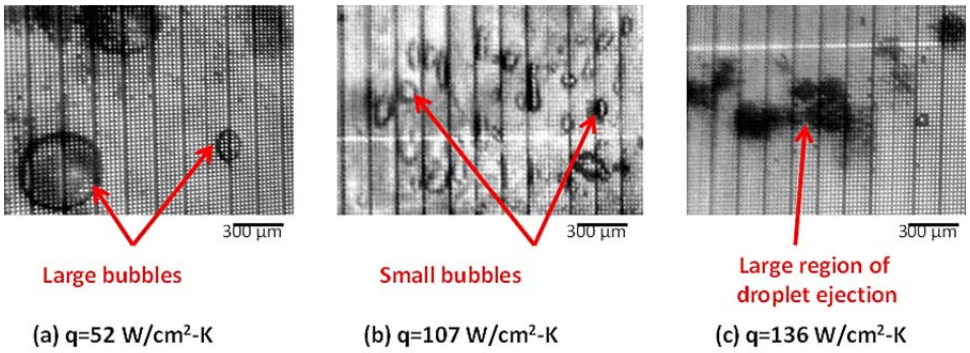

Fig. 3.6 Nucleate boiling at various heat fluxes for d = 13.5 µm, p = 16.5 µm, H = 207 µm, and w = 30µm.

Figure 3.7a-f shows one such cycle of bursting and receding of the wetting front followed by advancement of the wetting front back towards the nucleation zone. Immediately after droplet ejection, a large dry area is formed, as seen in Fig. 3.7a. In subsequent frames (Fig. 3.7b-e), motion of the liquid-vapor-solid contact line can be discerned, indicating liquid flow towards the nucleation area and rewetting of the surface, until the next burst occurs (Fig. 3.7f). This process of rewetting shows that capillary pumping continues to be active even after the onset of nucleate boiling, and indicates that this regime of bubble nucleation is not an operating limit in such biporous structures. To the best of our knowledge, this regime of stable boiling has not yet been visually observed in other thin liquid film wick structures. As the heat flux is increased the ejection frequency increases and the motion of the front can no longer be seen. At this point, the bubble ejection frequency is very high and the area where the nucleation occurs is so large that

the wick can no longer supply the liquid to the surface. Here, the boiling limit is reached and the wick dries out.

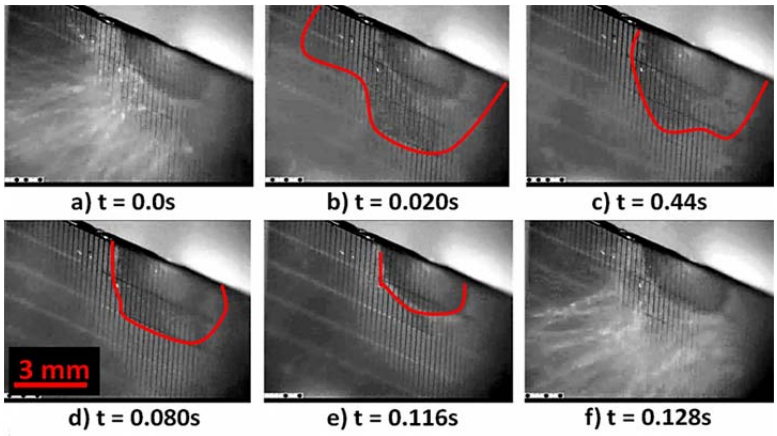

Fig. 3.7 Burst sequence at an imposed heat flux of ~230 W/cm^2: (a) Bubble bursting and violent ejection of liquid droplets (b) Formation of dry area around nucleation site. (c) - (d) Advancing wetting front. (e) Liquid almost fully rewetting the wick. (f) Start of next burst cycle.

3.3.3 Effect of Wick/Heater Area Ratio on Performance

As the applied heat flux is increased, the capillary pressure increases in order to accommodate for the increased rate of evaporation.[4] This process induces entrainment of liquid towards the area directly above the heater, where the surrounding region acts as a liquid reservoir. Therefore, for a given wick structure, the ratio of the total wick area to the heater area influences the dryout heat flux. The area over which evaporation occurs is difficult to determine visually; investigators usually resort to rough approximations for the evaporation area,[55] or report the applied heat flux based on the heater area.[48,49] Figure 3.8 shows a sketch of the general arrangement of the heater area (on the back of the wafer) within the wick.

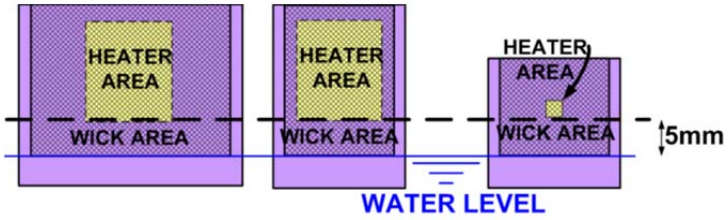

Fig. 3.8 Sketch of arrangement of wick and heater surfaces with respect to the liquid reservoir: (a) A_{wick}=3.8 cm^2, A_{heater}=1 cm^2 (b) A_{wick}=1.5 cm^2, A_{heater}=1 cm^2 (c) A_{wick}=1.1 cm^2, A_{heater}=0.0625 cm^2.

In one case, the wick dimensions above the reservoir liquid level are 1.9 × 2 cm^2, with the 1 cm^2 heater aligned centrally within the wick, with the reservoir level 5 mm below the heater edge. In another case, the wick area is 1 × 1.5 cm^2, and is aligned on three sides with the 1 cm^2 heater. Figure 3.9 shows the effect of this difference in wick and heater area on the wick performance. All data presented in Fig. 3.9 are for a single wick geometry with pin fin size d = 7.1 µm, pore size p = 9.0 µm, channel width w = 30 µm, and wick depth $H \approx$ 149 µm. The larger area of the wick in the second case yields an improved dryout flux of 119.6 (± 4.2) W/cm^2 compared to 73.6 (± 2.6) W/cm^2 for the first case. The heat transfer coefficient also increases from 9.8 (± 0.7) W/cm^2-K to 13.4 (± 1.5) W/cm^2-K at a heat flux of approximately 60 W/cm^2 due to an increase in the effective contact line length for evaporation in the larger wick. The data

suggests that larger wick-to-heater area ratios ought to allow for higher heat fluxes to be dissipated, since cooler liquid from the surrounding areas can penetrate deeper into the central hotspot before evaporating. This has particular relevance to the cooling of local hotspots within a microprocessor, where high heat fluxes on the order of hundreds of W/cm^2 may be generated.[6,8,28] In order to simulate a single hot spot on a chip, we fabricated a 2.4mm × 2.6mm heater on a 1.1 cm^2 wick, for an area ratio of about 18:1 (filled red circles in Fig. 3.9). For this heater size, evaporation predominates for heat fluxes as high as ~160 W/cm^2 beyond which nucleate boiling occurs until the dryout flux of 733.1 (± 103.4) W/cm^2 is reached. With this performance, thermal non-uniformities that may arise over small areas (on the order ~ 1mm^2 or less) of a microprocessor chip can be managed.[6,28] This effect may also explain the high dryout fluxes (~600 W/cm^2) observed by other investigators for area ratios of approximately 25:1 and 16:1 respectively.[48,49]

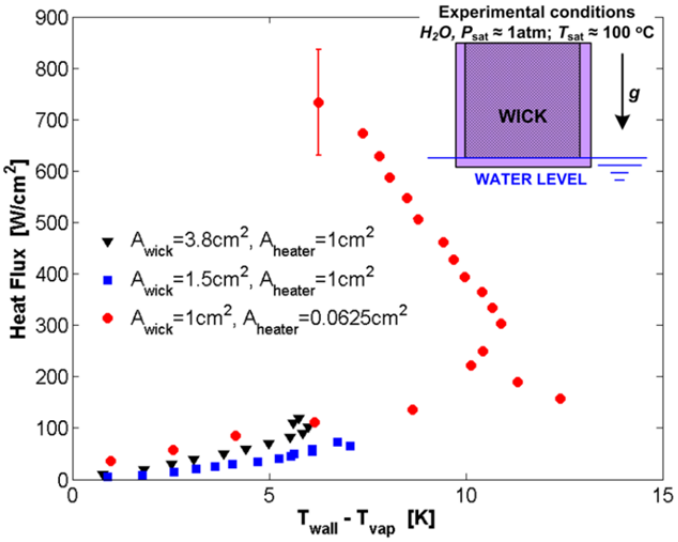

Fig. 3.9 Effect of the ratio of wick surface area to heater area, for d = 7.1 µm, p = 9.0 µm, w = 30 µm, and H = 149 µm. Only the error bar at dryout heat flux is shown for each data set, where the two sets with lower attained heat fluxes have error bars that are smaller than the marker size. The inset image shows experiment conditions and wick orientation (vertical).

3.3.4 Effect of Pin/Pore Size on Performance

In the interline region (length ~ several hundred nm) of a meniscus,[30] high mass (heat) fluxes occur due to enhanced fluid flow towards the contact line, modifying the film profile and the apparent contact angle.[112] However, this region occupies a small fraction of the total film length for large menisci (radius > few µm). Therefore, the major portion of the heat transfer occurs through conduction in the microscale liquid film (thickness ~ few µm) of constant curvature.[39,40,43] In order to increase total heat flux, one needs to increase the number of such regions by reducing pore size.

Data in Figures 3.10 (top and bottom) show the effect of varying the pin fin size d and spacing p on the heat transfer curve, for channel depths H in the range between 135 µm and 158 µm as summarized in Table 3.1, and channel widths w of 30 µm and 60 µm. Expectedly, from Fig. 3.10b it is evident that for samples with $w \approx 60$ µm, the heat transfer coefficient increases as pore size p decreases from 28 µm to 8.5 µm because in this manner the number of pins and thus available area for evaporation of thin liquid film near the contact line is increased. In samples

with $w \approx 30$ µm, there is an increase in heat transfer coefficient as pore size p is decreased from 16.5 µm to 9.2 µm. For $p = 9.2$ µm, the heat transfer coefficient reaches a maximum of 20.7 (± 2.4) W/cm^2-K at a dryout heat flux of 119.6 (± 4.2) W/cm^2. For large (~1cm^2) heaters, this represents both the highest heat flux and the highest heat transfer coefficient reported in literature for the predominantly evaporative heat transfer attesting to the benefits of using biporous wick structures. The heat transfer coefficient drops significantly for the smallest pore size of $p = 4.9$ µm which might entail a different physical explanation deviant from expectation as detailed below.

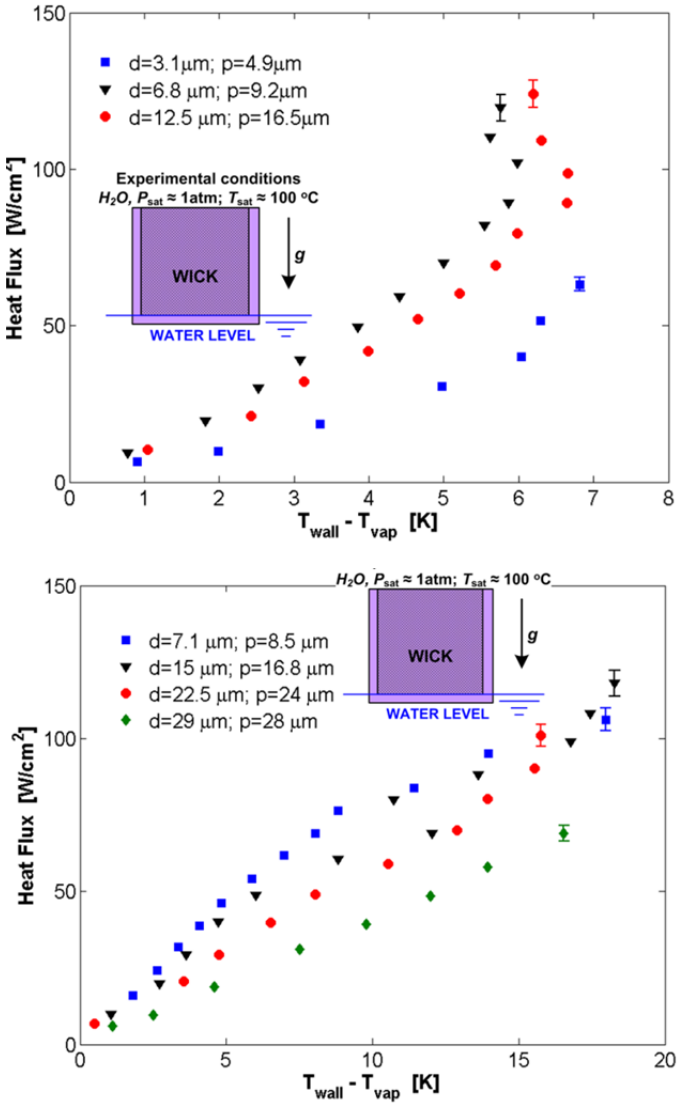

Figure 3.10 (top) Heat transfer data for various pin fin and pore size with channel size $w = 30$ µm, nominal array width $D = 150$ µm and nominal wick depth $H = 145$ µm; (bottom) Heat transfer data for varied pin fin size with channel size $w = 60$ µm, nominal array width $D = 260$ µm, and nominal depth $H = 150$ µm. Only error bars at dryout heat fluxes are shown for each data set. The inset image shows experiment conditions and wick orientation for both plots (vertical).

For a scaling analysis valid to leading order, we neglect spatial variations in curvature, all convective effects, and approximate the region of dominant thermal resistance as a thin liquid film of height L_{film} and average thickness δ near the top of each pin (Fig. 3.11). The dominance

of conduction over convection in the pores of the wick is verified by considering the Peclet number vd/α. Here v is the velocity of liquid required to maintain a fixed liquid/vapor interface undergoing evaporation, d is the characteristic length scale which in this case is the pin size, and α is the liquid thermal diffusivity. The velocity is calculated by Eq. (3.3)

$$v = \frac{q}{\rho_l h_{fg}} \tag{3.3}.$$

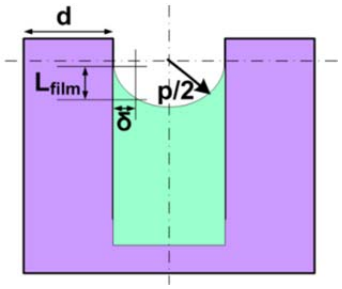

Fig. 3.11 Sketch of a thin liquid film and meniscus around a micro pin fin. Here L_{film} is the liquid film length along the pin that forms at the meniscus, p is the pore size spanning the pins, d is the side length of a square cross section pin, and δ is the thickness of the thin liquid film.

For the highest levels of heat flux considered of approximately q = 200 W/cm^2, this velocity scale is on the order of $v \approx 1$ mm/s which yields Peclet numbers that range from 1.7x10^{-2} for the smallest pin size tested d = 3.1 μm to 1.59x10^{-1} for d = 29 μm. This implies that even at such high heat fluxes, conduction heat transfer is still the dominant mode by at least one order of magnitude.

In the wick structures considered here composed of pin fins with square cross section and side length d and pin spacing p, the length L_{film} of the thin liquid film near the contact line is truncated by the assumed constraint that the meniscus takes on a spherical shape away from the solid surface and perfectly wets the solid surface (Fig. 3.11). The number of pins N protruding out of an area A is $N = (1-\phi)A/d^2$. Thus, the conductance (W/cm^2-K) of the liquid film is

$$g_{film} = \frac{(1-\phi)}{d^2}\frac{k_l(4d)L_{film}}{\delta}, \tag{3.4}$$

where $(4d)L_{film}$ is the surface area of the thin liquid film surrounding the pin of size d. Considering a two-dimensional situation (Fig. 3.11), the scales L_{film} and δ are related through the relation

$$L_{film} \approx \sqrt{(p/2)^2 - (p/2-\delta)^2} \tag{3.5}$$

Under this assumption, the conductance can be determined in terms of all measurable quantities with the film thickness δ being the only fitting parameter.

$$g_{film} = \frac{4k_l(1-\phi)}{d}\sqrt{\frac{p}{\delta}-1} \tag{3.6}$$

We observe that at low to moderate heat fluxes, the slopes of the heat transfer curve are nearly independent of applied heat flux for all pore sizes. This indicates that when the liquid

level in the wick is high, the base of the wick structure is not activated, and the assumptions used in deriving Eq. (3.6) are satisfied. For comparison of the observed film conductance with the predictions of Eq. (3.6), we extract heat transfer coefficients from Fig. 3.10(top) for various pore sizes at a moderate heat flux of ~60 W/cm^2 where evaporation is the dominant mode of heat transfer. A 1-D conduction model is used to extract the film conductance. This analysis assumes assumes a heat transfer area of 1cm^2 at the base of the pins, which translates into varied thin film area as p and d are varied as indicated by $(4d)L_{film}$ term in Eq. (3.4). A potentially larger area for evaporation due to thermal spreading is captured in the uncertainty and will not affect the trend with p significantly. Equation (3.6) is plotted in Fig. 3.12 as a solid line for a film thickness $\delta = 4$ µm. The data for samples with channels $w \approx 60$ µm appear to follow the $\sqrt{p/\delta - 1}$ trend predicted by Eq. (3.6). A similar trend can be discerned for the samples with channels $w \approx 30$ µm (dashed line in Fig. 3.12, $\delta = 4$ µm), for which the values of conductance are higher for the 9.2 µm and 16.5 µm pores. The higher values of conductance for the samples with 30 µm channels are attributed to a greater wicking area around the heater of 4.2 cm^2 compared to a value of 3.8 cm^2 for those with 60 µm channels which is a consequence of the fabrication. This reduces the number of pins by roughly 10 % when the larger channels are used. The only anomaly to the trend is the film conductance for the sample with $p = 4.9$µm pores and $w = 30$ µm channel. Here the conductance dips sharply below the estimated trend. We attribute this to the suppression of evaporation caused by interface curvature and reduced liquid pressure. Additionally, this hypothesis is also supported by data shown in Table A1.1of the appendix which also summarizes the total pin fin area. Although the smallest pins yield largest surface area the overall conductance is still reduced.

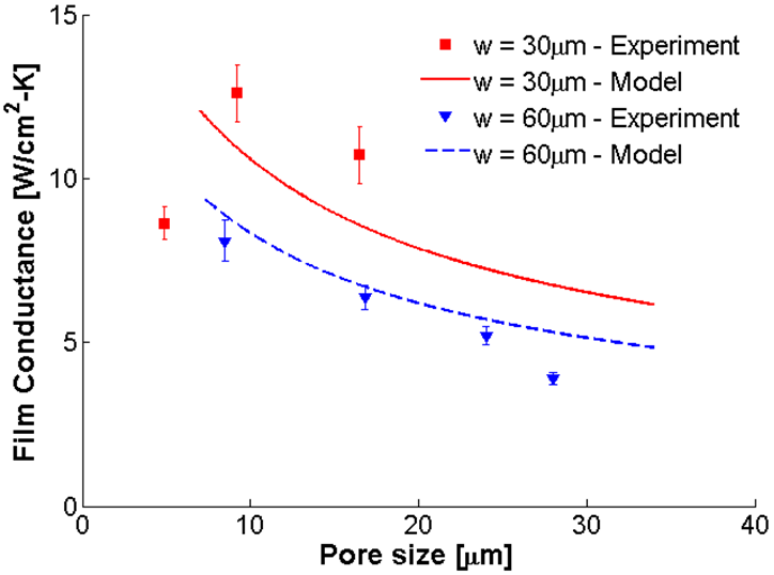

Fig. 3.12 Variation of the thermal conductance of the thin liquid film as a function of pore size at low evaporative heat fluxes of ~60W/cm^2.

To better interpret these results, we let T_l be the temperature of bulk liquid, while the curved liquid-vapor phase interface is at T_{lv}. For the two dimensional geometry considered here, the superheat required for phase equilibrium is given by combining the Kelvin and Clapeyron effects to yield:

$$T_{lv} = T_{sat}(P_l)\left[1 + \frac{\sigma}{(p/2)\rho_v h_{fg}}\right] \quad (3.7)$$

As pore size p is reduced from 16.5 down to 4.9 μm, Eq. (3.7) predicts the required superheat to be of the order of 1-6 K respectively. In a situation far from equilibrium with high interfacial mass fluxes, the required superheat may be considerably larger. Consequently, as pin size d and pore size p decrease in order to increase the surface area for evaporation, a larger fraction of the heat flux from the pin fin is used to superheat the liquid flowing towards the meniscus, resulting in low observed overall heat transfer coefficient for p = 4.9 μm. Numerical calculations by Ranjan et al indicate that increases in superheat of even 2–4 K can reduce interfacial evaporation coefficients by as much as an order of magnitude.[125]

3.4 Summary

Experimental data are presented for evaporation from a biporous medium consisting of pin fin arrays periodically separated by larger microchannels. Heat fluxes of up to 119.6 (± 4.2) W/cm^2 can be dissipated in predominantly evaporation heat transfer. For larger pores and deeper wicks (p > 16 μm and H > 145 μm respectively), a nucleate boiling regime is observed with high dryout heat fluxes up to 277.0 (± 9.7) W/cm^2 for large heaters (~1cm^2), and high heat transfer coefficients up to 19.6 (± 0.8) W/cm^2-K. A stable regime of boiling is observed for up to 185 W/cm^2 beyond the heat flux of boiling incipience in these samples. For small heaters of area 0.0625 cm^2, high heat fluxes of up to 733.1 (± 103.4) W/cm^2 can be dissipated, making these wick structures attractive for hotspot thermal management. The overall heat transfer coefficient is increased with a reduction in pore size and accompanying increase in surface area. A simple model is proposed that captures the trends in the observed data.

The preceding chapter first appeared in *ASME J. Heat Transfer, Vol. 134, Issue 10, 101501, (2012)*

Title: Enhanced Heat Transfer in Biporous Wicks in the Thin Liquid Film Evaporation and Boiling Regimes

Authors: Dusan Coso,* Vinod Srinivasan,* Ming-Chang Lu,* Je-Young Chang, Arun Majumdar

*denotes equal contribution

4. Hybrid Micro/Nano Structured Surfaces for Enhanced Phase Change Heat Transfer

In this chapter, hybrid structures made of microscale cavities and combined with nanowires are used to enhance of phase change heat transfer for pool boiling applications. In addition, structures similar to those in Chapter 3 are studied here in pool boiling experiments in attempts to distinguish between what physical phenomena govern CHF in thin liquid film phase change, and pool boiling systems. To avoid redundancy, some images of the micro pin fin arrays and the definition of their parameters is not repeated here and instead can be found in Chapter 3.2.1.

4.1 Background, Motivation and Survey of Previous Work

As it was discussed in the introductory chapter, and supported by several theoretical models in the latter portion of Chapter 2, there are still disagreements in the scientific community as to what exactly causes the onset of CHF in pool boiling systems. On large, well wetting surfaces, where the characteristic length scale is large compared to the capillary length L_c far field hydrodynamic theory presented in Chapter 2.2.4 seems to predict the CHF mechanism reasonably well.[60,61,64] Experiments conducted by Theofanous et al on large fresh and aged surfaces suggest that in those systems CHF is governed by hydrodynamic bubble interaction in a microlayer very near the surface where viscous flow, capillarity, wettability and other surface phenomena play important roles in surface rewetting and preventing growth of dry spots that trigger CHF; their studies indicate that CHF increases with increasing nucleation density.[65,66]

For 'finite' size heaters which will be used repeatedly throughout the chapter to indicate a length scale smaller than ~ 3 times the critical Taylor wavelength $\lambda_{T,c}$ Eq. (2.29b), [126] edge effects and these local surface conditions are even more pronounced, and it is anticipated that for wetting systems, the measured CHF will exceed that of an infinite surface with the same surface condition.[118,121,126] Haramura and Kato proposed an inflow factor $k = 0.83$ that captures this enhancement for finite 1 cm diameter copper discs and attributed it to the rewetting from the heater edges promoted by pressure gradients between the vapor pressure near the center of the finite heater and the surrounding liquid pressure caused by buoyant force effects. However, this trend has only been captured empirically, and through visual studies of other researchers.[118,127] Enhancement in CHF is also caused by inflow of liquid from heater edges driven by capillarity. For nanowire surfaces of finite size, Lu et al have argued that the Helmholtz wavelength for small heaters where only a single vapor column exists becomes limited by the heater size, and in their analysis they conclude that the enhancement is due to higher bubble nucleation density on nanowire surfaces yielding a larger vapor column to heater area ratio.[79]. In some studies enhancement in CHF is attributed to increased wettability,[78,128] while increased bubble nucleation seem to deteriorate CHF performance.[64,68,129] In view of these differences it is likely that all these effects have some share of responsibility for the onset of CHF, and it would be beneficial to study systems where these phenomena can be separated or more easily distinguished.

Along with increasing the maximum heat flux that can be dissipated from a surface, enhancing the heat transfer coefficient is also crucial, particularly in immersion cooling applications.[9,130,131] A relatively recent program initiated by DARPA for cooling of integrated electronics, particularly within hundreds of microns of electronic junctions, might

suggest that immersion cooling systems may still be crucial in achieving higher thermal management performance if engineered properly.[132] For operation of microelectronic systems, high CHF gives a higher factor of safety, and allows for operation at more severe conditions. However, another characteristic of heat transfer performance, the HTC, need also be high to yield lower temperature of operation and thus allow for more efficient performance of microelectronic components. At lower operational temperature, these microprocessors can have less leakage caused by electrothermal coupling between dies.[131,133,134].

A typical approach to enhancing HTC is by microstructuring or generating cavities on a surface which promote heterogeneous nucleation. It is pretty well known that cavities capable of trapping vapor are very effective at promoting bubble nucleation and thus enhancing heat transfer coefficient.[67,135] In addition, some have also argued that increased bubble density can act to enhance CHF.[65,66,79] Conical cavities or surface dents and scratches can be sources for bubble nucleation, but are intermittent and unstable in well wetted systems.[17,136] This is mostly attributed to their geometry and the likelihood of being rewetted during the bubble ebullition cycle. Several researches have investigated other engineered cavity shapes in hopes to promote nucleation, initiate it at low superheats, and make it stable until CHF is reached. Reentrant cavities have received much attention over the last several decades because they can trap vapor very effectively due to the interface shape that forms within the cavity (see Fig. 2.9 and Eq. (2.22)). Thus, the benefit of implementing reentrant cavities may not be to solely promote HTC (regular cavities may also be able to do this), but also keep the cavities steadily active over a broad range of heat fluxes.

Several researchers have focused on understanding nucleation site interactions, and if at all cavity geometry brings about significant changes to enhancing or deteriorating heat transfer. Goyal et al and Phadke et al implemented pyramidal reentrant cavities on silicon substrates and observed a significant reduction of superheat required for bubble nucleation onset versus plain (cavity free) surfaces.[137,138] Bhavnani and Jaeger showed that pyramidal reentrant cavities are better at reducing temperature overshoot than reentrant cavities with a rounded bulb base.[139] A systematic study of bubble nucleation characteristics from conical, cylindrical and reentrant cavities done by Shoji and Takagi indicated that conical cavities were rather intermittent while the other two geometries displayed stable and continuous bubbling at various heating rates and low superheats.[136] Chatpun et al determined that the cavity interactions (thermal, hydrodynamic) are significant when cavities separated by distance S satisfy the condition $S/L_c \leq 3$ where L_c is the capillary length scale.[140] They also argued that the complexity of interaction increases with the number of cavities.

In this investigation the objective is twofold. Firstly, the intent of this investigation is to isolate phenomena responsible for the onset of CHF in surface engineered capillary systems of finite size. To achieve this, micropillar structures identical to those presented in Chapter 3 are used in pool boiling experiments and compared to the heat transfer data obtained in thin liquid film wick structure experiments. Results presented in Chapter 3 indicate that in samples where thin liquid film boiling is detected, CHF increases with wick depth. Here two pore sizes of different depths of identical geometries will be explored in visualization studies, and for CHF comparisons. The intent here is to determine if the presence of a vast liquid pool above the surface brings about far field hydrodynamic effects that limit CHF, or if the onset of CHF is more complicated and has to be attributed to a combination of different phenomena. Finite heater

sizes are of particular interest because they can be implemented for thermal management via immersion cooling of compact microelectronic systems.

Secondly, the intent is to use hybrid micro-nano structure engineered surfaces that enhance HTC. These structures are composed of cavities (bulb-reentrant or rectangular) beneath the surface, and nanowires etched at the top surface above the cavities that promote wetting and capillarity. This part of the project is a continuation of the work done previously in our lab.[78,79] This design is motivated on the premises that combining surfaces with good wetting/capillarity and increased nucleation site density characteristics can yield high heat transfer performance in immersion cooling/pool boiling systems, and increased CHF as argued in other works.[65,66,79] For instance, in the work of Lu et al, high HTC of ~ 4.7 W/cm^2-K are reached near CHF of ~ 150 W/cm^2 at a superheat of ~35 K in boiling experiments of deionized water on 1 cm^2 silicon nanowire surfaces. If encountered in real applications of immersion cooling of microelectronics, such high superheats could deteriorate processor performance significantly.[133,134]

Most findings discussed in this chapter will hopefully soon be part of a journal article publication.

4.2 Materials and Methods

In this section, the geometries studied in pool boiling experiments are presented. Also the detailed fabrication and experimental procedure which proves to be effective at minimizing heat losses is presented. In this study silicon is used as the material for surface engineering. This is primarily because silicon possesses good thermal properties, it is easy to process into desired structures via micro/nano fabrication techniques, and can be more easily integrated in microelectronic systems. Filtered clean room grade deionized water is used for all experiments.

4.2.1 Parameter Range

Biporous pin array structures similar to those used in thin liquid film experiments shown in Fig 3.2(top) (also see Chapter 3.2) are used in pool boiling experiments here. Here only two geometries are implemented where the average pin and pore size combinations d/p are summarized later in Table 4.2. Additionally, depths ranging from $H \approx 3.8$ μm to $H \approx 179$ μm microns are used here, and the microchannels in the biporous array are kept at $w = 30$ μm to preserve the same porosity of $\phi \approx 0.79 \pm 0.04$. The choice of these dimensions is predicated by the experiments already done and presented in Chapter 3. In addition, the detailed fabrication of these structures was presented in Chapter 3.2, and only slight modifications are implemented here.

The parameter range of micro/nano hybrid structured surfaces investigated is shown in Table 4.1 These surfaces incorporated microscale cavities periodically distributed in a 2-D square lattice below a nanowire covered silicon surface. Spacing between the closest cavity edges were 100, 200 and 800 μm (See Fig. 4.1, center to center cavity pitch is defined as $p_c = s_c + d_c$). Cavity depth effects on performance were not considered, but in most experiments the D_c/d_c aspect ratio was maintained to be greater than 2. Most cavities had a base at a depth D_c defined in Fig. 4.1 that ranged from 45 to 90 μm. D_c is defined from the top of the nanowire array to the bottom of the cavity. The effect of D_c on HTC was not investigated. Table 4.1 also summarizes data for 1 cm^2 nanowire surface investigated by Lu et al that will be used for comparison.[79]

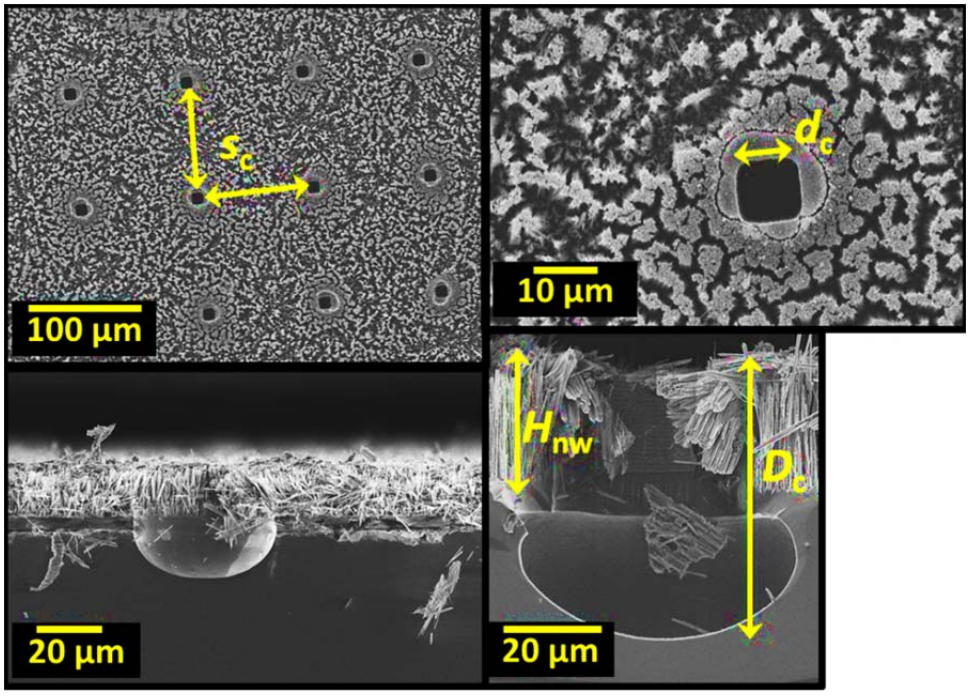

Fig. 4.1 Nanowire surfaces with square array cavities center to center distance $s_c + d_c$ apart (top left) of mouth opening d_c (top right); plain rectangular cavity profile vs. cavity of same size d_c with reentrant bulb base (bottom images). Cavity depth D_c is defined from the top of the nanowires to the cavity bottom. NOTE: nanowires are aligned and vertical during experiments, but get fractured when samples are broken to inspect cavities (See Appendix A1.3 for additional images).

Table 4.1 Dimensional parameters characterizing hybrid micro/nano structured surfaces employed in pool boiling experiments. These sizes are representative of all sample used, and typical variation according to SEM images ranged from ± 5 % except where specified with an error bar. Data from ref. [79] is included for comparison.

Sample type	**Cavity size d_c [µm]**	**Cavity spacing s_c [µm]**	**Nanowire height H_{nw} [µm]**	**Cavity depth range D_c [µm]**	**Cavity density[2] [cm^{-2}]**	**Contact angle [deg]**
Cavity	41	100, 800	34.8 ± 4.4	55 – 90	4900, 144	$\theta < 10$
Cavity	11	100, 200, 800	34.8 ± 4.4	45 – 55	8100, 2209, 144	$\theta < 10$
Plain Si	N/A	N/A	N/A	N/A	N/A	65.0 ± 4.3
NW only	N/A	N/A	34.8 ± 4.4	N/A	N/A	$\theta < 10$
Plain Si [ref. 79]	N/A	N/A	N/A	N/A	N/A	40
NW [ref. 79]	N/A	N/A	32	N/A	N/A	0

The chosen parameter range for cavities of square cross section and cavity mouth dimension $d_c \times d_c$, their shape, spacing s_c, and depth of nanowire array H_{nw} of hybrid micro/nano structures is based on several factors. Firstly, the range of cavity sizes was selected by the notion

[2] Note that the variation in density among samples is due to the choice to have cavity spacing s_c be the distance from cavity edges rather than the pitch which is defined as $s_c + d_c$. Although $d_c = 41$ µm has a smaller density than $d_c = 11$ µm when $s_c = 100$ µm, 11 µm cavities of smaller density ($s_c = 200$ µm) still yield better performance than larger 41 µm cavities of comparable density as will be presented later.

that larger cavities nucleate at much lower superheats as suggested by Eq. (4.1). The smallest cavity mouth size d_c was selected because it yielded a ~2.5 K superheat ($T_{wall} - T_{sat}$) required for onset of nucleate boiling according to Eq. (4.1) which is considered a reasonable temperature for real applications,

$$T_{wall} - T_{sat} = \frac{2\sigma T_{sat}}{r_c \rho_v h_{lv}} \quad (4.1).$$

Once nucleate boiling is initiated, the objective is to maintain stable boiling until CHF is reached with intent to maximize HTC. Thus, reentrant cavities and/or high D_c/d_c aspect ratio cavities were implemented in order to circumvent bubble nucleation suppression characteristic for very well wetting systems.[67,68] Good wetting characteristics in these nanowire surfaces are indicated by rapid complete wetting of the nanowire array with no liquid protruding when drops of DI water are placed on the surface. Due to the nature of sample preparation that will be discussed in the following section, some nanowire surfaces exhibited very poor wetting characteristics, where some liquid was suspended on top of the array (analogous to Cassie-Baxter state),[111] yielding apparent contact angles nearing, or beyond 90°. These samples repeatedly demonstrated lower CHF. Ultimately, only surfaces with well wetting characteristics are of interest in this investigation. The variation in contact angle is attributed to the presence of cavities and some aging of the surface during the last preparation step (some adsorption of particles from surrounding air may occur). Cavity spacing is also chosen such that it satisfies the condition $s_c/L_c \leq 3$ (where L_c is the capillary length scale) so that the efficiency of bubble generation in cavities of different size can be determined in this region where nucleation site interaction is quite complex.[140,141] The primary focus of the study is to determine if presence of cavities further enhances performance of surfaces with silicon nanowires.[78,79] Smooth surfaces and nanowire surfaces with no cavities were employed as control experiments.

4.2.2 Sample Fabrication and Preparation

Figure 4.2 (left) illustrates a sequence of steps of the fabrication of hybrid micro/nano samples for pool boiling experiments. Initially, a wet oxide is grown in a furnace at 1000 °C on a 100 mm diameter wafer (Fig. 4.2-S1). The oxide thickness is generally kept between 1.5 μm and 2 μm. The wafer is coated with photoresist, and after exposure to UV-light in a Karl Suss MA6 Mask Aligner (Fig. 4.2-S2) cavity patterns are generated. The resist is hard baked and the wafer bonded to a 150 mm silicon handle wafer for further processing via a Nitto Denko 31950E acrylic adhesive tape. Exposed oxide is then etched away in a STS-Oxide inductively coupled plasma etching system with C_4F_8. The etching is directional, and vertical trenches are made to expose the silicon for further etching (Fig. 4.2-S3). Deep silicon trenches are then etched in the wafer using inductively-coupled SF_6 plasma in a similar STS system to a desired depth (Fig. 4.2-S4). The wafer is then detached from the handle by heating on a hotplate at 190 °C, stripped in FujiFilm PRS3000 resist stripper at 80 °C, and subsequently cleaned with piranha (H_2SO_4-H_2O_2, 4:1, @ 120 °C) and filtered deionized (DI) water. Another 300 – 400 nm layer of oxide is grown in a wet oxide furnace (Fig. 4.2-S5). This oxide layer is used to protect the cavity side walls for further cavity etching processes. The wafer is again bonded to a handle wafer for oxide removal at the base of the cavities. The old oxide layer is used as the etching mask, and the difference in the initial oxide layer present (~ 1.5 – 2 μm) and the new added layer (300 – 400 nm) is used to ensure all the oxide at the base is etched away (Fig. 4.2-S6). Since high aspect ratios of cavity

depth/size (up to ~10:1, D_c/d_c), and small cavity mouth sizes (up to 41 μm) are implemented, the only way to check if the desired cavity profile is obtained is post-processing, via SEM imaging of the side profile of a sample broken along the cavity containing plane. To make bulb-reentrant cavities, the oxide etching is done until a 200 nm oxide film remains on the top surface. Once detached from the handle, the wafer is placed in a xenon difluoride (XeF_2) gas etching system so that the silicon at the base of the oxide protected cavities can be etched isotropically (Fig. 4.2-S7 and Fig. 4.1). At this point, the wafer is cleaned with piranha and DI water again, and prepared for deposition of an Indium Tin Oxide (ITO) film on the back side that will later serve as a heater. The top surface of the wafer is covered by a dummy wafer and is placed inside an Edwards Auto 306 sputtering chamber for ITO deposition of a ~ 200 nm – 300 nm thick film (Fig. 4.2-S7).

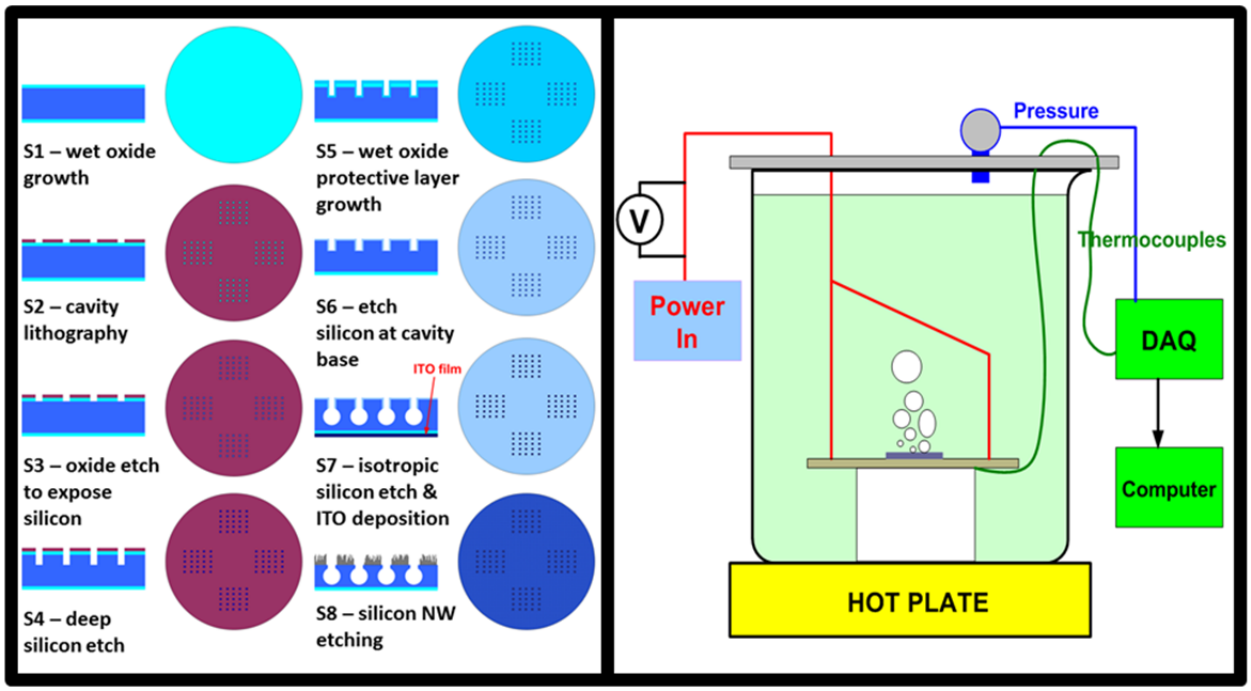

Fig. 4.2 (left) Steps for the sample fabrication for pool boiling experiments. Stopping the procedure at certain steps yields several different types of samples to be tested (e.g. plain surface, nanowire surface with cavities, nanowires only, etc.); (right) experimental setup for pool boiling experiments.

Once the ITO film is deposited, samples are either diced to size with a Disco DAD3240 dicing saw, or prepared for nanowire etching. The nanowires are etched electrolessly using an adapted technique developed by Peng et al.[142,143] First, a chemically resistant UV tape (GTUV224) from STM Semiconductors Tapes is used to protect the back (ITO side) of the samples prior to etching. For etching, 1.50 ± 0.10 g of 99.995% silver nitrate ($AgNO_3$) from Alfa Aesar is dissolved in 200 ml of clean room grade DI water. 50 ml of 49% hydrofluoric acid (HF) is then added to the solution and mixed well by stirring for at least one minute. The solution is poured in a Teflon dish inside a fume hood and a wafer is placed inside, tape protected side facing down. During the etching process, the Ag^+ ions oxidize the silicon and precipitate Ag dendrites. The dendrite distribution shapes the nanowire array profile. The HF acid then etches the oxide layer and this process recurs cyclically and directionally into the wafer surface for a desired amount of time. The resulting array is composed of vertically aligned silicon nanowires with diameter ranging from roughly 20 nm to 300 nm. Once completed, the solution is aspirated,

and the wafer is washed several times with DI water. Nitric acid (HNO_3) is then used several times to dissolve and remove the remaining silver particles. The wafer is washed thoroughly with DI water and dried with nitrogen gas. The protected back side is exposed to UV-light for ~5 min which is sufficient to release the tape. The ITO film remains intact for etches up to 4 hours. Beyond this, the preservation of ITO depends on how well the UV-tape is bonded to it. Typical etch rates depend strongly on lab environment conditions and range from 6 μm to 15 μm per hour for this given recipe and etches up to 4 hours. The cavity/nanowire hybrid structures (Fig. 4.2-S8) are then coated with photoresist used as a protective layer for dicing the wafer to desired chip size. Stopping at various steps of this fabrication procedure can yield several types of samples including: flat silicon surface, oxidized flat silicon surface, flat surface with regular or reentrant cavities, plain nanowire surface, and nanowire surface with regular or reentrant cavities.

Once cut to size (1×1 cm^2 samples are used in this investigation) the samples are sequentially cleaned with acetone, isopropyl alcohol, and DI water several times to remove any residual photoresist. Cleaned chips are dried with nitrogen gas. A 75×50 mm^2 glass slide with a centrally drilled 7 mm diameter hole is cleaned in similar fashion (Fig. 4.3a). A 15×75 mm^2 ~ 60 μm thick copper tape is placed symmetrically along the slide to cover the hole and is cut in such a way to open an 8.5mm slot for chip placement as illustrated in Fig. (4.3b). SPI Conductive Silver Paste Plus (~ 72% Ag solids) is used to bond the chip to the copper tape leads and ensure good electrical contact.[3] A very thin bead of paste is used on each edge of the two copper electrodes, and the chip with the ITO side down is placed symmetrically over the hole and with chip edges overlapping those of the copper tape (Fig. 4.3c). Once bonded to the copper, each sample is baked on a hot plate at 110 ^oC for 1-2 hours so that the silver paste can cure. Several samples have been tested to measure the total electrical resistance of all leads connected (including copper wire, copper tape and silver paste joints – see inset of Fig. 4.3). Typically, the overall resistance ranges between 0.10 and 0.25 Ω per lead. This is a very small fraction of the ITO heater resistance which ranges from ~20 – 30 Ω for all samples (See also Appendix A1.2). Hence a very small fraction of the power supplied is dissipated by joule heating in the leads and this is determined uniquely for each sample tested. Kapton tape is then used to insulate around the chip in order to prevent water from directly touching the edges, and also insulate the top of the copper leads. Small windows on each of the copper leads as seen in Fig. 4.3c are left for attaching electrical wires to the sample. Prior to this wire bonding, each sample is cleaned with oxygen plasma for 3 min at 200 W. This is to ensure photoresist, and any other remaining organic residue is completely removed. Once the samples have been cleaned, insulated copper wires are secured to the sample with carbon tape and bonded with silver paste until it cures. When cooled to room temperature, 100% silicone is used to completely seal and insulate the wire junctions. Two small 25×25 mm^2 glass cleaned glass slides are used to press down the silicone and form the seal. At this point, all the copper components are completely isolated from the environment.

[3] Prior to silver paste bonding, a dummy sample from the same ITO deposited batch is tested under a pressure of at least 1MPa against the copper pads. The measured electrical resistance of the sample under these conditions compared to the samples bonded via silver paste were within < 0.5%.

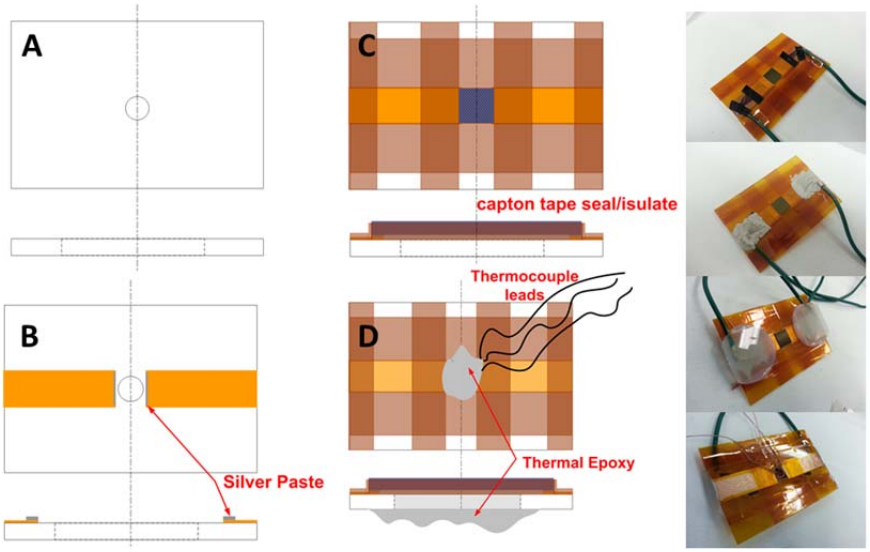

Fig. 4.3 (a) Glass slide with centrally drilled ~7 mm hole; (b) Placement of the copper tape and silver paste in preparation for chip bonding; (c) Bonded chip, additionally insulated with kapton tape on edges, and remaining parts of the glass slide; copper windows opened for further electrode bonding (orange patches); (d) Thermocouple bonding on the back of the sample via thermal epoxy. NOTE: these are not to scale and (a-c) are top views of the prepared samples while (d) is the view from the bottom; at the base of each image is the profile view of the region near the drilled hole (zoomed in). The inset shows a series of pictures of an actual sample in preparation.

When electrical wiring is completed, three special limit of error (SLE) Omega Engineering T-type thermocouples are placed centrally along the heater ~ 2mm apart as indicated in Fig. 4.4. The thermocouples are then bonded to the heater using electrically insulating epoxy (EPO-TEK T905BN-3, $k_{epoxy} \approx 2.02$ W/m-K), which also serves to fill all air gaps between the sample and the glass slide. Once cured at 100 ^{o}C for 1 hour and cooled to room temperature, a Teflon block with a drilled 20 mm diameter and depth hole at the center is bonded to the back side of the sample concentrically (hole to sample) with 100% silicone adhesive beaded around the hole. This is done to seal the back side of the sample from water and insulate it for heat losses. The silicone cures overnight, and each sample is thoroughly cleaned with DI water and dried with nitrogen gas prior to every experiment. After each experiment, the block is immediately detached to ensure no water has penetrated onto the sample back side. Any sample where water is observed is considered compromised, and this data is not included due to the possibility that phase change heat transfer occurred on the back side and generated high heat losses that could not be accounted for. Due to long curing time of 100% silicone, experiments were typically performed after 12 to 24 hours of complete sample preparation. This nature of prep may be responsible for yielding poorer wetting characteristics on some samples.

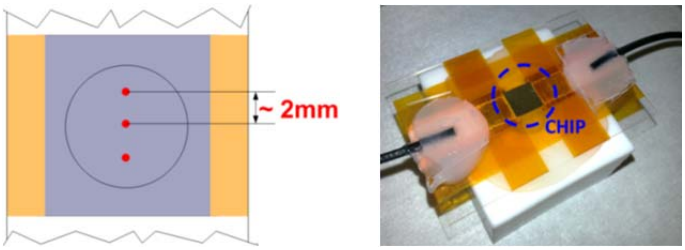

Fig. 4.4 Illustration of the thermocouple placement (red dots) on the back of each chip tested, and a picture of a sample ready for testing where the chip is circled with the dashed blue line.

4.2.3 Experimental Setup

Once each sample is prepared as shown in Fig. 4.4, it is washed with filtered DI water several times and placed in a 2 L beaker filled with filtered DI water as illustrated in Fig 4.2 (right). All experiments were performed with the samples surface along the horizontal plane. Thermocouples from the sample and those measuring the liquid pool temperature are connected to an Agilent 34970A data acquisition unit via an Agilent 34902A 16 channel multiplexer which has a built in thermocouple reference junction. The pressure is also measured via a Setra Systems pressure transducer connected to the data acquisition unit. The beaker is covered with a porous aluminum foil layer so that vapor and gas can escape and the system remains open to atmospheric conditions. Electrical leads from the sample are connected to the Agilent N5750A DC Power Supply (150V/5A/750 W). Once the system has degassed for one hour, the experiment is initiated. Typically, power is applied at ~ 2.5 W increments up to 15 – 20 W, and subsequently at increments of ~ (7.5 – 10) W until CHF is reached. Each reading is taken after the system has reached steady state conditions and remained stable for at least 3 min. To properly determine the power supplied to each sample, a Newport TrueRMS Supermeter multimeter is connected in parallel with the electrical leads from the sample to measure the applied voltage (see Appendix A1.2). The current reading is taken from the power supply with the appropriate manufacturer specified uncertainty. Before all heat losses Q_{loss} (joule heating in leads, conduction in substrate, heat loss through back side of sample) are accounted for, supplied power P is determined as the product of the measured voltage V and supplied current I, $P = IV$. Thus, the heat flow through the sample Q is defined as $Q = P - Q_{\text{loss}}$, and HTC is defined as

$$h = HTC = \frac{Q / A_{heater}}{T_{wall} - T_{sat}} \tag{4.2}$$

and based on the projected cross sectional area A_{heater} of the sample, and the sample wall temperature T_{wall} determined from a 1-D conduction model implemented once Q is determined. Contact angles are measured via a Kruss goinometer prior to experiments and the averages are shown in tables 4.1 and 4.2 where applicable. The uncertainty in these measurements and the heat loss calibration is discussed in Appendix A1.2.

4.3 Results and Discussion

4.3.1 CHF Limitations in Thin Liquid Film and Pool Boiling Systems on Biporous Micropillar Array Surfaces

In order to get a better understanding of what mechanisms are crucial in limiting CHF, it is important to consider experiments where known limiting phenomena such as capillarity, wettability and hydrodynamics are isolated as best as possible. This can be achieved by considering a capillary surface with a given finish (e.g. micro or nano porous etc.) and implement it in both, pool boiling experiments where far field hydrodynamic effects can be more easily encountered, and thin liquid film experiments where wettability, capillary, and near the surface hydrodynamic phenomena are more prominent. In this section, structures used in wick evaporation/boiling experiments presented in Chapter 3 are probed in pool boiling experiments.

Visualization Studies: Capillary Wick vs. Pool Boiling Experiments

As discussed in Chapter 3 and shown in Fig. 3.7, for thin liquid film experiments, in wick structures of sufficient depth (H > 150 μm) a regime of stable boiling is encountered at elevated

heat fluxes where bubbles merge and burst simultaneously over a large fraction of the heater area yielding an increase in HTC. Figure 4.5 illustrates a bursting sequence (yellow dashed lines) for a wick of depth $H = 159 \pm 8$ μm and parameters $d = 12.6$ μm and $p = 15.7$ μm. Severity of CHF in thin liquid film wick experiments is shown in Fig. A1.8 of Appendix A1.3 for a pin array structure of same porosity but slightly different geometry[4] than investigated here. Because the wick is surrounded by a vapor environment, the generated bubbles cannot grow much beyond the surface and are released at high frequencies allowing for rapid liquid resupply to the depleted region and short ebullition cycles. Similar qualitative observations were noted for isolated nucleate boiling in sintered copper mesh structures by Li and Peterson, who claimed that thinner wicks (< 1mm) limited bubble size at collapse, increased bubble generation frequencies, and reduced liquid/vapor counter-flow resistance within a multi-layer mesh porous media which in turn yielded increases in CHF and HTC simultaneously.[53] Based on visual observations it is clear that this regime of nucleate boiling does not prevent rewetting and cause the wick to fail. Instead, it actually may act to prevent formation of local dry spots as observed in shallower wicks where no clear boiling is observed (see Chapter 3.3.1). The wick dries out when the capillary limit is reached, which is indicated by the sudden and complete radial liquid recession over the heater area and ultimately burnout (see Fig. A1.8).

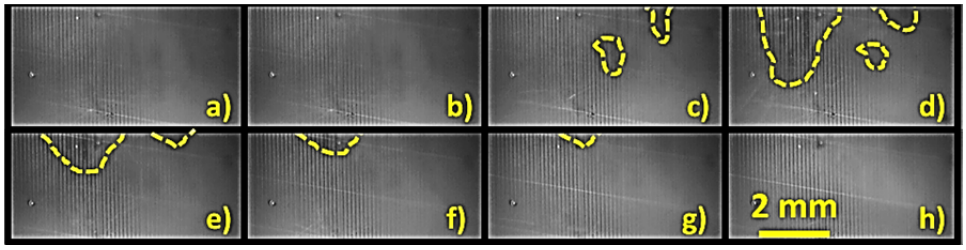

Fig. 4.5 Capillary wick experiment: a sequence (a-h) of a bursting cycle at $q \approx 154$ W/cm^2 that starts from a fully wetted wick (a), produces a large liquid depleted spot formed by the bursting (yellow dashed lines c-f), and gets rewetted by capillary pressure (g, h) to sustain this process. Each frame is taken at 4 ms intervals giving a total length of this bursting cycle (b-e) of ~ 12 ms. The parameters of this wick are $H \approx 159$ μm, $d = 12.6$ μm, $p = 15.7$ μm, $w \approx 30$ μm.

Parameters of biporous micropillar surfaces used in pool boiling experiments are summarized in Table. 4.2 (see Table 3.1 and A1.1 for comparison). A sequence of frames obtained via a Fastec Imaging (IN100M2GB) CCD camera at 250 frames per second is shown during a pool boiling experiment in Fig. 4.6 at conditions very near the CHF ($q \sim 145$W/cm^2, $d = 13.1$ μm, $p = 15.7$ μm, $H \approx 147$ μm). Structures used in Fig. 4.5 and Fig. 4.6 are of same geometry and at similar heat flux conditions allowing for qualitative comparison. In Fig. 4.6 initially the surface is covered by a densely packed bubble array which suddenly merges near the surface to form a large expanding secondary bubble (Fig 4.6(a-d)). As the large bubble expands it hovers near the surface appearing attached to it, and tends toward a more spherical shape (dashed yellow lines in Fig 4.6(e-m)). The bubble eventually detaches and flows away due to the buoyant force. At this point the heater is again covered by an array of smaller bubbles and the cycle of merging and ejection is repeated (Fig 4.6(n-p)). In Fig. 4.6(g-k) the heater can be seen through the large vapor cloud implying that once smaller bubbles merge and detach, the surface

[4] This is one of the few samples tested beyond CHF that reached meltdown while all other samples are preserved for the purpose of repeating measurements. Therefore the image sequence is chosen to be placed in the appendix, and is only meant for illustrative purposes.

is rewetted presumably due to the capillary pressure from the heater edges and more significantly by liquid flow induced by the detaching bubble. Similar behavior is observed in other studies of pool boiling on finite surfaces (eg. heater characteristic size $W < 3\lambda_{T,c}$), where near CHF bubbles near the heater surface (macrolayer) merge to form a secondary large escaping bubble.[127]

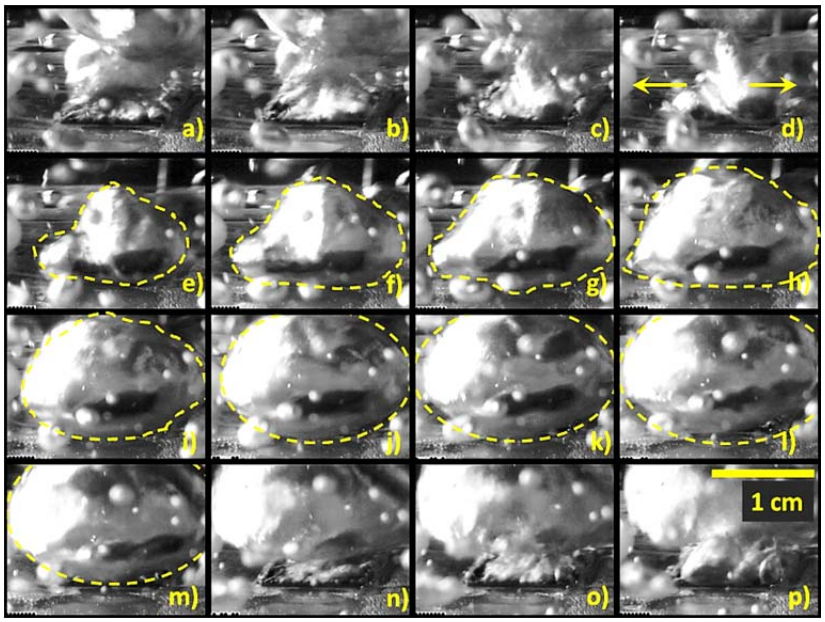

Fig. 4.6 Pool boiling experiment: ebullition cycle (a-o) of bubbles merging in a pin fin array structure of d = 13.1 μm, p = 15.7 μm, and $H \approx 147$ μm toward the heater center to form a large vapor cloud at a heat flux of $q \approx 145$ W/cm^2. Each image is taken at a 4ms span, thus the total length of a large bubble release sequence is ~60ms.

For all geometries tested in pool boiling experiments, very near CHF (within ~10 %) the secondary bubble diameters D_b varied with micropillar depth H as shown in Fig. 4.7. Larger D_b indicated more active phase change heat transfer within the pores of deeper micropillar arrays, but the variation in D_b platoet for $H > 80$μm.

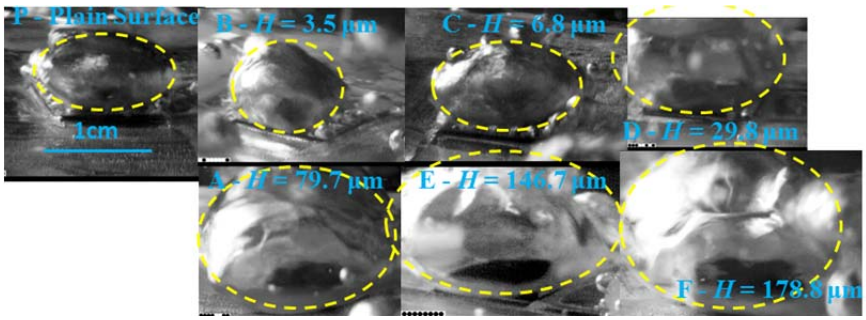

Fig. 4.7 Variation of secondary bubble diameters D_b near CHF for samples of various depth H.

Table 4.2 summarizes the apparent contact angles of DI water measured on all samples tested (see Fig. A1.9 for images). The plain surface yielded apparent contact angles of $\theta_{meas} \approx 65^o$, higher than those observed with DI water on plain Si or SiO_2 surfaces in other studies.[78,79,144] This measured value was repeatable and may be due to some aging of the surface during the long sample preparation discussed in section 4.2.2. This process and the subsequent cleaning procedure was consistent for all samples tested so we anticipate similar surface properties for all samples at the beginning of each experiment. Consequently, the reduction in contact angle from the plain surface sample is solely attributed to the surface area

augmentation via increased micropillar depth. This is confirmed by the good agreement with Wenzel model Eq. (2.2) where the ratio γ is approximated by the total surface area enhancement A_{total}/A_{plain} also shown in Table 4.2. Some discrepancy exists with sample series A and D where a finite contact angle was measured contrary to estimates of Eq. (2.2) which suggests that any $\gamma >$ 2.4 should yield a contact angle of 0^o, but the deviation is not significant.

In contrast to capillary wick structure experiments where CHF increases approximately linearly with H, experimental data indicates that CHF in pool boiling experiments rises proportionally with wick depth H up to a certain value beyond which it plateaus. The CHF experimental data, wetting characteristics, and visualization studies will be considered more closely in the following subsection to distinguish the limitations between the two experimental systems. It is further noted that for the sample in Fig. 4.5, there were approximately 65 independent bursts per second (eg. f_B ~65 Hz.) at 154 W/cm^2. This measured value is limited by the 4ms resolution of the camera, and the actual number may be larger. For the sequence shown in Fig. 4.6, an average ebullition period of 62.5 +/- 16.5 ms (~ 16 Hz.) is observed during the entire length of the recorded video (~4.8 s) measured at this applied heat flux. Bubble release is clearly hindered by the formation of the secondary vapor cloud in pool boiling experiments. In deeper micropillar arrays that appear to be very well wetting, appearance of wave-like nodes at the heater edges, and antinodes at the heater center observed at CHF may indicate hydrodynamic behavior limited by heater size or surface geometry (see Fig. 4.8) as observed in other studies of highly wetting systems.[79,145]

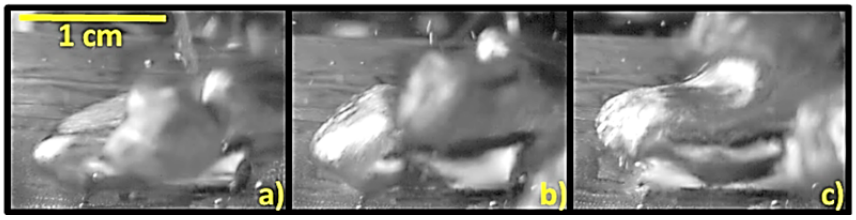

Fig. 4.8 At CHF ($q \approx$ 151 W/cm^2) the isolated bubbles covering the heater as in Fig. 4.6p between large bubble ebullition cycles are replaced by a constant vapor film. These images are shown at 16ms intervals; image (c) shows the appearance of wave-like nodes at heater edges, and anti-nodes at the center at CHF.

Experimental Trends

Figure 4.9 shows data that compares CHF in thin liquid film and pool boiling experiments on biporous micropillar structures of similar porosity (ϕ = 0.79 ±0.04), and parameters d and p as summarized in Tables 3.1 and 4.2, but varied depth H. The horizontal line in the plot represents pool boiling data on smooth samples series P with the error bar being the orange shading based on several measurements. All presented pool boiling data is adjusted for heat losses (see Appendix 1.2) and all CHF error bars shown are at a 90% confidence level. The thin liquid film data is adjusted for heat losses with error bars based on a single measurement since these were fabricated to have a unique wick depth per sample tested. The variation in wick depth for thin liquid film experiments is no more than 5% (error bars not shown) and based on the value specified by the Surface Technology Systems (STS) DRIE etching tool. Pool boiling experiments are done with the sample surface sitting flat in the horizontal direction, while thin liquid film experiments were done with samples in a vertical orientation wicking against gravity (see inset of Fig. 4.9). Some additional parameters and all CHF values are summarized in Table A1.1 and A1.2 of Appendix 1.3.

Table. 4.2 Parameters of the biporous micropillar array structures used for pool boiling experiments. For all biporous structures used in pool boiling experiments the parameter $w \approx 30$ µm (See Fig. 3.2(top)). A_{plain} is a 1cm^2 flat smooth surface.

Sample type	Sample Depth H [µm]	Pin size d [µm]	Pore size p [µm]	$\gamma = A_{total}/A_{plain}$	Contact Angle θ_α-Eq. (2.2) / θ_{meas} [deg]
A	79.7 ± 3.3	13.3 ± 0.6	15.3 ± 0.3	5.93 ± 0.23	0 / 10.0 ± 3.2
B	3.8 ± 0.1	14.3 ± 0.4	14.2 ± 0.2	1.25 ± 0.02	57.5 / 58.1 ± 5.6
C	6.5 ± 0.2	14.3 ± 0.2	14.1 ± 0.3	1.43 ± 0.03	52.7 / 52.8 ± 6.8
D	29.8 ± 0.8	13.7 ± 0.3	14.5 ± 0.3	2.90 ± 0.09	0 / 27.0 ± 5.0
E	146.7 ± 6.8	13.1 ± 0.3	15.7 ± 0.5	9.95 ± 0.41	0 / 0
F	178.8 ± 8.5	12.7 ± 0.3	15.7 ± 0.3	11.58 ± 0.49	0 / 0
P – Plain	N/A	N/A	N/A	N/A	n/a / 65.0 ± 4.3
X	79.7 ± 2.2	7.6 ± 0.2	8.4 ± 0.2	9.74 ± 0.41	0 / 0

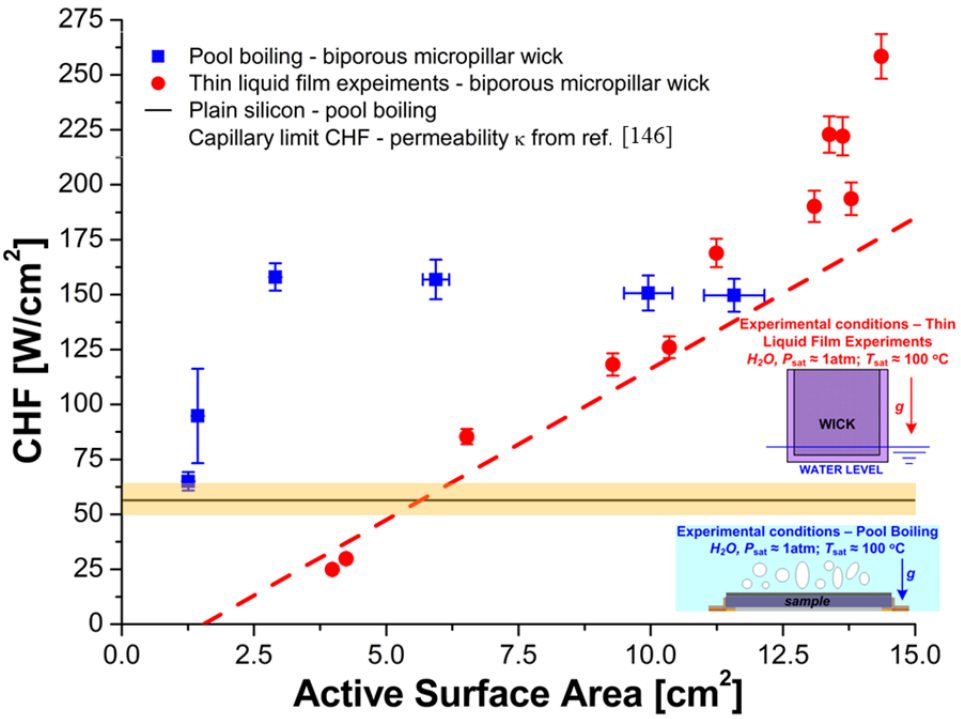

Fig. 4.9 CHF dependence on active surface area for heat transfer in pool boiling experiments (blue squares) to thin liquid film boiling/evaporation experiments (red circles) for biporous micropillar structures of similar parameters p, d, w and varied depth H (See Tables 4.2, 4.3, A1.1 and A1.2); CHF measured for pool boiling on smooth silicon samples (black line) is displayed as a reference with an error bar in CHF (orange shading). For thin liquid film experiments only, a model for the heat flux (red dashed lines) based on capillary limitations indicates good agreement with the data trend.

From the trends in Fig 4.9, CHF behavior in thin liquid film experiments (red circles) is essentially linear with wick depth and thus phase change active surface area since ϕ is kept constant. This area incorporates wick base and micropillar sides, but excludes micropillar tops because they are presumed not to be wetted during experiments (see Table A1.1). At heat fluxes near CHF Reynolds numbers are defined as $\mathrm{Re} = \rho_l v d/\mu_l$ where d is the micropillar characteristic size and v average radial flow speed confirmed visually within the biporous medium (eg. $v \approx 2.5$

cm/s from Fig. 3.5, $v \approx 8$cm/s from Fig. 4.5). The flow speed can also be estimated based on the mass flow rate obtained from heat flux q and projected heater area A (eg. $\dot{m} = qA/h_{lv}$), where the average speed is then defined as $v = \dot{m} / (\rho_l A_{flow})$ and is found to agree well with visually obtained data when the liquid resupply is assumed equal from all sides of the heater thus defining A_{flow} as in Eq. (4.3a). For all samples tested Re < 5 indicating laminar viscous flow and that Darcy's law can be implemented. From Eq. (2.14a) only the liquid pressure drop term and the gravity term are important. The maximum heat that can be maintained by the capillary pressure is then given by Eq. (4.3c).

$$A_{flow} = 4HW\phi_{flow}$$

$$\phi_{flow} \approx p / l$$

$$Q = \left(\frac{2\sigma}{r_p} - \rho_l g L \right) \frac{\rho_l A_{flow} \kappa h_{lv}}{\mu_l L} \qquad \text{(4.3a-c)}$$

In this equation r_p is the effective pores size that provides capillary suction and can be defined based on micropillar spacing p as

$$r_p = \sqrt{(2p^2)} \qquad \text{(4.4).}$$

The effective pore size was used as the fitting parameter, and it was defined as the smallest length scale spanned by 4 neighboring pins – this assumption yielded a good trend with the data. The porosity ϕ_{flow} in Eq. (4.3b) is different than wick porosity ϕ, and is defined as the void fraction of porous area of the wick edges to the total area of the wick edges where the length W is defined by the heater side length; this can be estimated as the ratio of the actual micropillar spacing p to the micropillar pitch l. The average flow length of $L \approx 1.17$ cm was determined as the shortest distance from the water reservoir to the location on the heater where boiling was typically first observed. The permeability κ in Eq. (4.3c) is taken from a numerical study of Sangani and Acrivos for laminar low Re number flow through a square array of cylinders,[146] and is defined as

$$\kappa = l^2 \left(\frac{\ln(c^{-1/2}) - 0.738 + c - 0.887c^2 + 2.038c^3}{4\pi} \right)$$

$$c = \frac{d^2}{l^2} \qquad \text{(4.5a, b).}$$

Experimental data of Xiao et al for flow of DI water through monoporous cylindrical silicon micropillar arrays under the restriction where ratios of the micropillar diameter to pitch, and height to diameter are maintained as $d/l < 0.57$ and $H/d > 1$ respectively,[147] agreed well with Eq. (4.5a). In most micropillar structures investigated here these criteria are satisfied and use of Eq. (4.5a) is thus justified. Because the micropillars used here are of square cross section, this model is used solely for illustrative purposes.

A red dashed line in Fig. 4.9(right) is a plot of heat flux q based on heater area $A = 1\text{cm}^2$ and Q obtained from Eq. (4.3c) and other parameters in Eq. (4.4) and Eq. (4.5). This data is

plotted for a geometry $p = d = 14$ μm, $w = 30$ μm, $\phi = 0.77$ and varied H. Equation 4.2 dependence on total phase change active surface area agrees well with the trend of the measured data. As the cross sectional flow area A_{flow} is increased by increasing H, Eq. (4.3c) indicates a delay of the capillary limit by virtue of liquid pressure drop reduction. The departure of the apparent slope of the measured data and slope of the model indicates the benefit of using biporous wicks and suggests that localized boiling may serve to disrupt liquid profile gradients observed in shallower wicks (see. Chapter 3.3.1) and enhance liquid transport to local hot spots thus delaying CHF. The model trend supports visual claims that the capillary limit is responsible for the onset of CHF. Nucleate boiling and bursting appear to enhance both HTC and CHF in thin liquid film experiments.

For pool boiling experiments the plateauing in Fig. 4.9 indicates a different mechanism of CHF. Below a wick depth of ~ 165 μm (intersection of data in Fig. 4.9), shallower wicks can dissipate much higher CHF in pool boiling as opposed to thin liquid film experiments indicating that rewetting is mainly from the top of the surface. Up to a depth of $H \approx 30$ μm (data series D), CHF enhancement to that of the plain surface seems to be proportional to total wick surface area, however beyond this depth this correlation ceases. In a study of monoporous micropillar silicon surfaces with similar porosities and FC-72 as the working fluid, Honda, Wei, and Takamatsu correlated the CHF enhancement to total surface area enhancement via microstructuring, but as it appears they did not probe large enough H/d aspect ratios to observe the plateau clearly.[75,76]

Recently, Liter and Kaviany proposed that modulated surfaces can be engineered to alter the instabilities suggested by the original work of Zuber.[60,145] These modifications were proposed by introducing periodic microstructures that promote capillary wicking and thus rewetting separated by voids that serve as pathways for effective vapor escape in pool boiling systems.[145] This is essentially a proposition for using biporous and multi-porous surfaces that disrupt near and far field hydrodynamics. For surfaces of finite heater length scales and geometries satisfying the condition $\lambda_m < (9/2\pi)\lambda_{T,c}$, where λ_m is the defining length scale, the CHF is given by Eq. (4.6).[145] For silicon nanowire systems that show excellent wetting characteristics,[79] the modulation appeared to be triggered by heater size.

$$q_{L-K} = \frac{\pi}{8} h_{lv} \left(\frac{\sigma \rho_v}{\lambda_m} \right)^{1/2} \tag{4.6}$$

For well wetting systems, a modified version of the Kandlikar expression Eq. (2.35) was proposed by Chu et al, that captures enhancements observed in CHF in literature due to both apparent contact angle reduction and surface area increase.[144] Their pool boiling data for DI water on microstructured silicon surfaces, and data of several other researchers agreed well with the model, particularly for very well wetting systems.[73,144]. The expression for a horizontal surface is given as:

$$q_{\max,CEW} = K(1+\cos\theta_\alpha)\left[\frac{2(1+\tau)}{\pi(1+\cos\theta_\alpha)} + \frac{\pi}{4}(1+\cos\theta_\alpha) \right]^{1/2} \rho_v^{1/2} h_{lv} \left(\sigma g(\rho_l - \rho_v) \right)^{1/4} \tag{4.7}$$

where K is defined as the constant obtained by Kandlikar to be 1/16, θ_a is the apparent measured contact angle on a given surface; coefficient τ is defined in terms of the apparent receding

contact angle on a smooth surface (eg. series P in this work), and the roughness factor γ given by the surface area enhancement as $\tau = \gamma\cos\theta_a$. The enhancement is attributed to the roughness factor enhanced surface tension force acting at the contact line to delay lateral bubble spreading.

Figure 4.10 shows CHF predicted by Eq. (4.6) and Eq. (4.7) for λ_m defined as the heater size. Findings of Lu et al,[78] and good agreement with predictions of Eq. (4.6) (magenta data in Fig. 4.10 i → k, corresponding to $\lambda_m = W = 0.5$, 1, 1.5, 2 cm respectively) indicating that for well wetting finite surfaces CHF is hydrodynamically limited by instabilities on the order of heater size W in this case. Although smaller than the heater size W, the nanowires are random in structure and thus do not provide even smaller modulations λ_m that would yield CHF enhancement. For well wetted biporous micropillar samples tested here (eg. $A = 1\text{cm}^2$, $W = 1$cm), this identical CHF limit is approached assuming $\lambda_m = W$. Although some modulation exists in these samples (Table. 4.2 and Fig. 3.2(top)) by the presence of larger microchannels, these do not seem to be significant in defining λ_m. Equation (4.7) seems to over-predict the CHF for well wetted samples studied here, while for samples with poor wetting characteristics the trend seems to be captured. For these samples (series B, C, and P) the secondary bubble diameters are smaller than for well wetted samples and less stable. Since these bubbles escape in a single column, the area of influence as proposed by Kandlikar and captured by factor K = 1/16 seems inappropriate. This is adjusted by assuming that the departure diameter used to define Eq. (2.35) is limited by heater size to equal $W/2$. This gives K ≈ 24 when normalize by actual heater size, and yields better agreement with the data for poorly wetting finite microstructured surfaces. Based on these models, CHF seems to be limited by heater size modulated hydrodynamics on finite well wetted surfaces (see Fig. 4.8).

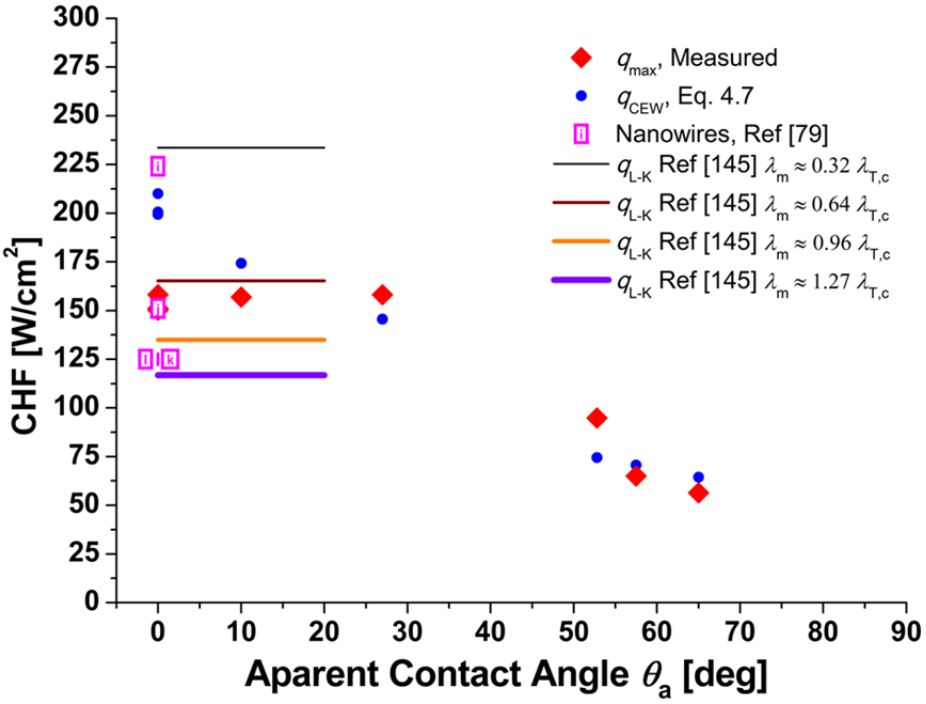

Fig. 4.10 Comparison of measured data (red diamonds), to model Eq. (4.6) for various λ_m (flat lines), model given by Eq. (4.7) (blue circles), and data for well wetting nanowire surfaces on varied finite heater sizes (magenta - λ_m used in Eq. (4.6) corresponds modulations by hater sizes used in Ref. [79], eg. $W = 0.5$, 1, 1.5, and 2 cm). Constant K = 1/24 is found to agree better with low contact angle data and is determined based on the heater surface area.

Note that pool boiling experiments studied on biporous micropillar arrays in this dissertation and those on similar monoporous structures in [144] occurred in parallel on a timeline basis, however the findings in [144] were published first and are referenced here. The rest of this section will focus on the differences in the data and new observations.

In order to probe the contribution of the capillary pressure to the CHF and determine if it can be extended via rewetting from heater edges, micropillar array structures series X of similar depth and porosity to series A but reduced pore sizes p were fabricated thus increasing the capillary term of Eq. (4.3c). The capillary term is nearly doubled by the reduction in p. Visual evidence indicated similar evolvement of bubble dynamics and surface rewetting as in Fig 4.6 and behavior at CHF as in Fig. 4.8. What is interesting to note in Fig. 4.11(left) is that the CHF in samples with lager pores (data series A) was approximately equal to the CHF of samples of similar depth $H \approx 79$ µm but smaller pores (data series X). Thus the capillary pressure was not as significant at rewetting the surface as is the bulk liquid flow induced by the detaching secondary bubbles. This further supports the claim that CHF is limited by hydrodynamics of liquid/vapor flow where instabilities are formed near the surface and defined based on heater size W, as indicated by the trend in Fig. 4.10.

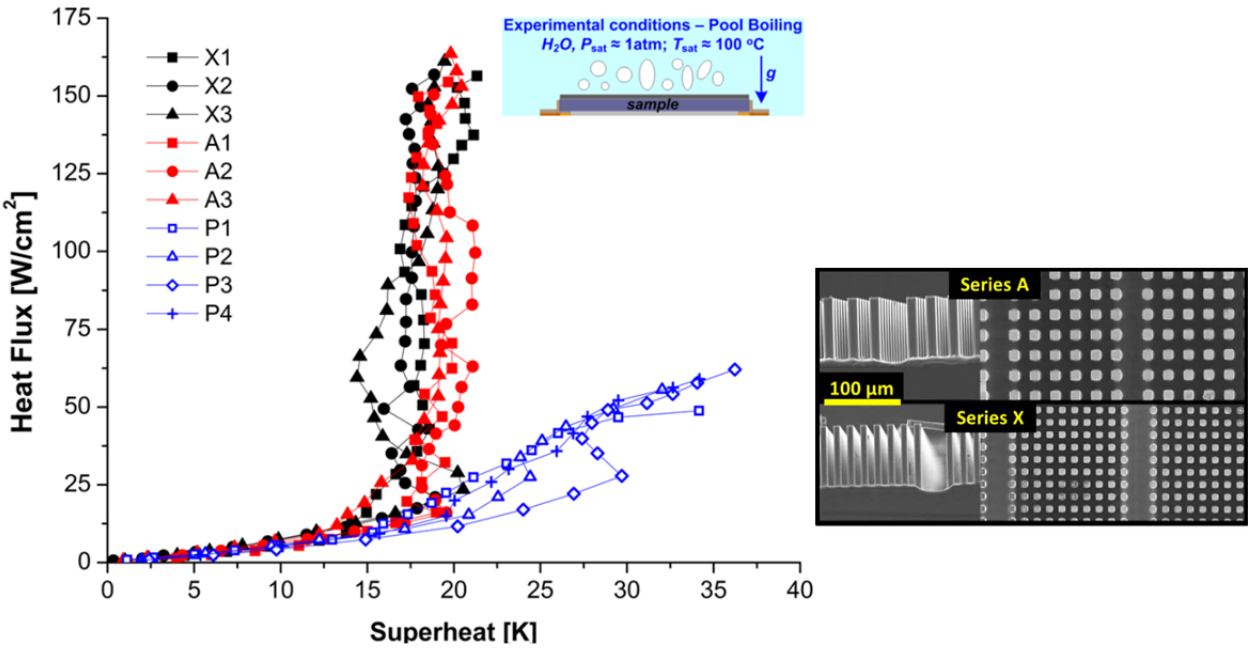

Fig. 4.11 (left) Heat flux versus superheat data for two different pin fin array structures series A and X with parameters summarized in Table 4.2. All samples here have a depth H in the range between 79 ± 3.5µm. Data obtained on plain silicon surfaces is shown for reference; (right) SEM images of samples series A and X with a universal scale bar.

Looking more closely at pool boiling data leading up to the CHF values reported in Fig. 4.9 it is evident that although wick depth does not affect CHF strongly beyond a certain depth H, it has a prominent effect on HTC. Figure 4.12 shows data for several sample series of varied depth summarized in Table 4.2. Only a pair of data sets is shown in order to avoid clutter, yet these are selected so that they capture the entire breadth of the measured superheat for a given H (all other not included data fall within the envelopes formed by the presented data). The breadth of the data can be attributed to several possible factors such as the stability of nucleate boiling

which is reduced for shallower wicks, and nucleation site density variation from sample to sample, which was not determined systematically in these experiments. For deeper wicks, the onset of boiling occurs at lower superheat, is more uniform across the heater surface, and the HTC is significantly increased. For $H \approx 180$ μm, the onset occurs at approximately 5 K and is verified visually, while for shallower wicks the onset is evinced by the sharp transition in the slopes of the data in Fig. 4.12 and varies due to more prominent bubble nucleation near heater edges observed at low heat fluxes. The quantitative nature of the onset could have a similar reasoning as that offered in Chapter 3, where the added micropillar depth increases thermal resistance along the micropillar length thus supplying larger local superheats near the array base necessary for bubble nucleation. Peak HTC values as defined by Eq. (4.2) for these samples recorded at or near CHF are summarized in Table 4.3. The enhancement in HTC seems to be directly related to three factors: a) higher nucleation site density visually observed in deeper wicks at lower superheats which is presumably maintained as heat flux is increase (implied by the larger secondary bubble diameters in Fig. 4.7); b) the increased total surface area for heat transfer (total area of all pins and exposed base – see Table 4.2); c) separation of wetting characteristics within the micropillar array which are presumed to be comparable to those measured on the plain surfaces P, and wetting over the whole array captured by the apparent contact angle. The last characteristic may act to promote bubble nucleation as vapor is trapped during the chaotic boiling process. The variation of HTC near CHF for different H is summarized in Table 4.3.

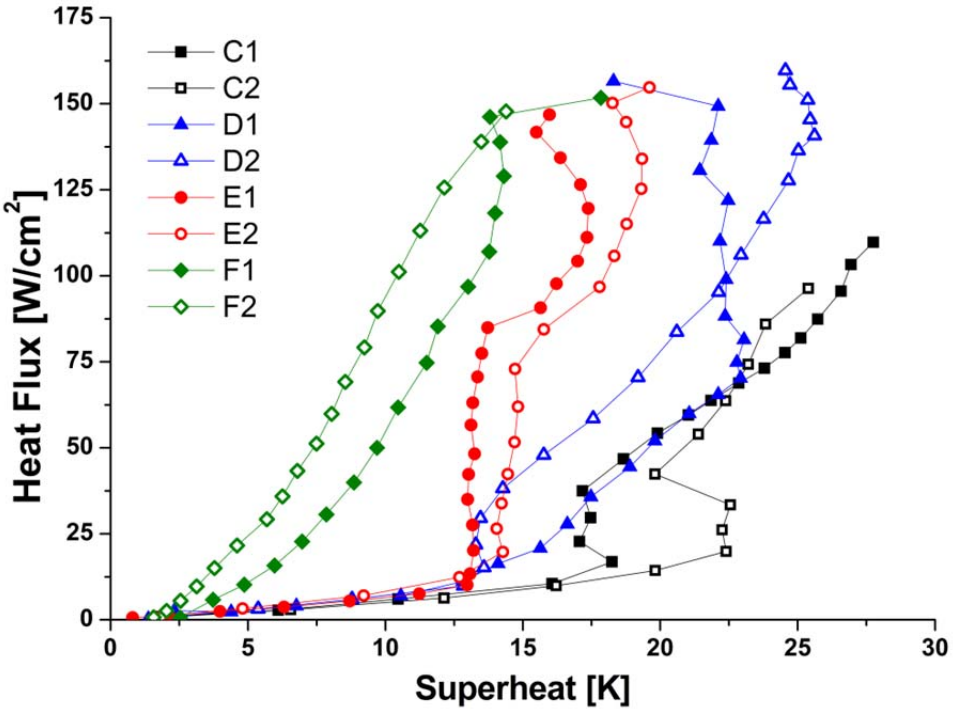

Fig. 4.12 Pool boiling data on biporous micropillar arrays of varied depth and parameter values summarized in Tables 4.2 and 4.3.

Table. 4.3 Summary of pool boiling experimental presented in Figs. 4.9 and 4.10.

Sample	Depth H [μm]	Pin Size d [μm]	Peak HTC [W/cm^2-K]	CHF [W/cm^2]	A_{total}/A_{plain}	CHF/CHF$_{plain}$
A1	79.7 ± 3.4	13.3 ± 0.6	8.60 ± 0.68	156.90 ± 9.02	5.93 ± 0.23	2.79 ± 0.33
A3	79.7 ± 3.4	13.3 ± 0.6	8.25 ± 0.93	163.54 ± 9.02	5.93 ± 0.23	2.90 ± 0.34
C1	6.5 ± 0.2	14.3 ± 0.2	3.95 ± 0.82	109.71 ± 21.49	1.43 ± 0.03	1.95 ± 0.43
C2	6.5 ± 0.2	14.3 ± 0.2	3.79 ± 0.87	96.36 ± 21.49	1.43 ± 0.03	1.71 ± 0.43
D1	29.8 ± 0.8	13.7 ±0.2	6.75 ± 0.63	156.59 ± 6.70	2.90 ± 0.09	2.78 ± 0.31
D2	29.8 ± 0.8	13.7 ±0.2	6.5 ± 0.38	159.63 ± 6.70	2.90 ± 0.09	2.83 ± 0.31
E1	146.7 ± 6.8	13.1 ± 0.2	9.15 ± 0.54	146.84 ± 3.30	9.95 ± 0.41	2.61 ± 0.27
E2	146.7 ± 6.8	13.1 ± 0.2	9.12 ± 0.53	151.05 ± 3.30	9.95 ± 0.41	2.68 ± 0.28
F1	178.8 ± 8.5	12.7 ± 0.2	10.59 ± 0.68	151.76 ± 2.25	11.58 ± 0.49	2.69 ± 0.28
F2	178.8 ± 8.5	12.7 ± 0.2	10.30 ±0.87	147.76 ± 2.25	11.58 ± 0.49	2.62 ± 0.27
X1	79.0 ± 2.2	7.6 ± 0.1	7.57 ± 0.36	156.42 ± 3.59	9.74 ± 0.41	2.78 ± 0.29
X3	79.0 ± 2.2	7.6 ± 0.1	8.31 ± 0.57	161.10 ± 3.59	9.74 ± 0.41	2.86 ± 0.30
P - Plain	N/A	N/A	1.72 ± 0.18	56.33 ± 5.76	1.0	1.0

Figure 4.13(top) shows HTC obtained at CHF from Table 4.3 normalized with respect to the peak HTC of plain surfaces P and the total surface area enhancement (A_{total}/A_{plain}). This plot serves to show the capability of different micro and nano porous structures to enhance HTC. The work of Chu et al, Lu et al, and Li et al is also presented in the figure,[79,80,144] where the apparent contact angle measured on plain surfaces were larger than that on a modified surface. For nanowire and nanorod structures,[79,80] the increase in surface area due to nanostructuring is significant and the porosity ϕ relatively large (~0.3). This normalization, and observations that enhancements in HTC are seen in their data indicates that a very small portion of the volume within the nanowires is active in the bubble generation process (green/blue arrow indicates that actual surface area enhancement is significantly larger). This idea motivates alternate modifications that will be presented in the following section. The micropillar structures considered here and in [144] indicate better activity within the porous array compared to nanostructured surfaces, the former giving better HTC performance for a given surface area based on a larger smooth surface apparent contact angle of $\theta_\alpha \sim 65^o$, compared to reported in the latter work $\theta_a \sim 25^o$. These contact angles are presumed to characterize actual wetting within the porous array of micropillars rather than what is observed through macroscopic apparent contact angle measurements modified by the presence of the microstructures, where higher contact angle surfaces are known to promote bubble nucleation.[68]

Microstructuring and nanostructuring smooth surfaces made of materials that have different wettability can therefore be used to modify HTC without compromising CHF by separation of wettability characteristics within the porous media from those observed macroscopically. This suggests pathways for optimizing CHF and HTC simultaneously. A similar normalization is performed on CHF in Fig 4.13(bottom) and data of relevant work by other researchers on similar length scale monoporous structures is presented. Even for a different working fluid system (FC-72 on Si,[75,76]) this normalized CHF trend is similar, and the comparison is valid given that the normalization eliminates dependence on any physical parameters. Although CHF can be enhanced via microstructuring a smooth surface, it appears

that irrespective of the initial apparent contact angle on the starting smooth surface, the surface area change via microstructuring dominates the CHF enhancement trend as compared to smooth surfaces. Comparison of the two plots in Fig. 4.13 supports the idea that CHF limitations do not depend so much to phase change characteristics within the porous medium (Fig. 4.13(top)), but more so the bubble interaction near and away from the surface.

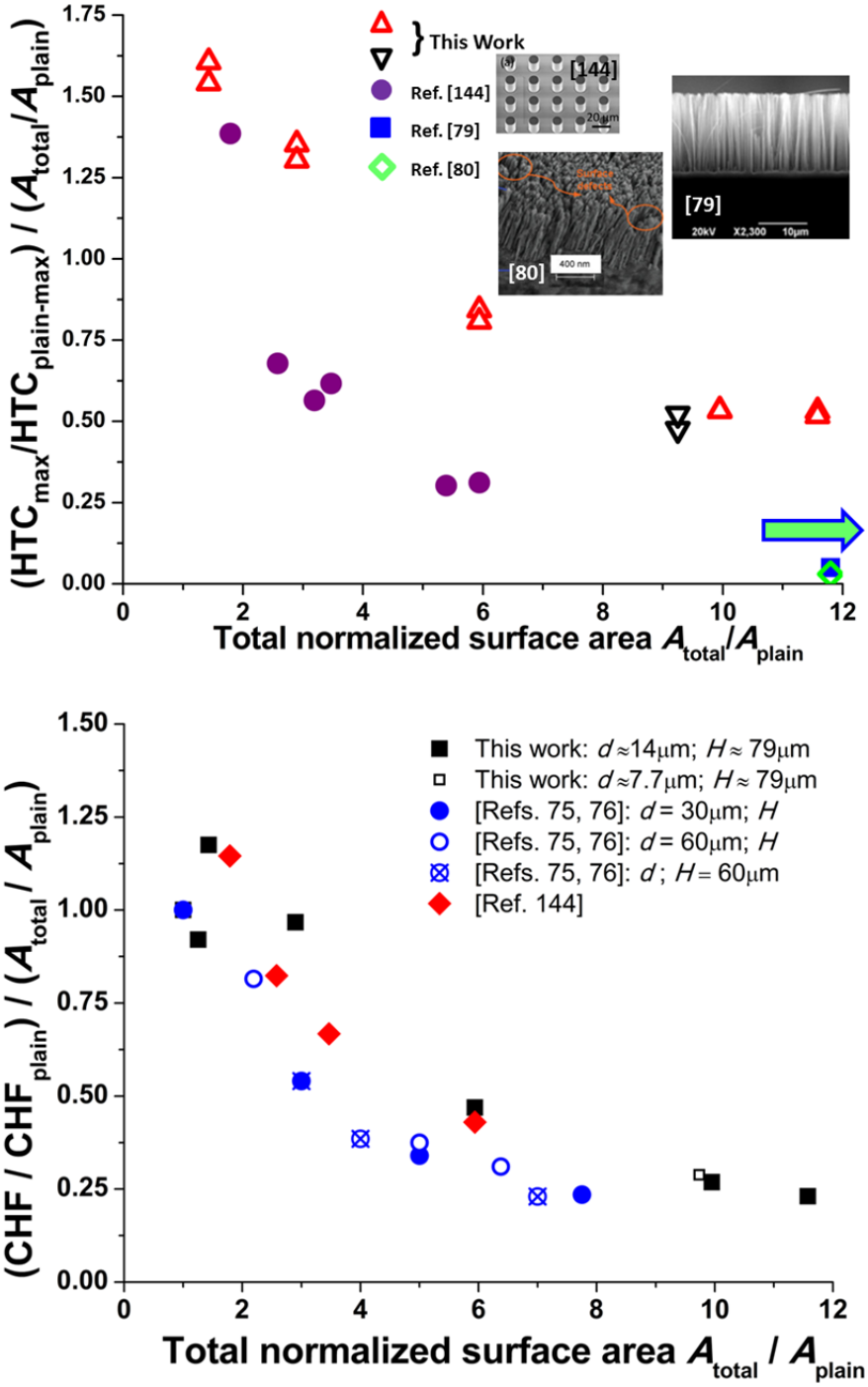

Fig. 4.13 HTC (top) and CHF (bottom) normalized with respect to total surface area and data obtained on smooth surfaces; relevant work from literature is presented for comparison.

4.3.2 Hybrid Micro/Nano Structured Surfaces for Enhanced HTC in Pool Boiling Systems

Nanowire and nanorod arrays have already shown promising performance characteristics.[78–80] Li et al argued that copper nanorod structured surfaces combine effects of trapping gas in nanoscale features and promote bubble nucleation via larger (microscopic) surface defects of the nanowire array; they concluded that in this manner HTC is increased while CHF is not compromised.[80] They observe that the increse in HTC is manifested via ~3 fold increase in bubble release frequency, smaller departure diameters, and up to a 30 fold increase in nucleation site density. Chen et al and Lu et al claimed that increased wettability and bubble nucleation were simultaneously responsible for enhancements in CHF and HTC on nanowire surfaces.[78,79] However, structures containing nanowires have not been modified in a controlled fashion for better HTC performance and the limits of enhancement are not known. A systematic study of artificially engineered micro-cavities, their size and density effects on HTC and CHF is presented here. Highest uncertainties are reported in the data from a single measurement or measurement repeatability as appropriate (See Appendix. A1.2 and A1.3). In these, and all other experiments incorporating cavities, the choice of the parameter s_c (see Fig 4.1 and Table 4.1) was predicated based on previous work done by Hsu,[116] and under the assumption that the cavity pitch $p_c = (s_c + d_c)$ defines the boundary layer thickness δ_t (See Chapter 2.2.2, Eqn. 2.31). This assumption was chosen considering a worst case scenario where all cavities are active and merge when the bubble diameter is equal to p_c. Any larger bubbles would then merge and detach from the surface, where beyond $\delta_t = p_c$ the temperature field would be more uniform due to the turbulent nature of bubble interaction. Inset of Fig. 4.14 illustrates the scenarios for the smallest pitch p_c implemented in this investigation for cavity sizes of d_c = 11 μm and d_c = 41 μm shown by dashed horizontal lines. According to Hsu's model, any boundary layer thickness greater than the minimum p_c used in this investigation would further ensure that all cavity sizes implemented would activate at low superheat (< 10 K) and remain active. The presence of the nanowires would also serve to broaden the spectrum of available cavity sizes as suggested in other works,[78–80] and further validate the implementation of Hsu's model here. This analysis governs the parameter space summarized in Table 4.1 and shown in Figs. 4.1 ans A1.7 thus enabling the comparison of how cavity geometry and density influences stability of bubble nucleation and heat transfer performance.

Figure 4.14 (left) illustrates the data comparing a bulb-reentrant cavity array of mouth sizes $d_c \approx 41$ μm on a nanowire surface of depth $H_{nw} \approx 35$ μm versus a plain rectangular cavity array on a nanowire surface with similar characteristics (SeeTable 4.1). From the data and the slope, once nucleate boiling initiates it is evident that reentrant cavities yield no HTC improvements (via active site density or stability) in performance over plain rectangular cavities of aspect ratio (D_c/d_c ranging from 1 to 2) when incorporated on surfaces with great wetting characteristics ($\theta_{nw} \leq 10^o$). This is also verified visually, where both types of cavities are active at low q and remain stable over a broad range of superheat as CHF is approached. Similar nucleation stability between these types of cavities for aspect ratios $D_c/d_c < 1$ was observed in a previous study by Shoji et al on smooth surfaces.[136] Table 4.4 summarizes key dimensional parameters of the three samples presented in Fig. 4.14 (left) and the slopes indicating performance similarity in the nucleate boiling regime. From this data, no clear benefit of implementing bulb-reentrant cavities was observed.

For all other presented data (apart from ~40 μm cavities), rectangular cavities of high aspect ratio are used instead ($D_c/d_c \geq 4$, at the least), where vapor trapping is expected based on

two presumptions: a) nanowires are NOT present within the cavities (confirmed via SEM) thus yielding higher apparent contact angles ($\theta_{plain\text{-}Si} > 10^o$) in case liquid were to penetrate – indicating again a separation of wetting characteristics within and on the surface; b) vapor trapping is manifested in the sharp corners of the rectangular cavity profile during the chaotic process of surface rewetting. This latter is determined via geometric analysis and measured contact angles (Fig. 4.14 (right)) where the angle formed by these dimensions ($\tan^{-1}(d_c/D_c = 1/4) \approx 14^o$) is comparable to the contact angle observed between DI water and the nanowire arrays, and lower than that observed on clean or aged silicon surfaces (see Table 4.2 or Ref. 78). Additionally, the high capillary pressure produced by the dense nanowire array ($Pc_{nw} > 1.1$ MPa estimated based on average nanowire spacing ≤ 100nm from SEM images just around the cavity mouth edges) could be responsible for keeping the liquid from penetrating too deep into the cavity during bubble ebullition, thus evading the need of reentrant cavities. The pressence of the nanowires at the contact line around the cavity mouth may alter local surface properties and make the voids in the surface produced by cavities behave like local hydrophobic spots. Other studies have shown that hydrophobic regions on hydrophillic surfaces may aid heat transfer performance and bubble nucleation.[129]

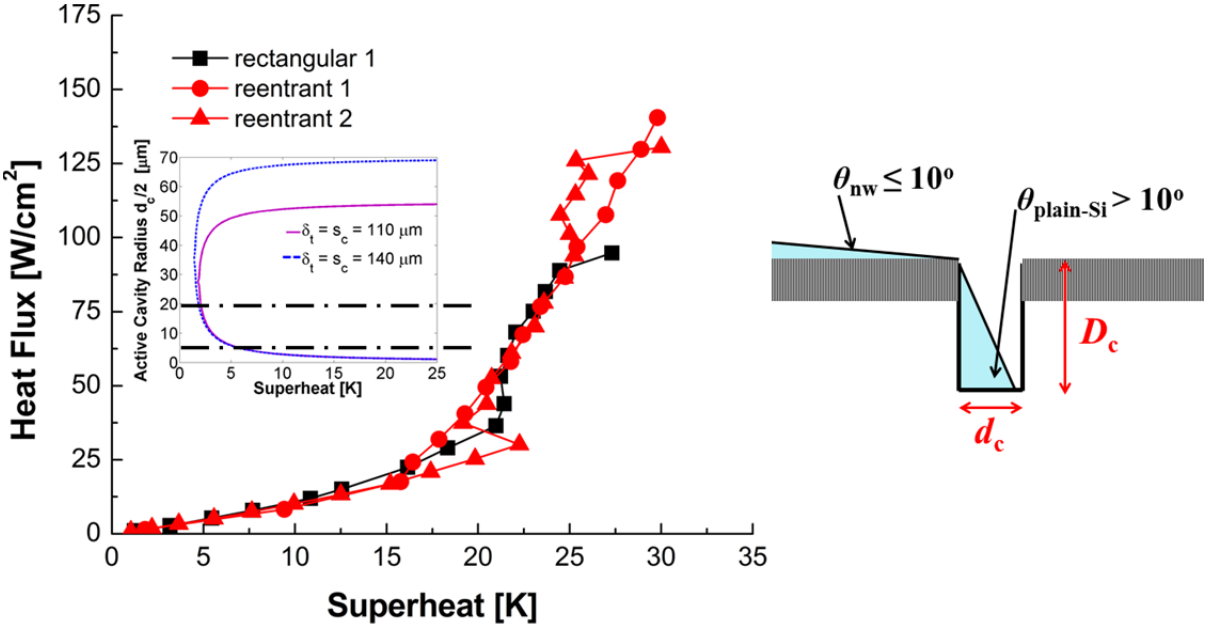

Fig. 4.14 (left) Data indicating that reentrant and rectangular cavities are equally stable over a broad range of heat fluxes, and active in the range of superheats in good agreement with Hsu's model [ref. 116]. The presented data is for $H_{nw} = 35$ μm, $p_c = s_c + d_c \approx 140$ μm samples (maximum variation in any dimension ~ 5 % among the 3 samples). NOTE: the sample with rectangular cavities detached during the experiment, thus the CHF is lower but the reentrant versus rectangular cavity trend as far as active nucleation sites are concerned is illustrated and visually confirmed; (right) rectangular large aspect ratio D_c/d_c cavities implemented to ensure vapor trapping based on geometry, and difference in apparent contact angles on the nanowire surface and within the cavity.

Table 4.4 Dimensional characteristics of reentrant and rectangular cavities and their performance in the nucleate boiling regime.

Sample type	d_c	s_c	D_c	Slope [W/cm²-K]
Reentrant 1	39.4	100	57	9.5 ± 0.47
Reentrant 2	40.7	100	55	10.1 ± 0.5
Rectangular 1	38.3	100	50	10.5 ± 0.52

Top of Fig. 4.15 shows the effect of cavity density on pool boiling performance. In this figure, samples of cavity size $d_c \approx 11$ μm, and average nanowire depth $H_{nw} \approx 35$ μm are shown. All cavities have a rectangular cross section. The data indicates that HTC increases with increased cavity density. In addition, the presence of cavities yields a much steadier slope to the q vs. ΔT curve rather that the more chaotic behavior observed for a cavity free nanowire surface of same nanowire depth. Data for the plain nanowire samples is found to be in pretty good argreement with the data published by Lu et al.[79] which is also plotted in the Fig.4.15; the difference in CHF values in this study and Ref. 79 may be do to slightly greater contact angle values measured here.

Cavities of this size show increased heat transfer efficiency via nucleate boiling with increasing density, although cavities of 200 μm and 100 μm spacing do not give significantly different performance. A very slight reduction in CHF is observed as cavity density increases. Small reduction in CHF may also be atributed to variations in measured contact angles, but it is not significant enough to claim that nucleation density affects CHF. Figure 4.15(bottom) shows data for 100 μm and 800 μm spacing for cavities of size $d_c \approx 41$ μm. By comparison of Fig. 4.15(top) and Fig. 4.15(bottom) it is evident that larger cavities on nanowire surfaces are much less efficient at nucleate boiling heat transfer in the regime where $s_c/L_c < 3$, a cavity density regime claimed to exhibit very complex bubble interactions in other works.[140] This is most likely due to the large void volume that larger cavities occupy within the surface (eg. at peak density shown in Table 4.1, ~ 40 μm cavities occupy ~ 0.6 mm^3 within the surface while 10 μm cavities occupy ~ 0.04 mm^3), and thus more heat transfer interactions that may promote bubble deactivation near the surface. Some performance characteristics are compared in Table 4.5.

In Fig. 4.15, Rohsenow's model (Chapter 2.2.3 Eq. (2.28)) is also incorporated with the constant C_{sf} serving as the fitting parameter for both cavity sizes.[17,117] For 11 μm cavities $C_{sf} = 0.0115$, while for 41 μm cavities $C_{sf} = 0.019$. With these values Rohsenow's model fits the data trend very well, and because the surface tension in the system can be assumed the same between experiments and the apparent contact angle on the whole surface variation between samples is small, the different values of C_{sf} for different cavity sizes supports the claim that smaller cavities do seem to be more efficient at nucleate boiling heat transfer, particularly at higher heat fluxes. They also exhibit bubble nucleation onset verified experimentally at lower superheat (~6 K and ~15 K for $d_c = 11$ μm and $d_c = 41$ μm respectively). This disparity in performance and deviation from predictions of Eq. (4.1) which suggests that smaller cavities should nucleate at larger superheat, may indicate different bubble dynamic characteristics (departure diameter and frequency), and different cavity wetting characteristics near cavities of different sizes present within nanowire surfaces. Increases in peak HTC near CHF up to 213 ± 20 % as compared to a cavity free nanowire surface are observed in this investigation.

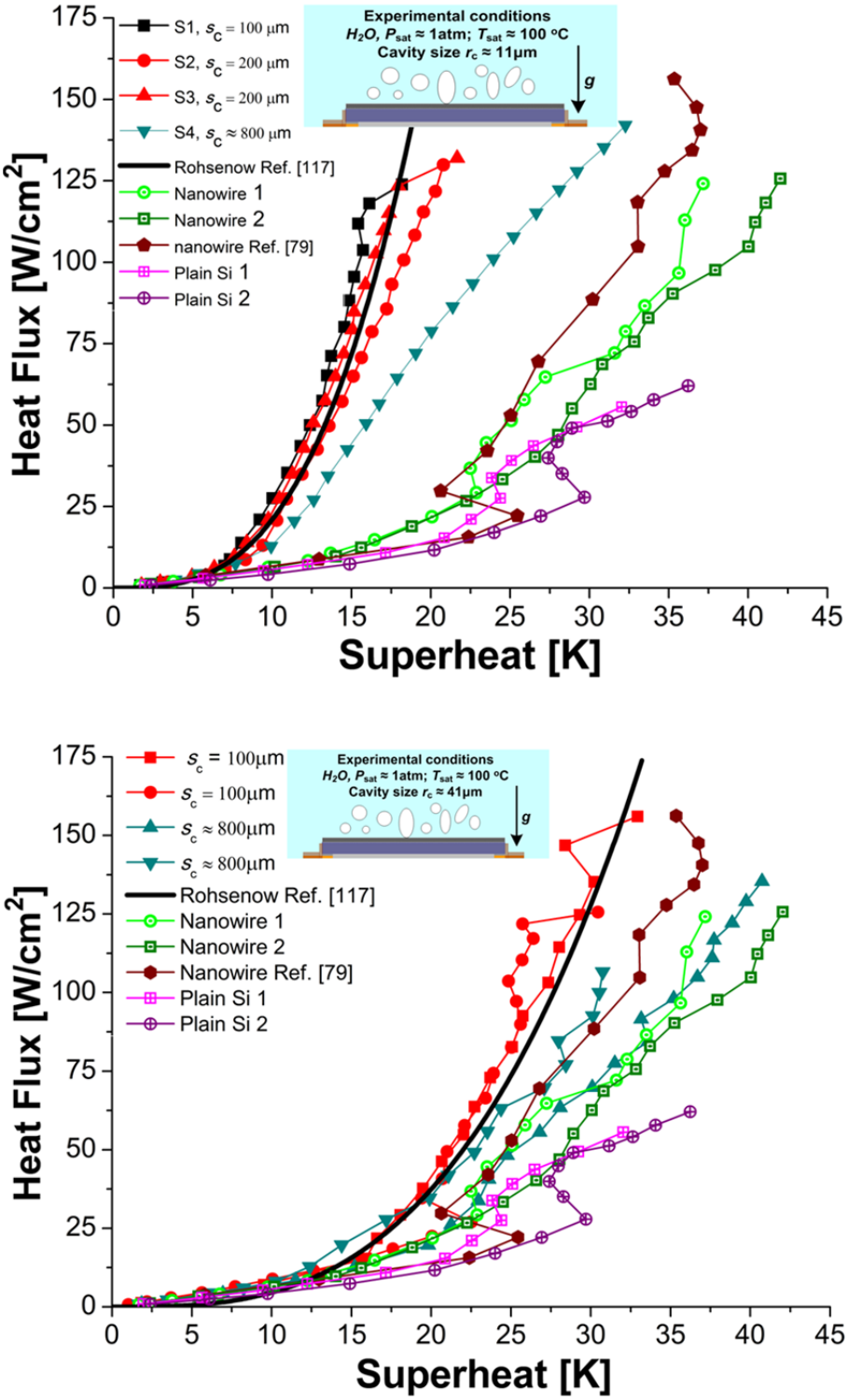

Fig. 4.15 (top) Data illustrating cavity density effects on pool boiling performance for $d_c \approx 11$ μm, $H_{nw} \approx 35$ μm; $C_{sf} = 0.0115$ for fitting the Rohsenow model for $s_c = 100$ μm; (bottom) data illustrating cavity density effects on pool boiling performance for $d_c \approx 41$ μm, $H_{nw} \approx 35$ μm; $C_{sf} = 0.019$ for fitting the Rohsenow model for $s_c = 100$ μm. Experiments are done with all sample surfaces lying horizontally as shown in the insets of each figure.

Table. 4.5 Summary of peak HTCs of data presented in Fig. 15 at comparable heat fluxes $q \approx 110$ W/cm^2; data from ref. [79] is included for comparison.

$s_c/d_c/H_{nw}$ [μm]	Peak HTC [W/cm^2-K]	$HTC_{cav}/HTC_{nanowire}$
100/11/35	6.40 ± 0.32	2.13 ± 0.20
800/11/35	4.30 ± 0.25	1.43 ± 0.14
100/41/35	4.61 ± 0.91	1.54 ± 0.33
800/41/35	3.16 ± 0.26	1.05 ± 0.12
nanowire	3.00 ± 0.23	N/A
nanowire [ref. 79]	3.20 ± 0.23	N/A

Lastly for this section, pool boiling HTC of several geometries are ploted as a function of heat flux q in Fig. 4.16. In addition, a capillary wick micropillar structure studied in Chapter 3 is included for comparison. Both micropillar and hybrid micro/nano structured surfaces yield a significant performance increase as compared to plain surfaces attesting to using multi-length-scale features for enhancing heat transfer performance. As micro and nanostructuring configurations are changed to manipulate HTC, CHF does not seem to be significantly affected on surfaces with low apparent contact angle. This suggests that boiling withing the micro and nano porous media is not responsible for CHF onset but rather bubble interaction near and away from the surface. When comparing thin liquid film data (magenta downward triangles), to pool boling data on the same structures (black sideway triangles), it is evident that the free surface in the former yields better HTC at low heat fluxes where evaporation is the dominant mode. As the heat flux is increased, pool boiling HTC (black sideway triangles) dominates indicating that more surface area is active in the phase change process. The same can be argued once boiling is initiated in capillary wicking experiments and the ensuing increase in HTC is observed. The fact that HTC in the two experiments converges near ~150 W/cm^2 indicates that the active surface area in phase change is comparable in both pool boiling and capillary wicking experiments.

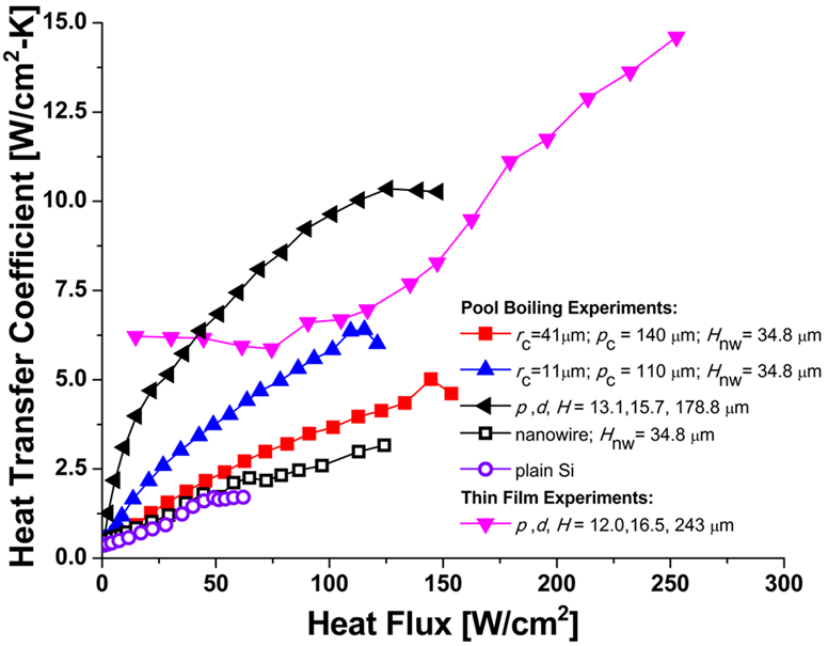

Fig. 4.16 Comparison of pool boiling heat transfer coefficient performance of several geometries indicated in the legend. All cavity samples have spacing $s_c \approx 100$ μm. Peak uncertainties are included in data tables.

4.4 Summary

In this chapter, a comparative systematic study on biporous microstructured surfaces was undertaken to distinguish between phenomena that limit CHF in pool boiling experiments where the presence of the liquid pool significantly affects bubble dynamics, and those in thin liquid film capillary experiments where the top surface is open to a saturated vapor environment. Additionally, the goal was to design structures that promote both HTC and CHF in pool boiling systems of finite size. The fact that HTC data indicates similar bubble activity in both systems on structures of similar geometries suggests that the free surface in capillary wicking experiments permits rapid vapor release and in that way keeps the phase change process active, delaying CHF. On the contrary, although the activity is similar in pool boiling experiments (via comparison of HTC), the presence of the liquid pool causes bubbles to interact near the surface hindering effective release. For finite, well wetted micropillar array surfaces hydrodynamic instabilities in the liquid/vapor flow near the surface appear to be triggered by the heater length scale in pool boiling experiments. Increasing capillary pressure via reduction of micropillar pore size has yielded no enhancement to CHF in pool boiling indicating that convection of the surrounding liquid to the surface by the departing secondary bubble is more significant in surface rewetting.

This chapter also focused on performance of hybrid micro/nano structures in pool boiling experiments. Several cavity sizes were fabricated within nanowire surfaces and tested in order to determine what cavity size is most effective in reducing superheat for onset of nucleation in the regime where $s_c/L_c < 3$ and cavity interactions are significant. An attempt was made to further optimize pool boiling performance on previously considered silicon nanowire covered surfaces.[78,79] Reentrant and rectangular cavities yielded no significant difference in performance, and provided low superheat at boiling onset (as low as ~6 K), and stable boiling until CHF was reached. Smaller cavities (d_c = 11 μm) at peak densities (s_c = 100, 200 μm) yielded best HTC and did not appear to contribute to CHF reduction significantly. Because these hybrid surfaces also indicate good wetting, onset of CHF is similar as that observed on the micropillar surfaces studied here. The data trends agree very well with the behavior predicted by Rohsenow's model where C_{sf} is used as a fitting parameter.

Up to ~2.4 fold enhancement in HTC was observed at $q \approx 115$ W/cm^2 for a hybrid cavity/nanowire surface at peak cavity density (d_c = 11 μm, s_c = 100μm) as compared to a plain nanowire surface (7.3 ± 0.4 vs. 3.1 ± 0.5 W/cm^2-K respectively). Micropillar structures yielded HTC improvements up to 10.6 ± 0.7 W/cm^2-K at q = 147.2 ± 4.3 W/cm^2. Structures developed in these studies yield excellent enhancement of phase change heat transfer in pool boiling systems, that don't compromise CHF. HTC enhancements on microstructured and hybrid micro/nano structured surfaces are in part attributed to wetting characteristics within the porous media that differ to those that are observable macroscopically and altered by micro/nano structuring.

5. Fundamentals of Solar Energy Storage in Photosensitive Molecular Systems

In this chapter some fundamental photophysical and photochemical characteristics of photochromic systems are discussed. The intent here is to give an overview of how these molecular systems store solar energy, how they release it, and what are the desired properties for a viable solar energy storage system. Photochrome efficiency is also defined. More detailed considerations can be found in a book by Dürr and Laurent.[21]

5.1 Energy Storage in Molecular Systems - Principles

Photochemical reactions arise due to the interactions of electromagnetic radiation with the electron density distribution within matter. This occurs at resonant frequencies where the energy of electromagnetic radiation ($\varepsilon = h\nu$) at a certain frequency υ matches up with the distance of energy levels within a molecular system. This interaction can change the electron distribution permanently and excite molecules to different energy states. For example, when electromagnetic radiation passes through matter, its interaction with molecules can change the incident radiation amplitude, change the electron density distribution within the molecules, or change the electron distribution between two energy states. These are all caused by energy transfer between the electromagnetic radiation and the molecular system. Molecular systems are typically sensitive to interactions with UV and visible parts of the solar spectrum. A general pathway of this interaction can be defined as

$$A + h\nu \longleftrightarrow A^* \longleftrightarrow B \qquad (5.1).$$

Here, molecule in state A is excited via a photon of energy $h\nu$ to an excited metastable state A^* from where it can relax to a stable higher energy state B or back to the original state A. When considered from the excited state B, the energy difference between the higher excited state A^* and the state B is the energy barrier E_a that needs to be overcome to relax the molecule to the original molecular state A (see Fig. 1.4 in Chapter 1.3).

In most photochromic systems, the energy exchange yields unstable and short lived excited states A^*. This is especially true for systems where the absorbed energy can be dissipated in the rotation, translation, or vibration of molecules. These deactivation pathways are responsible for low quantum yield Φ (typically $\Phi < 1$ in photochromic systems). In more general terms, the quantum yield of a molecular system is defined as the number of times a specific event occurs per photon of light absorbed for a radiation-induced process. Therefore, for solar energy storage in molecular systems, the quantum yield quantifies the number of successful transitions of a molecule from a ground energy state (e.g. state A Fig. 1.4) to an excited state (e.g. state B Fig. 1.4) $n_{A\rightarrow B}$, per number of photons absorbed n_p

$$\Phi = \frac{n_{A\rightarrow B}}{n_p} \qquad (5.2).$$

In contrast to absorption of photons, spontaneous and induced emissions are also important in these molecular systems. In the process of emission, a molecule undergoes a transition from the excited to the ground state while it emits a photon. Spontaneous emission occurs due to energy fluctuations within a molecular system, while induced emission can occur due to other factors such as excitement by electromagnetic radiation. In this way, even if a

molecule is excited to state B, interaction with incident radiation can induce a transition back to a lower energy state A. For energy storage purposes, a stable excited state, high quantum yield, and controlled emission is necessary for creating an effective system.

5.2 Criteria for Effective Solar Energy Storage Molecular Systems

Below is a summary of different photochemical processes and reaction types can be distinguished into several groups as,[21]

$$A \xrightarrow{h\nu} (C + D; C^+ + C^-; C^+ + e^-)$$

$$A + C \xrightarrow{h\nu} D$$

$$A_1 + A_2 \xrightarrow{h\nu} A_3$$

$$A \xrightarrow{h\nu} B \qquad (5.3a\text{-}d).$$

In spontaneous monomolecular deactivation processes Eq. (5.3a), a molecule can be broken down into radicals, ions, two other stable molecules, or into a positive ion and electron pair. If dissolved in a solvent or a non-inert environment, a molecule can also react with other reactants within the system (Eq. (5.3b)) to form other compounds (e.g. photoaddition, photoreduction, etc.). Also, photopolymerization can occur (Eq. (5.3c)), where the reactant molecule polymerizes to form a polymer chain. Finally, a rearrangement reaction (trans-cis-photoisomerization) can occur, where a molecule undergoes a change in geometric structure between stable states A and B (Eq. (5.3d)). The last of these four photochemical reaction groups can be treated as a type of phase change transition of a molecular system if the rearrangement is reversible, and the chemical composition is completely maintained. Considering the last reaction type Eq. (5.3d) more closely, in order to be viable solar energy storage and power generation systems, these photochromic molecules must possess several properties [22,23,90,100,101]:

(a) Eq. (5.3d) must be endergonic where product B is at a higher energy state than product A (see Fig. 1.4) and the reaction must be reversible, thus the exergonic back reaction must yield complete conversion of B→A.

(b) Both forward and back reaction must have high recyclability rates with almost no degradation either in pure form, in solution of a working fluid, or when in contact with any potential catalyst to be used in a practical energy storage/power generation system.

(c) A→B transformation should have a high quantum yield Φ.

(d) Molecule A should absorb the portion of the solar spectrum in the UV and visible range to which molecule B should not be sensitive.

(e) The energy barrier for the back reaction (E_a in Fig. 1.4) should be sufficient so that the back reaction is slow or completely prevented at room temperature conditions to allow for long term energy storage.

(f) The ground state energy level of compound B should exceed that of A by a significant amount ($\Delta H_{storage}$~250 J/g, e.g. 1g of compound sufficient to heat 1g of water by ~ 60 ^oC, or comparable to other solar thermal systems summarized in Table 1.1).[11,12]

(g) The exergonic reaction from B→A in Eq. (5.3d) must be susceptible to catalytic activation so that the energy can be released quickly even at room temperature conditions.

(h) Compounds A and B should be abundant, cheap, non-toxic, incombustible, nonexplosive, and easy to transport.

5.3 Photochrome Efficiency and Roundtrip Efficiency

In addition to the strict criteria for a functional and practical system, the overall efficiency of the photochrome should be high. The overall efficiency η_{pc} [%] of A→B conversion can be defined as follows,[22]

$$\eta_{pc} = \left(\frac{\Delta \hat{H}_{storage}}{hcN_A/\lambda_{\lim}} \right) \cdot \left(\frac{\int_{o}^{\lambda_{\lim}} I_\lambda(\lambda/\lambda_{\lim})d\lambda}{\int_{0}^{\infty} I_\lambda d\lambda} \right) \cdot \Phi \cdot \eta_{abs} \qquad (5.4).$$

The first term in the parentheses is the energy conversion factor which is the ratio of the molar enthalpy $\Delta\hat{H}_{\text{storage}}$ (stored energy in molecule B) to the energy of one mole of photons with the threshold energy at wavelength $\lambda_{\lim}$ where c is the speed of light, h is Planck's constant, and N_A Avogadro's number. Wavelength $\lambda_{\lim}$ corresponds to the minimum energy required (E_g) to excite molecule A to the transition state A^* (see Fig. 1.4); any photon with $\lambda > \lambda_{\lim}$ will not cause this transition. In other words $\lambda_{\lim}$ is the long wavelength limit of absorption of compound A. The second term is the fraction of energy useful for photoconversion of A→B; it is the ratio of useful energy (as determined by the absorption spectrum range of A) to the incident solar flux. The third term is the quantum yield Φ as defined in Eq. (5.2). Finally, the last term is the overall absorption of molecule A (fraction of light absorbed for $\lambda < \lambda_{\lim}$). With sufficient residence times and minor degradation in most systems this can be as high as $\eta_{abs} \sim 0.75 <$.[100] The theoretical limits of these energy storage systems are estimated in the range of 20 – 30%,[24,25] but a reasonable goal for a practical system is approximately 10%.[100]

The round trip efficiency of a working molecular solar energy conversion system where no degradation is observed should depend on the photochrome efficiency η_{pc}, the efficiency of the back reaction triggered by a room temperature catalyst η_{cat}, and the efficiency of any heat exchanger η_{he} implemented to transfer the heat for power generation. Thus the overall round trip efficiency η is defined as

$$\eta = \eta_{pc} \cdot \eta_{cat} \cdot \eta_{he} \qquad (5.5).$$

In a realistic system, degradation of the photochrome is inevitable especially when working with solution based systems or systems where homogeneous or heterogeneous catalysts are used. Thus the actual efficiency should be somewhat lower than that defined in Eq. (5.5) especially in applications where molecules undergo this type of phase change transformation over many repeated cycles.

6. Molecular Solar Thermal (MOST) Energy Storage and Conversion System

In this chapter, the focus is on the design and construction of a microfluidic molecular solar thermal (MOST) device that uses a new bis(1,1-dimethyltridecyl) substituted derivative of $FvRu_2$ to demonstrate the technical feasibility of solar energy storage and "on demand" conversion to heat (Fig. 6.1). In the forward reaction, compound **1** is photoisomerized to **2** (energy storage), and in the reverse reaction, a catalyst facilitates the stored energy release in the form of heat, yielding a measurable temperature rise. While the chemical aspects of MOST suggest many different paths for further optimization and improvements, the focus here is on a proof-of-principle platform that will also accelerate the screening for other molecular targets and catalysts, and demonstrate that both energy storage and direct and continuous solar energy conversion to heat are feasible.

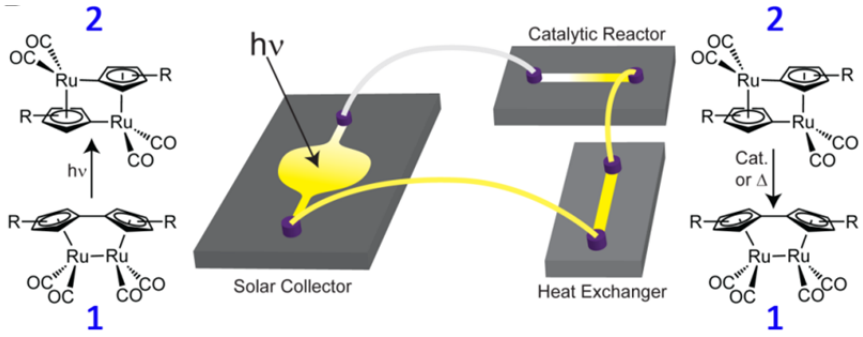

Fig. 6.1 MOST device developed in this study: The working fluid contains compound **1** that is photoconverted in a high surface area microfluidic solar collector to form photisomer **2** (R = 1,1-dimethyltridecyl). The solution can be pumped directly into a heterogeneous catalytic converter, in which the stored energy can be extracted by heat exchange.

6.1 Background, Motivation and Survey of Previous Work

Utilization of solar energy in either photovoltaic or solar thermal power generation is limited by the inherent challenge of load leveling and intermittency of solar radiation.[13,14,19] In these power generation systems, development of large scale electrical and thermal energy storage technologies that would mitigate these constraints has been challenging.[13,14,19,84,148–150] In conventional oil- and coal-based power generation, energy stored over geological time scales in the form of chemical bonds is released by combustion „on demand". A great deal of current effort is devoted to mimicking this process on a shorter time scale by the creation of solar fuels via the splitting of water to form H_2 and O_2, or similar schemes to produce alcohols and other fuels from CO_2.[13,88,151] In this context, a closed cycle that reversibly stores energy upon exposure to sunlight (a photochemical reaction), followed by a second, on demand reaction, that generates heat and regenerates the original reactant, is very attractive as a renewable storage media for solar energy (Fig. 6.2).[88] A molecule (the „parent") must be photoconverted to a stable higher energy isomer (the „photoisomer"). The latter then releases its energy as heat by reversing to the parent on thermal excitation. This reversible chemical transformation can be regarded as a change of phase type reaction where molecules transition between different structural configurations. The implementation of this concept is

challenging, since both parent and isomer molecules need to satisfy a large portion of criteria established in Chapter 5.2.

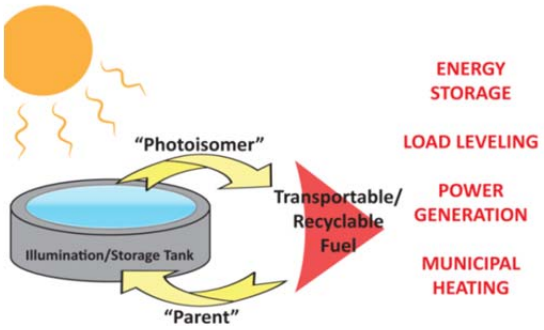

Fig. 6.2 Conceptual illustration of a potential large scale molecular solar thermal energy storage system, in which solar energy is harvested and used cyclically for „on demand" applications.

A number of organic compounds have been scrutinized in these respects, most notably the norbornadiene-quadricyclane (*N*-*Q*) system.[23,91,96–99] Although it has large energy storage capabilities, the *N*-*Q* system has thus far had limited practical use since it absorbs a very small fraction of the solar spectrum, and tends to form undesired byproducts during the photochemical conversion.[23] Organometallic (fulvalene)diruthenium compounds ($FvRu_2$) shown in Fig. 1.5 have shown promising solar energy conversion and storage properties due to their inherent stability and relatively large energy storage enthalpies (~195 J/g).[102–104] $FvRu_2$ is a solid powder at room temperature.[102,152] Since no photo-conversion of this compound is observed in its solid state and because it has poor solubility in common organic solvents, alternative forms of the compound have been synthesized in attempts to increase its solubility and thus increase the photo-conversion rate and energy density of the solution based system. A previously considered derivative of $FvRu_2$ the tetra-tert-butyl fulvalene diruthenium,[103] is rather soluble in tetrahydrofuran (0.34 M) but its photo-isomer has a surprisingly low solubility (0.02 M) thus limiting both rate and yield of photoconversion, and the stored energy density of the solution.[106] To overcome this, the $FvRu_2$ compound has been modified by the addition of long alkyl side chains to the fulvalene moiety to generate bis(1,1-dimethyltridecyl) substituted derivative of $FvRu_2$ to enhance solubility (Fig. 6.3).[153]

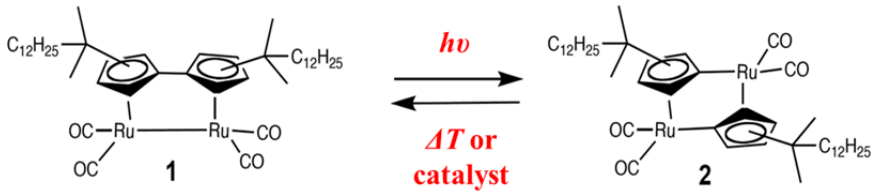

Fig. 6.3 Chemical structure of bis(1,1-dimethyltridecyl) substituted derivative of $FvRu_2$. The molecule undergoes a cis-trans phase transition during the energy storage-energy release steps.

6.2 Materials and Methods

6.2.1 Differential Scanning Calorimetry Measurements

Differential Scanning Calorimetry (DSC) measurements employed a TA Instruments Tzero Q20 calorimeter to determine the energy stored in the cis-trans structural phase transformation from molecule **1** to **2**. Photoisomer **2**, a viscous oil at standard temperature and pressure, was subjected to high vacuum to remove residual solvent toluene from its preparation,

and a small weighted amount was placed in an aluminum DSC pan. The pan was hermetically sealed and placed into the calorimeter. Data was collected from –30 °C to 250 °C at a 10 °C/min heating rate. The exotherm observed during the heat release step **2→1** shown in Fig. 6.4 was integrated to obtain the energy/mass ($\Delta H_{storage}$) in compound **2**. The flat portions of the DSC curve were used to obtain specific heat values of **1** and 2. The specific heat measurements were performed on several batches of parent compound **1**, where no phase transitions were observed and the heat flow data was steady with no observed humps. The averaged value for the $\Delta H_{storage}$ in compound **2** (5 measurements) was 110.8 J/g, and that of the specific heat 1.23 ± 0.15 J/g-K at 75 °C. The negative peak observed just prior to the heat release step is repeatable between samples, however it is not reversible. Thus it believe that this corresponds to a small amount of toluene or any other remaining solvent used during synthesis than might have remained trapped with compound **2** and evaporated during the DSC experiments.

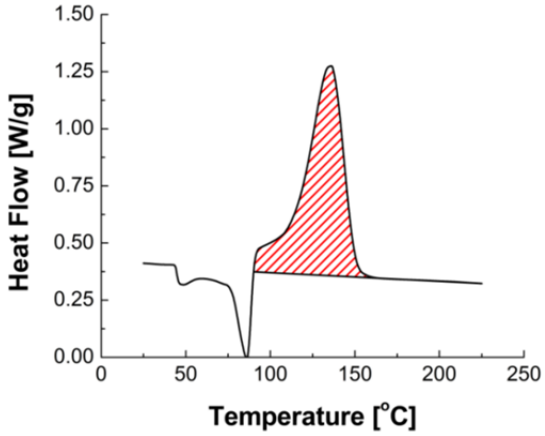

Fig. 6.4 Typical data plot obtained from DSC measurements. Positive peak (shaded in red) indicate exothermic phase transitions in this case (this is $\Delta H_{storage}$ energy released during **2→1** transformation), while the endotherms (negative) peaks indicate that some remaining solvent is evaporated off. (NOTE: relative position of the curve in the y-axis direction is not significant until it is adjusted with respect to a measurement device baseline established based on standard samples which is done for all presented data).

In addition to the plot in Fig. 6.4, Table 6.1 summarizes the energy density obtained by DSC experiments for all the candidate molecules considered for preliminary MOST device testing. These include the original $FvRu_2$ molecule shown in Fig. 1.5, (1,2-tetra-tert-butyldihydrofulvalene) substituted $FvRu_2$ and $FvOs_2$,[103] and bis(1,1-dimethyltridecyl) substituted derivative of $FvRu_2$ shown in Fig. 6.3. The specific heat was only determined for the bis(1,1-dimethyltridecyl) substituted derivative of $FvRu_2$, and compared against control measurements of standard sapphire samples summarized in Table 6.2.

Table 6.1. Results of the DSC experiments for several $FvRu_2$ and $FvOs_2$ derived compounds.

Compound	**Molecular Weight [g/mol]**	**Storage Enthalpy $\Delta H_{storage}$ [J/g]**	**Storage Enthalpy $\Delta H_{storage}$ [kJ/mol]**
$FvRu_2$	442.4	195.0 ± 18.5	89.6 ± 8.2
[5]ttBu-$FvRu_2$	666.8	132.8 ± 18.0	88.3 ± 12.0
ttBu-$FvOs_2$	845.1	56.62 ± N/A	47.8 ± N/A
[6]R-FvRu$_2$	***859.1***	***110.8 ± 20.6***	***95.2 ± 17.7***

[5] ttBu - 1,2-tetra-tert-butyldihydrofulvalene
[6] R - bis(1,1-dimethyltridecyl)

Table 6.2 Specific heat of **1⇆2** molecular system from Fig. 6.3 compared to a sapphire control measurement with accepted values. Error bars are shown for a 90% confidence level.

Temperature [^{o}C]	Specific Heat [J/g-K] – ^{5}R-FvRu$_2$	Specific Heat [J/g-K] – Sapphire measured / (accepted)
25	1.15 ± 0.13	0.78 / (.78)
75	1.24 ± 0.15	0.85 / (.87)
125	1.33 ± 0.11	0.92 / (0.94)
175	1.42 ± 0.10	0.96 / (1.00)
225	1.52 ± 0.06	1.00 / (1.04)

6.2.2 Device Fabrication and Experimental Setup

As shown in Fig. 6.1, the MOST system is comprised primarily of the solar collector, catalytic converter, and a heat exchanger used to transfer the generated heat to a working fluid. Experiments here focus only on the solar collector and catalytic converter portion and the heat released is characterized by measuring the temperature rise. This experimental system can also serve as a platform for testing other candidate molecular systems for MOST applications.

Solar collector

The solar collector was made of borosilicate glass anodicaly bonded at 400 °C and voltage difference ΔV = 800 V to a silicon substrate that contained etched serpentine structured microchannels. Openings for the inlet and outlet to the microchannels were drilled prior to anodic bonding. The microchannels were constructed on a 150 mm diameter silicon wafer (p-type, 1–10 ohm cm, [100]) by using photolithography with a Karl Suss MA6 Mask Aligner. The exposed pattern was etched using a Surface Technology Systems (STS) DRIE etching tool. A depth of ~50 μm was ascertained by using an Alpha-Step IQ Surface Profiler. The silicon substrate and borosilicate glass were thoroughly cleaned in piranha solution (H_2SO_4-H_2O_2, 4:1) and dried, before they were bonded. The entire system was then placed on a 25×25 cm^2, 1 cm thick aluminum heat sink. A computer-numerical-control (CNC) mill was used to machine two circular grooves to accommodate chemical resistant Viton O-rings on two separate aluminum plates (1 cm × 5 cm × 25 cm). Holes were then drilled on the plates concentric to the O-ring grooves. These openings were then aligned with those on the borosilicate glass and secured by clamp to create an air tight seal. A syringe tip was inserted and fastened by chemically resistant epoxy. Finally, polytetrafluoroethylene (PTFE) tubes were used to connect the inlet of the microchannel to a WPI SP200i syringe pump containing compound **1** ([7]0.1 M in toluene), and the corresponding outlet to an inert Ar-flushed container. The total projected surface area of the microchannels was 585 mm^2. Irradiation employed a full spectrum solar simulator lamp from Newport Corp., equipped with an AM 1.5 and λ < 400 nm filters. Calibration to 1 sun intensity was made with a certified photovoltaic as a reference. The simulator was incorporated with the whole experimental setup as depicted in Fig. 6.5. A degassed solution of **1** was pumped through the apparatus and conversion to **2** monitored by ^{1}H NMR spectroscopy.[153]

[7] 0.1M concentration was used rather than the peak concentration of 0.4M because at smaller concentration the solution was far less viscous and easier to pump through the system.

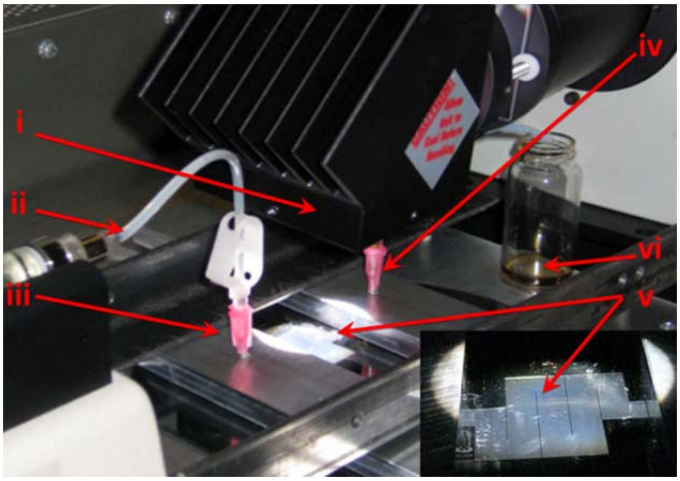

Fig. 6.5 Solar thermal energy conversion device: (i) AM 1.5 solar simulator incorporating a 400 nm cut-off filter, (ii) syringe pump to adjust flow rate, (iii) inlet port of solution, (iv) outlet port of solution, (v) microfluidic plates, (vi) collector of irradiated solution.

Heat Release Device

Catalytic reactor experiments utilized a PTFE tube inside a vacuum chamber ($P_{system} \approx 10^{-3}$ Pa, maintained via a Leybold Vacuum turbomolecular pump) designed to minimize convective and conductive heat losses (Fig. 6.6). A channel T-junction allowed for the insertion of thermocouples into the tube through one port, and the solution containing dissolved photoisomer **2** in THF through the other. The former consisted of two SLE Omega Engineering thermocouples placed just before and after the catalyst location and away from the chamber inlet and outlet. Cotton plugs prevented catalyst dislocation within the PTFE tube. This is more clearly illustrated in the diagram of Fig. 6.6. The chamber temperature was monitored by two additional thermocouples inside the vacuum chamber, whereas the system pressure was recorded by a pressure gauge. Additional PTFE tubes connected the catalytic reactor to the syringe pump at the inlet and to the collection flask at the outlet, respectively. The time dependent temperature rise was measured at increments of 1 s with an Omega HH147U Data Logger Thermometer (0.1 °C resolution) and recorded directly on a computer. Each experiment commenced by flushing the catalyst with toluene, followed by pumping the solution of **2** in tetrahydrofuran (THF) through the system.

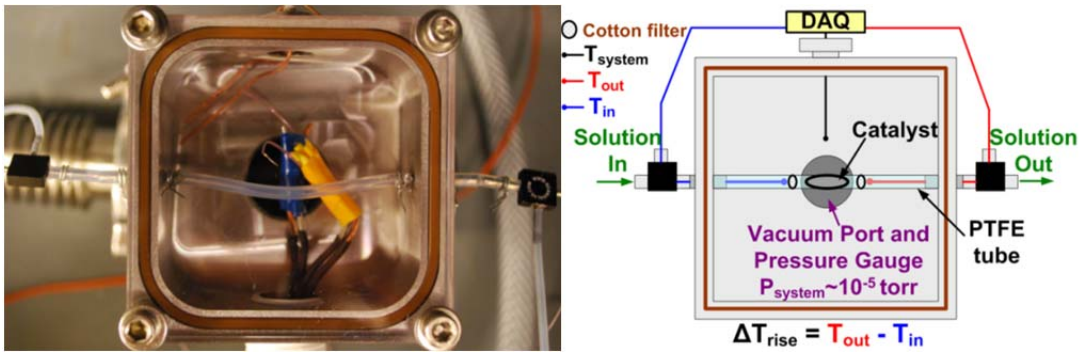

Fig. 6.6 Picture (left) of of the catalytic reaction chamber and a diagram (right) showing all the critical components; the temperature rise is measured at the inlet near the catalyst and at the outlet right after the solution passes the catalyst.

6.3 Results and Discussion

The goal of this system is to maximize the temperature rise during the thermal isomerization step to allow for direct solar thermal applications for heating or power generation via low temperature power generation systems.[105,154] An estimate of the expected temperature rise is given by Eq. (6.1),

$$\Delta T_{adiabatic} = \frac{m_{solu}\Delta H_{storage}}{(m_{solu}c_{solu} + m_{solv}c_{solv})} \tag{6.1}$$

in which $\Delta T_{\text{adiabatic}}$ is the total adiabatic temperature rise of the solution, $\Delta H_{\text{storage}}$ the total energy stored per kg of isomer, m_{solu} is the mass of the solute (photoisomer **2**), m_{solv} the mass of the solvent, c_{solu} the specific heat of the solute, and c_{solv} the specific heat of the solvent. As such, the presence of an inert solvent tends to dilute the temperature rise so the choice of the molecular system with which to test the device was predicated by the need to attain high concentration. The parent $FvRu_2(CO)_4$,[102] and its tetra-*tert*-butyl derivative,[103] were unsatisfactory in this regard.[106] Consequently, structure **1** in Fig. 6.3 was implemented, where the long-chain tertiary alkyl group was used to improve solubility.[153]

Energy Storage in the Microfluidic Solar Collector

Peak solubility of both isomers **1** and **2** is about 0.4 M (≈ 350 mg/mL) in common organic solvents such toluene and the measured $\Delta H_{\text{storage}}$ = 110.8 J/g yield a maximum temperature rise of approximately 23 °C when entered in Eq. (6.1) (See blue dashed line Fig. 6.7). Fig. 6.7 also illustrates the peak theoretical temperature rise at maximum solubility of the **1**⇆**2** system (red dashed line) if dichlorobenzene were implemented as the solvent. Although solubility in Dichlorobenzene was measured, this solution was not tested experimentally in this study due to its hazardous characteristics.

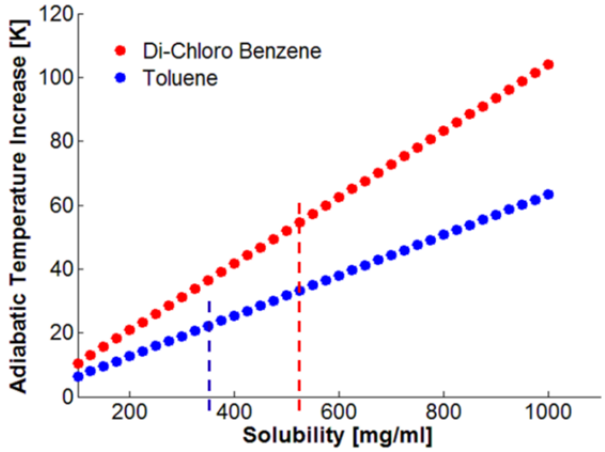

Fig. 6.7 Estimates of adiabatic temperature rise from conversion of **2** to **1** in solution. Peak solubilities in the two solvents are indicated by dashed lines.

The MOST solar collector (Fig. 6.5) consists of a micro-fluidic reactor in which the working fluid (**1** dissolved in toluene at molar concentration M = 0.1M = 100 mol/m^3) is pumped through the device while being illuminated by a solar simulator (1 sun, AM 1.5) to generate photoismer **2**. The irradiated microchannel area of 585 mm^2 was limited by the focus size of the solar simulator. By adjusting the flow rate $\dot{V}$ from 4 µL/min to 0.1 µL/min, and thus the

residence time in the reactor, conversions from 8 to 81% yield were achieved, respectively. It should be noted that these numbers are limited only by the residence time in the solar collector, as **1** transforms to **2** quantitatively in preparative experiments. By considering light out-put, residence time, concentration of **1**, and the conversion yield, the effective stored energy per unit area $\dot{e}$ could be determined using Eq. (6.2b)

$$\dot{M} = M \cdot \dot{V}$$

$$\dot{e} = \frac{\dot{M} \cdot \Delta \hat{H}_{storage}}{A} \qquad (6.2a, b),$$

where $\dot{M}$ is the molar conversion rate (mol/s) defined in Eq. (6.2a), $\Delta \hat{H}_{storage}$ the storage enthalpy per mol of compound **2** obtained from DSC experiments, and A the irradiated area. Energy storage rate data is ploted in Fig. 6.8 along with the mesasured conversion percentage of **1**→**2** as a function of residence time. As expected, the conversion rate plateaus as residence time is increased primarily because **1** is depleted and therefore the amount of absorbed light quanta per unit time is lowered. In addition, prolonged exposure appears to cause some degradation, as evidenced by the formation of a thin film on the glass plate, which, apart from draining some material, may block penetration of the incident light. The measured energy storage rate for low residence times (minimal thin film formation) is in good agreement with energy storage rate per unit area $\dot{e}_{calc}$ = 0.066 W/m^2 calculated from the heat flux at AM 1.5 conditions (~930 W/m^2) and photochrome efficiency $\eta_{pc} \approx 0.0071\%$ calculated from Eq. (5.4) (NOTE: η_{pc} is determined assuming $\eta_{abs} \approx 1$ and incorporating the measured quantum yield of photoisomerization of **1** → **2** at 400nm, $\Phi = 0.002$, see Ref. 154).

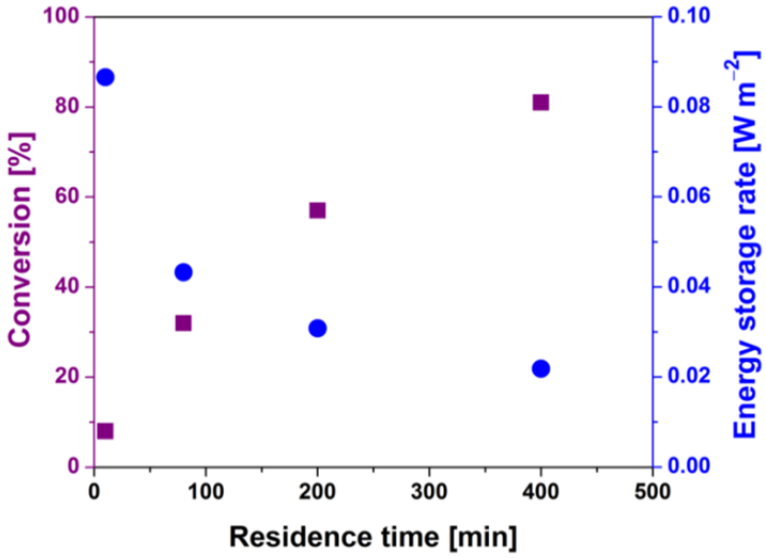

Fig. 6.8 Conversion of **1** (purple squares) to **2** as monitored by NMR, and energy storage characteristics (blue circles) as a function of residence time.

Heat Release in The Catalytic Reactor

The second complementary part of the system, needed to demonstrate that the energy stored in the active compound **2** can be effectively released by a triggered chemical back reaction. A number number of potential catalyst systems have been screened,[155] and it was

determined that 1–10 w% $AgNO_3$ on silica powder catalyzes the reaction of **2** to **1** dissolved in THF in quantitative yield in less than 1 min.[153,155] A limit of this catalytic system is the turnover number (TON) of only about 30, caused by catalyst (but not the silica substrate material) decomposition.

To quantify the experimental temperature rise, a reactor chamber has been developed with the schematic shown in Fig. 6.6. Here, a 0.1 M THF solution of compound **2** is pumped through a PTFE tube containing the catalyst (10 w% $AgNO_3$ on silica powder). Fig. 6.9 (left) depicts the measured temperature rise ΔT_{rise}. This demonstrates that flow through a heterogeneous catalyst is a feasible way of extracting the stored energy in a MOST system. The low TON of the catalyst limits the maximum observed temperature rise to approximately 0.9 °C, well below the theoretically predicted value from Eq. (6.1) of ~5.7 ^{o}C for the molar concentration used. Clean catalytic conversion of **2** to **1** as indicated by NMR measurements demonstrates that the catalytic conversion in high yield is feasible (up to 98%), and that even better heat release characteristics can be expected if a more stable and perennially active catalyst is implemented.

The stability of the photo-thermal cycle **1**⇆**2** has been tested and indicates that the system is extremely durable up to 10 cycles with no or little degradation.[153] When considering large scale applications, recyclability of **1** and **2** through thousands of cycles is important. However, this optimization is not considered here, and it is noted that studies of other MOST candidate systems have shown that several thousand cycles can be achieved with minor degradation.[99]

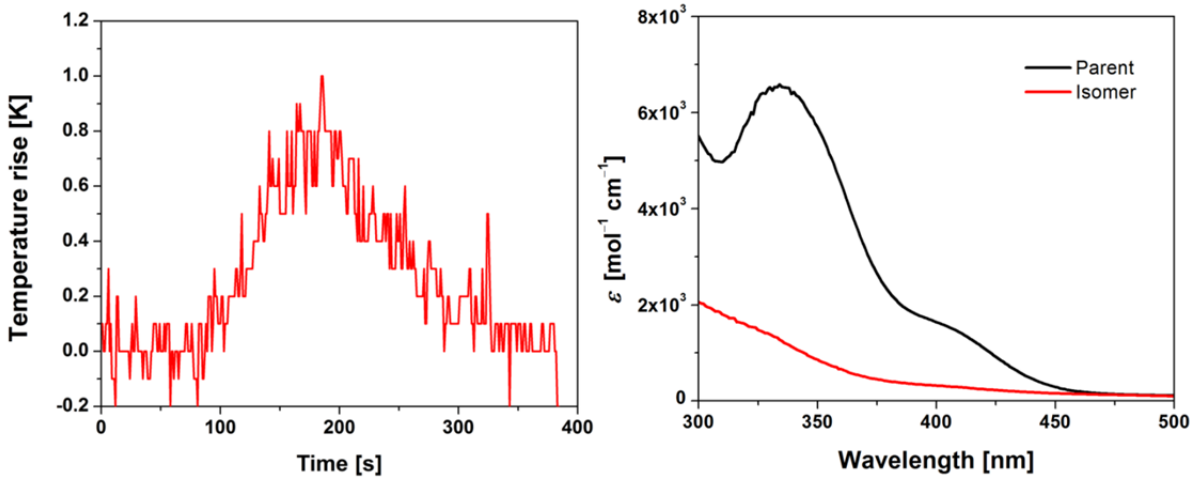

Fig. 6.9 (left) Measured temperature rise for **2** dissolved in THF (0.14 M), at a flow rate of ~2.78 µl/s, through the catalyst (28 mg of 10 w% $AgNO_3$ on silica powder). The error bar is ± 0.1 K for the data shown; (right) Absorption spectra of **1** (parent) and **2** (isomer) from Fig. 6.3 included with permission from Ref. [153].

MOST System Round Trip Efficiency

Putting into perspective the characteristics of the MOST system probed here, the energy density at peak solubility is ~10.7 Wh/L. This is an orders of magnitude improvement to the original $FvRu_2$ compounds,[102,106] and going in the right direction toward energy densities of solar thermal materials summarized in Table 1.1,, Li-ion batteries,[13] and those in recently proposed azobenzene systems.[156] However, when very low energy conversion rates are considered as presented in Fig. 6.8, clever design is necessary for practical applications. For

example, the mismatch between the rates of solar energy storage **1→2** and catalytic heat release **2→1** can be mitigated by proper MOST system design; **1→2** can be done in large storage tanks taking advantage of quantitative volumetric conversion in solution (see Fig. 6.2). Other important metrics of MOST systems to consider are the round trip efficiency and the number of cycles sustained before significan degradation occurs. Considering the former, with high catalytic conversion yield observed experimentally ($\eta_{cat} \approx 98\%$), absorption characteristics of **1** and **2** shown in Fig. 6.10 (right), and assuming minor degradation, the full cycle efficiency of **1⇆2** as defined by Eq. (5.5) (excluding losses via heat exchange) is ~0.0071%

In view of the modifications implemented in systems such as norbornadiene-quadricyclane,[23,91,96–99] the efficiency of **1→2,** and thus the round trip efficiency and overall photoconversion rate, can analogously be improved by use of sensitizers, and additional substituents that would modify the absorption spectrum and quantum yield of the reaction. Under these premises, the estimate for the peak round trip efficiency of **1⇆2** of up to 8.8% which is comparable to the estimated peak efficiencies of photosynthesis-biomass processes.[157] In this assumption it is estimated that the quantum yield Φ~0.95 and the range of wavelengths over which **1** absorbs and **2** is not sensitive is 280–550 nm.

6.4 Summary

In summary, a full cycle MOST energy storage and release system has been demonstrated which can also serve as a device for testing other candidate molecular compounds. It consists of a $FvRu_2$ based working fluid, a microfluidic solar collector, and a catalytic heat release reactor. The high solubility of the newly synthesized **1** provides a relatively large energy storage density in the working fluid and the catalytic energy release reaction is rapid which are two important factors for device implementation. The organometallic $FvRu_2$ based system satisfies several criteria presented in Chapter 5.2 (in particular a, b, e and g) The kinetic stability of **2** and the resilience of the **1⇆2** cycle are promising characteristics that encourage further improvements of the framework. Temperature rise is currently limited by catalyst performance, suggesting that in addition to optimization of the parent molecule for light absorption features, further catalyst development is necessary. Moreover, from an economical perspective, ruthenium based compounds are far from ideal due to scarcity and high cost of this metal, thus development of photosensitive organometallic compounds based on abundant metals such as iron is highly desirable. The availability of a MOST device will facilitate the screening for alternative molecular systems and catalysts, in an effort develop a durable and economically sound system. All findings presented here may inspire other work focused on developing analogous MOST solar energy conversion and storage systems based on organometallic compounds that may achieve large scale energy conversion applications.

The preceding chapter first appeared in *Energy Environ. Sci, Vol. 5, 8534 - 8537, (2012)*

Title: Molecular solar thermal (MOST) energy storage and release system

Authors: Kasper-Moth Poulsen,* Dusan Coso,* Karl Börjesson, Nikolai Vinokurov, Steven K. Meier, Arun Majumdar, K. Peter C. Vollhardt and Rachel A. Segalman

*denotes equal contribution

7. Conclusions and Future Outlook

7.1 Conclusions

The scope of this dissertation covered two topics which are related through a similar physical mechanism – phase change via state transitions in solid-liquid-vapor systems and molecular (chemical) structure transitions.

In Chapters 3 and 4, phase change heat transfer in micro and micro/nano structured silicon surfaces is studied in both pool boiling and thin liquid film wick structure experiments. This investigation was motivated based on thermal management needs where passive components such as heat pipes, vapor chamber thermal spreaders, and immersion cooling systems are implemented, and the objective was to engineer structures that yield better heat transfer and get a better understanding of what limits performance on finite size surfaces through a comparative study. Unique measurement setups and procedures were developed that fairly accurately account for heat losses encountered in these types of measurements.

In Chapter 3, evaporation/boiling phase change heat transfer was investigated through a systematic study of biporous microscale pin fin array capillary wick structures. The focus was on developing a better performing evaporator wick via increase of thin liquid film area coverage at the menisci formed between the pins. Based on this hypothesis structures were generated capable of dissipating up to 277.0 (± 9.7) W/cm^2, both, via evaporation and nucleate boiling modes of phase change heat transfer. In addition, these micropillar arrays indicated good performance in thermal management of local hot spots where heat fluxes of up to 733.1 (± 103.4) W/cm^2 could be dissipated over an area of ~0.0625 cm^2. The systematic study also yielded several interesting results. Deeper wick structures demonstrated both evaporative and boiling heat transfer, while shallower wicks reached CHF before nucleate boiling was clearly observed. These observations were verified visually and by changes in the slope of the q vs. ΔT data. In addition, in shallower structures, heat transfer coefficient (HTC) via evaporation could be further enhanced by reducing pore size and thus increasing area coverage of thin film menisci that form at the contact line. However, at really small pore sizes ($p \sim 4\mu m$) a reduction of HTC performance is observed and attributed to evaporation suppression due to the curvature in the menisci.

In pool boiling experiments discussed in Chapter 4, the aim was to investigate the limiting phenomena of CHF on finite size heaters (applications in immersion cooling of microelectronic systems) and generate surfaces capable of dissipating high heat fluxes and generating high HTCs in order to allow for smaller operating temperatures. The former is done through a comparative study of biporous micropillar wicks in both pool boiling and thin film experiments via visualization studies, and developing some scaling analyses based on experimental data and sample parameters. Visual observations indicate that the bubble interactions near the heater surface generate larger secondary bubbles that hinder ebullition in pool boiling experiments. Comparison to thin liquid film experiments on structures with same geometries indicate that a similar fraction of the porous volume is active in the phase change process (comparable HTCs), but that bubble ebullition in the capillary wicking experiments is not hindered above the wick surface thus allowing for higher CHF to be reached limited by capillary rewetting. This observation suggests that momentum driven lateral bubble expansion along the heater surface may not be as significant to limiting CHF for some pool boiling surface morphologies of finite size as are hydrodynamic phenomena near and away from the heater

surface. For well wetted finite size microstructured surfaces the pool boiling CHF is found to be hydrodynamically limited by instabilities modulated by heater size. No benefit was found in reducing pore size and thus increasing capillary pressure in order to enhance CHF. Peak HTC's and CHF of 10.59 ± 0.68 W/cm^2-K and 151.76 ± 2.25 respectively W/cm^2 were measured on ~178 μm deep biporous micropillar surfaces. HTC increased via surface area enhancement; this was atributed to the larger surface area available for heat transfer within the porous medium, and variation of wettability presumed within the pores that promotes bubble nucleation as compared to that observed on the whole heater surface via the apparent contact angle that reduced as micropillar surface area increased.

In the latter investigation of Chapter 4, a nanowire array surface was combined with microscale cavities in order to generate a structure with high CHF and HTC. No benefit of using reentrant cavities was observed since rectangular cavities yielded almost identical performance. Smaller (d_c = 11 μm) size cavities were more efficient in bubble nucleation and yielded higher HTC at same heat fluxes when compared to larger cavities (d_c = 41μm) dispersed in identical arrays on nanowire surfaces (~100 μm and ~800 μm 2-D square lattice). The maximum observed HTC of 6.4 ± 0.32 W/cm^2-K for these cavities was achieved at $q \approx$ 115W/cm^2 for a hybrid cavity/nanowire surface at peak cavity density (d_c = 11 μm, s_c = 100μm) – a ~2.4 fold increase in HTC compared to cavity free nanowire surface. The presence of cavities reduced the superheat of bubble nucleation onset significantly, increased thermal stability of the substrate, but did not seem to affect the CHF as compared to a plain nanowire surface; on these well wetting finite surfaces CHF also seems to be limited by heater size modulated hydrodynamics.

The final portion of this dissertation presented in Chapter 6 focused on organometallic molecules that store solar energy via a reversible phase-change-like reorientation of chemical structure. These molecular systems have shown great durability and are probed via a newly developed microfluidic system that tests both energy storage and release characteristics. The MOST device can be used in the future for testing and optimizing other potential molecular candidates. These experiments indicated that 110 J/g can be stored in bis(1,1-dimethyltridecyl) substituted $FvRu_2$ system. The photochrome efficiency was determined to be η_{pc} = 0.0073% and the measured temperature rise via a 10 w% $AgNO_3$ on silica powder heterogeneous catalyst was 0.9 ^oC, much lower than theoretical predictions and limited by the catalyst turnover number. Even though the current system demonstrates poor performance, it suggests an avenue for research in solar energy storage in photosensitive organometallic molecular systems, which can be probed and optimized more easily with a microfluidic system developed here.

7.2 Further Wick Structure Optimization and Fundamental Studies of Bursting Phenomenon

As it was evident in Chapter 3, biporous microscale pin fin array structures demonstrated great phase change heat transfer characteristics but some questions remain unanswered, and there are other avenues that can be followed inspired by this work. For instance, incorporating a micropillar structure developed here in a fully operational heat pipe, and optimizing it with respect to porosity, pore size, depth and other parameters can be the ultimate engineering test to determining true performance characteristics and whether the bursting phenomenon that occurs at high heat fluxes is detrimental to operation. On a more fundamental side, temperature measurements using very sensitive tools (thermocouples, data acquisition units, etc.) with better temporal and spatial resolution can be incorporated to better understand the frequency domain of these bursting cycles and the temperature responses over finite surfaces. The experimental

system incorporated in this study captures visual data on the order of 4 ms, and thermal data on the order of 25-100 ms which is not enough to capture and understand the temperature transients caused by the boiling heat transfer and get accurate bursting frequencies indicated in the visualization studies. This data could also provide valuable information on the capability of this boiling mechanism for cooling hot spots of various sizes. In addition, if implemented in pool boiling experiments as well, a more thorough investigation of bubble sizes, release frequencies and interactions within and near the porous medium can be studied. Automation of the experimental setup can allow for synchronization of visual, temporal and thermal data.

7.3 Alternative Pathways for Enhancing HTC and Circumventing Hydrodynamic Limitations

Based on the pool boiling heat transfer characteristics observed on hybrid micro/nano surfaces, and the indications that smaller cavities are actually more efficient at bubble nucleation and release over length scales where bubble interactions are significant, it would be interesting to take a more fundamental approach and study how the contact line region generated by the nanowires at the cavity mouth affects nucleation. It is well known that cavities are capable of trapping gases and vapors and thus being active nucleation sites, but can a nano scale roughness or nano porous regions near a micro scale cavity opening make cavities of any shape permanent nucleation sites irrespective of geometry? Based on the findings of this investigation, it may be interesting to develop hierarchical micro/nano scale structures incorporating cavities, nanowires, micro pillars etc., for selective thermal management of more localized heat sources incorporating best characteristics of each structure type. Attempting these experiments on large heaters ($L >> L_c$) may also help better isolate limiting phenomena.

Based on hydrodynamic theory which generally imposes stringent limits on CHF and is so often encountered in investigated systems throughout literature, the idea that hydrodynamics can be modulated proposed in previous works, also appears to be a possible avenue for future work. In this study, biporous structures yielded no modulations; however, engineering porous surfaces with features of multiple length scales that extend in the out-of-plane dimension to be on the order of capillary length L_c may serve to better guide relative liquid and vapor flows that are responsible for the hydrodynamic instabilities, and in that way delay CHF.

Finally, research on the topic of pool boiling would greatly benefit from establishment of standardized measurement systems. In recent years, enhancements in pool boiling CHF have only somewhat exceeded limits suggested by hydrodynamic theories. Having standardized measurements would significantly improve understanding of data trends, allow for better comparison of various surface types, and establish a better foundation for theoretical models.

7.4 Exploring Methods for Improving Solar Energy Storage and Conversion Characteristics in MOST Systems

In the case of the MOST solar energy conversion it would be interesting to collaborate with synthetic chemists and develop and test other organometallic photosensitive molecules based on more abundant materials than ruthenium. The MOST system could be further optimized and implemented in screening of other catalysts. Testing the durability of $FvRu_2$ based and other candidate molecules that store solar energy reversibly should be a priority. Ultimately the goal should be to develop a system capable of effective solar energy storage and direct solar energy conversion to work. Focus should be directed to synthesis of MOST system based on cheaper materials, and cost analysis studies should be conducted to determine best applications.

References

[1] International Energy Agency, 2010, World Energy Outlook, IEA Publications.

[2] Baxter J., Bian Z., Chen G., Danielson D., Dresselhaus M. S., Fedorov A. G., Fisher T. S., Jones C. W., Maginn E., Kortshagen U., Manthiram A., Nozik A., Rolison D. R., Sands T., Shi L., Sholl D., and Wu Y., 2009, "Nanoscale Design to Enable the Revolution in Renewable Energy," Energy & Environmental Science, **2**(6), p. 559.

[3] REN21, 2011, Renewables 2011 Global Status Report, Paris: REN21 Secretariat.

[4] Faghri A., 1995, Heat Pipe Science and Technology, Taylor & Francis, Washington DC.

[5] Vasiliev L. L., 2005, "Heat Pipes in Modern Heat Exchangers," Applied Thermal Engineering, **25**(1), pp. 1–19.

[6] Mahajan R., and Chrysler G., 2006, "Cooling a Microprocessor Chip," Proceedings of the IEEE, **94**(8), pp. 1476–1486.

[7] Sobhan C. B., Rag R. L., and Peterson G. P., 2007, "A Review and Comparative Study of the Investigations on Micro Heat Pipes," International Journal of Energy Research, **31**, pp. 664–688.

[8] Garimella S. V, Fleischer A. S., Murthy J. Y., Keshavarzi A., Prasher R., Member S., Patel C., Bhavnani S. H., Venkatasubramanian R., Mahajan R., Joshi Y., Sammakia B., Myers B. A., Chorosinski L., Baelmans M., Sathyamurthy P., and Raad P. E., 2008, "Thermal Challenges in Next-Generation Electronic Systems," **31**(4), pp. 801–815.

[9] Mudawar I., 2001, "Assessment of High-Heat-Flux Thermal Management Schemes," IEEE Transactions on Components and Packaging Technologies, **24**(2), pp. 122–141.

[10] Hasnain S. M., 1998, "Review on Sustainable thermal Energy Storage Technologies, Part I: Heat Storage Materials and Techniques," Energy Conversion and Management, **39**(11), pp. 1127–1138.

[11] Sharma S. D., and Sagara K., 2005, "Latent Heat Storage Materials and Systems: A Review," International Journal of Green Energy, **2**(1), pp. 1–56.

[12] Sharma A., Tyagi V. V., Chen C. R., and Buddhi D., 2009, "Review on Thermal Energy Storage with Phase Change Materials and Applications," Renewable and Sustainable Energy Reviews, **13**(2), pp. 318–345.

[13] Cook T. R., Dogutan D. K., Reece S. Y., Surendranath Y., Teets T. S., and Nocera D. G., 2010, "Solar Energy Supply and Storage for the Legacy and Nonlegacy Worlds," Chemical Reviews, **110**(11), pp. 6474–502.

[14] Gur I., Sawyer K., and Prasher R., 2012, "Searching for a Better Thermal Battery," Science (New York, N.Y.), **335**(6075), pp. 1454–5.

[15] Watel B., 2003, "Review of Saturated Flow Boiling in Small Passages of Compact Heat-Exchangers," International Journal of Thermal Sciences, **42**(2), pp. 107–140.

[16] Schrage R. W., 1953, A Theoretical Study of Interphase Mass Transfer, Columbia University Press, New York, NY.

[17] Carey V. P., 2008, Liquid-Vapor Phase-Change Phenomena, Taylor & Francis, New York, NY.

[18] U.S. Energy Information Administration, 2011, Annual Energy Review 2011, Washington DC.

[19] Chen H., Cong T. N., Yang W., Tan C., Li Y., and Ding Y., 2009, "Progress in Electrical Energy Storage System: A Critical Review," Progress in Natural Science, **19**(3), pp. 291–312.

[20] Kalogirou S. a., 2004, "Solar Thermal Collectors and Applications," Progress in Energy and Combustion Science, **30**(3), pp. 231–295.

[21] Dürr H., and Boas-Laurent H., eds., 2003, Photochromism Molecules and Systems, Elsevier, Amsterdam.

[22] Scharf H.-D., Fleischhauer J., Leismann H., Ressler I., Schleker W., and Weitz R., 1979, "Criteria for the Efficiency, Stability, and Capacity of Abiotic Photo-chemical Solar Energy Storage Systems," Angewandte Chemie (International ed. in English), **18**, pp. 652–662.

[23] Bren' V. A., Dubonosov A. D., Minkin V. I., and Chernoivanov V. A., 1991, "Norbornadiene–Quadricyclane — an Effective Molecular System for the Storage of Solar Energy," Russian Chemical Reviews, **60**(5), pp. 451–469.

[24] Ross R. T., and Hsiao T., 1977, "Limits on the Yield of Photochemical Solar Energy Conversiona," Journal of Applied Physics, **48**(11), pp. 4783–4785.

[25] Almgren M., 1978, "Thermodynamic and Kinetic Limitations on the Conversion of Solar Energy Into Storable Chemical Free-Energy," Photochemistry and Photobiology, **27**(5), pp. 603–609.

[26] Moore G. E., and Fellow L., 1998, "Cramming More Components onto Integrated Circuits," Proceedings of the IEEE, **86**(1), pp. 82–85.

[27] Geer D., 2005, "Chip Makers Turn to Multicore Processors," Computer, **38**(5), pp. 11–13.

[28] Majumdar A., 2009, "Helping Chips to Keep their Cool," Nature Nanotechnology, **4**, pp. 214–215.

[29] Prasher R. S., 2003, "A Simplified Conduction Based Modeling Scheme for Design Sensitivity Study of Thermal Solution Utilizing Heat Pipe and Vapor Chamber Technology," Journal of Electronic Packaging, **125**(3), p. 378.

[30] Potash M., and Wayner P. C., 1972, "Evaporation From a Two-Dimensional Extended Meniscus," International Journal of Heat and Mass Transfer, **15**, pp. 1851–1863.

[31] Wayner P. C., 1991, "The Effect of Interfacial Mass Transport on Flow in Thin Liquid Films," Colloids and Surfaces, **52**, pp. 71–84.

[32] DasGupta S., Schonberg J. A., Kim I. Y., and Wayner P. C. J., 1993, "Use of the Augmented Young-Laplace Equation to Model Equilibrium and Evaporating Extended Menisci," Journal of Colloid and Interface Science, **157**, pp. 332–342.

[33] Wayner P. C., 1999, "Intermolecular Forces in Phase-Change Heat Transfer: 1998 Kern Award Review," AIChE Journal, **45**(10), pp. 2055–2068.

[34] Schonberg J. a., DasGupta S., and Wayner P. C., 1995, "An Augmented Young-Laplace Model of an Evaporating Meniscus in a Microchannel with High Heat Flux," Experimental Thermal and Fluid Science, **10**(2), pp. 163–170.

[35] Stephan P. C., and Busse C. A., 1992, "Analysis of the Heat Transfer Coefficient of Grooved Heat Pipe Evaporator Walls," International Journal of Heat and Mass Transfer, **35**(2), pp. 383–391.

[36] Xu X., and Carey V. P., 1990, "Film Evaporation from a Micro-Grooved Surface — An Approximate Heat Transfer Model and Its Comparison with Experimental Data," Journal of Thermophysics, **4**(4), pp. 512–520.

[37] Sujanani M., and Wayner P. C., 1992, "Transport Processes and Interfacial Phenomena in an Evaporating Meniscus," Chemical Engineering Communications, **118**(1), pp. 89–110.

[38] Panchamgam S. S., Gokhale S. J., Plawsky J. L., DasGupta S., and Wayner P. C., 2005, "Experimental Determination of the Effect of Disjoining Pressure on Shear in the Contact Line Region of a Moving Evaporating Thin Film," Journal of Heat Transfer, **127**(3), p. 231.

[39] Wang H., Garimella S. V., and Murthy J. Y., 2007, "Characteristics of an Evaporating Thin Film in a Microchannel," International Journal of Heat and Mass Transfer, **50**, pp. 3933–3942.

[40] Dhavaleswarapu H. K., Garimella S. V., and Murthy J. Y., 2009, "Microscale Temperature Measurements Near the Triple Line of an Evaporating Thin Liquid Film," Journal of Heat Transfer, **131**(6), p. 061501.

[41] Panchamgam S. S., Plawsky J. L., and Wayner P. C., 2006, "Spreading Characteristics and Microscale Evaporative Heat Transfer in an Ultrathin Film Containing a Binary Mixture," Journal of Heat Transfer, **128**(12), p. 1266.

[42] Panchamgam S. ., Chatterjee A., Plawsky J. L., and Wayner P. C. J., 2008, "Comprehensive Experimental and Theoretical Study of Fluid Fow and Heat Transfer in a Microscopic Evaporating Meniscus in a Miniature Heat Exchanger," International Journal of Heat and Mass Transfer, **51**, pp. 5368–5379.

[43] Morris S. J. S., 2003, "The Evaporating Meniscus in a Channel," Journal of Fluid Mechanics, **494**, pp. 297–317.

[44] Ma H. Bin, and Peterson G. P., 1996, "Experimental Investigation of the Maximum Heat Transport in Triangular Grooves," Journal of Heat Transfer, **118**, pp. 740–746.

[45] Ma H. B., Lofgreen K. P., and Peterson G. P., 2006, "An Experimental Investigation of a High Flux Heat Pipe Heat Sink," Journal of Electronic Packaging, **128**(1), p. 18.

[46] Zhao Y., and Chen C., 2007, "Vaporization Heat Transfer in Sintered Copper Wicks with Microgrooves," THERMES 2007: Thermal Challanges in Next Generation Electronic Systems, Millpress, Rotterdam, pp. 241–247.

[47] Lips S., Lefèvre F., and Bonjour J., 2009, "Nucleate Boiling in a Flat Grooved Heat Pipe," International Journal of Thermal Sciences, **48**(7), pp. 1273–1278.

[48] Weibel J. a., Garimella S. V., and North M. T., 2010, "Characterization of Evaporation and Boiling from Sintered Powder Wicks Fed by Capillary Action," International Journal of Heat and Mass Transfer, **53**, pp. 4204–4215.

[49] Cai Q., and Chen C.-L., 2010, "Design and Test of Carbon Nanotube Biwick Structure for High-Heat-Flux Phase Change Heat Transfer," Journal of Heat Transfer, **132**(5).

[50] Dunn P. D., and Reay D. A., 1976, Heat Pipes, Pergamon Press, Elmsford.

[51] Hanlon M. a., and Ma H. B., 2003, "Evaporation Heat Transfer in Sintered Porous Media," Journal of Heat Transfer, **125**(4), p. 644.

[52] Li C., Peterson G. P., and Wang Y., 2006, "Evaporation/Boiling in Thin Capillary Wicks (l)—Wick Thickness Effects," Journal of Heat Transfer, **128**(12), p. 1312.

[53] Li C., and Peterson G. P., 2006, "Evaporation/Boiling in Thin Capillary Wicks (II)—Effects of Volumetric Porosity and Mesh Size," Journal of Heat Transfer, **128**(12), p. 1320.

[54] Liao Q., and Zhao T. S., 1999, "Evaporative Heat Transfer in a Capillary Structure Heated by a Grooved Block," AIAA Journal of Thermophysics and Heat Transfer, **13**(1), pp. 126–133.

[55] Davis T. W., and Garimella S. V., 2008, "Thermal Resistance Measurement Across a Wick Structure Using a Novel Thermosyphon Test Chamber," Experimental Heat Transfer, **21**(2), pp. 143–154.

[56] Semenic T., Lin Y. Y., Catton I., and Sarraf D. B., 2008, "Use of Biporous Wicks to Remove High Heat Fluxes," Applied Thermal Engineering, **28**(4), pp. 278–283.

[57] Semenic T., Lin Y.-Y., and Catton I., 2008, "Thermophysical Properties of Biporous Heat Pipe Evaporators," Journal of Heat Transfer, **130**(2).

[58] Semenic T., and Catton I., 2009, "Experimental Study of Biporous Wicks for High Heat Flux Applications," International Journal of Heat and Mass Transfer, **52**(21-22), pp. 5113–5121.

[59] Cao X. L., Cheng P., and Zhao T. S., 2002, "Experimental Study of Evaporative Heat Transfer in Sintered Copper Bidispersed Wick Structures," Journal of Thermophysics and Heat Transfer, **16**(4), pp. 547–552.

[60] Zuber N., 1959, "Hydrodynamic Aspects of Boiling Heat Transfer," University of California Los Angeles.

[61] Lienhard J. H., and Dhir V. K., 1973, "Extended Hydrodynamic Theory of the Peak and Minimum Pool Boiling Heat Fluxes," NASA-CR2270.

[62] Gogonin I. I., and Kutateladze S. S., 1977, "Critical Heat Flux as a Function of Heater Size for a Liquid Boiling in a Large Enclosure," Inzhenerno-Fizicheskii Zhurnal, **33**(5), pp. 1286–1289.

[63] Kandlikar S. G., 2001, "A Theoretical Model to Predict Pool Boiling CHF Incorporating Effects of Contact Angle and Orientation," Journal of Heat Transfer, **123**(6), p. 1071.

[64] Dhir V. K., and Liaw S. P., 1989, "Framework for a Unified Model for Nucleate and Transition Pool Boiling," **111**, pp. 739–746.

[65] Theofanous T. G., Tu J. P., Dinh A. T., and Dinh T. N., 2002, "The Boiling Crisis Phenomenon Part I : Nucleation and Nucleate Boiling Heat Transfer," **26**, pp. 775–792.

[66] Theofanous T. G., Dinh T. N., Tu J. P., and Dinh A. T., 2002, "The Boiling Crisis Phenomenon Part II : Dryout Dynamics and Burnout," **26**, pp. 793–810.

[67] Dhir V. K., 1998, "Boiling Heat Transfer," Annual Review of Fluid Mechanics, **30**(1), pp. 365–401.

[68] Wang C. H., and Dhir V. K., 1993, "Effect of Surface Wettability on Active Nucleation Site Density During Pool Boiling of Water on a Vertical Surface," Journal of Heat Transfer, **115**, pp. 659–669.

[69] Kim S. J., Bang I. C., Buongiorno J., and Hu L. W., 2007, "Surface Wettability Change During Pool Boiling of Nanofluids and its Effect on Critical Heat Flux," International Journal of Heat and Mass Transfer, **50**, pp. 4105–4116.

[70] Kim S. J., Bang I. C., Buongiorno J., and Hu L. W., 2007, "Study of Pool Boiling and Critical Heat Flux Enhancement in Nanofluids," Bulletin of the Polish Academy of Sciences, **55**(2), pp. 211–216.

[71] Kim H., Kim J., and Kim M. H., 2006, "Effect of Nanoparticles on CHF Enhancement in Pool Boiling of Nano-fluids," International Journal of Heat and Mass Transfer, **49**(25-26), pp. 5070–5074.

[72] Ahn H. S., Lee C., Kim H., Jo H., Kang S., Kim J., Shin J., and Kim M. H., 2010, "Pool Boiling CHF Enhancement by Micro/Nanoscale Modification of Zircaloy-4 Surface," Nuclear Engineering and Design, **240**(10), pp. 3350–3360.

[73] Ahn H. S., Jo H. J., Kang S. H., and Kim M. H., 2011, "Effect of Liquid Spreading Due to Nano/Microstructures on the Critical Heat Flux During Pool Boiling," Applied Physics Letters, **98**(7).

[74] Ahn H. S., Lee C., Kim J., and Kim M. H., 2012, "The Effect of Capillary Wicking Action of Micro/Nano Structures on Pool Boiling Critical Heat Flux," International Journal of Heat and Mass Transfer, **55**, pp. 89–92.

[75] Honda H., Takamastu H., and Wei J. J., 2002, "Enhanced Boiling of FC-72 on Silicon Chips With Micro-Pin-Fins and Submicron-Scale Roughness," Journal of Heat Transfer, **124**(2), p. 383.

[76] Wei J. J., and Honda H., 2003, "Effects of in Geometry on Boiling Heat Transfer from Silicon Chips with Pin Fins," International Journal of Heat and Mass Transfer, **46**, pp. 4059–4070.

[77] Li C., and Peterson G. P., 2007, "Parametric Study of Pool Boiling on Horizontal Highly Conductive Microporous Coated Surfaces," Journal of Heat Transfer, **129**(11), p. 1465.

[78] Chen R., Lu M.-C., Srinivasan V., Wang Z., Cho H. H., and Majumdar A., 2009, "Nanowires for Enhanced Boiling Heat Transfer," Nano letters, **9**(2), pp. 548–53.

[79] Lu M.-C., Chen R., Srinivasan V., Carey V. P., and Majumdar A., 2011, "Critical Heat Flux of Pool Boiling on Si Nanowire Array-Coated Surfaces," International Journal of Heat and Mass Transfer, **54**, pp. 5359–5367.

[80] Li C., Wang Z., Wang P.-I., Peles Y., Koratkar N., and Peterson G. P., 2008, "Nanostructured Copper Interfaces for Enhanced Boiling," Small (Weinheim an der Bergstrasse, Germany), **4**(8), pp. 1084–8.

[81] Chu S., and Majumdar A., 2012, "Opportunities and Challenges for a Sustainable Energy Future," Nature, **488**, pp. 294–303.

[82] Shah A., Torres P., Tscharner R., Wyrsch N., and Keppner H., 1999, "Photovoltaic Technology: The Case for Thin-Film Solar Cells," Science, **285**, pp. 692–698.

[83] Goetzberger A., Hebling C., and Schock H.-W., 2003, "Photovoltaic Materials, History, Status and Outlook," Materials Science and Engineering: R: Reports, **40**(1), pp. 1–46.

[84] Herrmann U., and Kearney D. W., 2002, "Survey of Thermal Energy Storage for Parabolic Trough Power Plants," Journal of Solar Energy Engineering, **124**(2), p. 145.

[85] Farid M. M., Khudhair A. M., Razack S. A. K., and Al-Hallaj S., 2004, "A Review on Phase Change Energy Storage: Materials and Applications," Energy Conversion and Management, **45**, pp. 1597–1615.

[86] Schnatbaum L., 2009, "Solar Thermal Power Plants," The European Physical Journal Special Topics, **176**(1), pp. 127–140.

[87] Kenisarin M. M., 2010, "High-Temperature Phase Change Materials for Thermal Energy Storage," Renewable and Sustainable Energy Reviews, **14**(3), pp. 955–970.

[88] Kucharski T. J., Tian Y., Akbulatov S., and Boulatov R., 2011, "Chemical Solutions for the Closed-Cycle Storage of Solar Energy," Energy & Environmental Science, **4**(11), pp. 4449–4472.

[89] Tchanche B. F., Lambrinos G., Frangoudakis A., and Papadakis G., 2011, "Low-grade Heat Conversion into Power Using Organic Rankine Cycles – A Review of Various Applications," Renewable and Sustainable Energy Reviews, **15**(8), pp. 3963–3979.

[90] Wentworth W. E., and Chen E., 1976, "Simple Thermal Decomposition Reactions for Storage of Solar Thermal Energy," Solar Energy, **18**(3), pp. 205–214.

[91] Yoshida Z.-I., 1985, "New Molecular Energy Storage Systems," Journal of Photochemistry, **29**, pp. 27–40.

[92] Hall H. K. J., Smith C. D., and Baldt J. H., 1973, “Enthalpies of Formation of Nortricyclene, Norbornene, Norbornadiene, and Quadricyclane,” Journal of the American Chemical Society, **95**(10), pp. 3197–3201.

[93] Kabakoff D. S., Bunzli J. G., Oth J. F. M., Hammond W. B., and Bersonzb J. A., 1975, “Enthalpy and Kinetics of Isomerization of Quadricyclane to Norbornadiene. Strain Energy of Quadricyclane,” Journal of the American Chemical Society, **97**(6), pp. 1510–1512.

[94] Maruyama K., Terada K., and Yamamoto Y., 1981, “Exploitation of Solar Energy Storage Systems . Valence Isomerization between Norbornadiene and Quadricyclane Derivatives,” journal of organic chemistry, **46**, pp. 5294–5300.

[95] Raghavachari K., Haddon R. C., and Roth H. D., 1983, “Theoretical Studies in the Norbornadiene-Quadricyclane System,” Journal of the American Chemical Society, **105**, pp. 3110–3114.

[96] Dubonosov A. D., Bren V. A., and Chernoivanov V. A., 2002, “Norbornadiene–Quadricyclane as an Abiotic System for the Storage of Solar Energy,” Russian Chemical Reviews, **71**(11), pp. 917–927.

[97] Phlllppopoulos C., Economou D., Economou C., and Marangoris J., 1983, “Norbornadiene-Quadricyclane System in the Photochemical Conversion and Storage of Solar Energy,” American Chemical Society, **22**, pp. 627–633.

[98] Philippopoulos C., and Marangozis J., 1984, “Kinetics and Efficiency of Solar Energy Storage in the Photochemical Isomerization of Norbornadlene to Quadricyclane,” American Chemical Society, **23**, pp. 458–466.

[99] Miki S., Yoshida A., and Yoshida Z.-I., 1987, “Photochromic Films Prepared by Doping with Donor-Acceptor Norbornadienes,” Chemistry Letters - Chemical Society of Japan, pp. 195–198.

[100] Bolton J., 1978, “Solar Fuels,” Science, **202**, pp. 705–711.

[101] Archer M. D., and Bolton J. R., 1990, “Requirements for Ideal Performance of Photochemical and Photovoltaic Solar Energy Converters,” American Chemical Society, **94**, pp. 8028–8036.

[102] Boese R., Cammack J. K., Matzger A. J., Pflug K., Tolman W. B., Vollhardt K. P. C., and Weidman T. W., 1997, “Photochemistry of (Fulvalene)tetracarbonyldiruthenium and its Derivatives : Efficient Light Energy Storage Devices,” Journal of the American Chemical Society, **119**, pp. 6757–6773.

[103] Zhu B., Miljanić O. Š., Vollhardt K. P., and West M. J., 2005, “Synthesis of 2,2′,3,3′-Tetramethyl- and 2,2′,3,3′-Tetra- tert -butylfulvalene: Attractive Platforms for Dinuclear

Transition Metal Fragments, as Exemplified by (η 5 : η 5 -2,2′,3,3′- t -Bu 4 C 10 H 4)M 2 (CO) n (M = Fe, Ru, Os, Mo) and First X-ray Crys," Synthesis, **2**(19), pp. 3373–3379.

[104] Kanai Y., Srinivasan V., Meier S. K., Vollhardt K. P. C., and Grossman J. C., 2010, "Mechanism of Thermal Reversal of the (fulvalene)tetracarbonyldiruthenium Photoisomerization: Toward Molecular Solar-Thermal Energy Storage," Angewandte Chemie (International ed. in English), **122**(47), pp. 9110–9113.

[105] Harpham M. R., Nguyen S. C., Hou Z., Grossman J. C., Harris C. B., Mara M. W., Stickrath A. B., Kanai Y., Kolpak A. M., Lee D., Liu D.-J., Lomont J. P., Moth-Poulsen K., Vinokurov N., Chen L. X., and Vollhardt K. P. C., 2012, "X-ray Transient Absorption and Picosecond IR Spectroscopy of Fulvalene(tetracarbonyl)diruthenium on Photoexcitation.," Angewandte Chemie (International ed. in English), **51**(31), pp. 1–6.

[106] Meier S. K., 2009, Fulvalene Diruthenium Tetracarbonyl Complexes as Photochemical Energy Storage Devices, Berkeley.

[107] Gil A., Medrano M., Martorell I., Lázaro A., Dolado P., Zalba B., and Cabeza L. F., 2010, "State of the Art on High Temperature Thermal Energy Storage for Power Generation. Part 1—Concepts, Materials and Modellization," Renewable and Sustainable Energy Reviews, **14**(1), pp. 31–55.

[108] Carey V. P., 1999, Statistical Thermodynamics and Microscale Thermophysics, Cambridge University Press, Cambridge.

[109] Israelachvili J., 1991, Intermolecular & Surface Forces, Academic Press, London.

[110] Wenzel R. N., 1936, "Resistance of Solid Surfaces to Wetting by Water," Industrial and Engineering Chemistry, **28**(8), pp. 988–994.

[111] Cassie B. D., and Baxter S., 1944, "Wettability of Porous Surfaces," Trans. Faraday Soc., **40**(5), pp. 546–551.

[112] Plawsky J. L., Ojha M., Chatterjee A., and Wayner P. C., 2008, "Review of the Effects of Surface Topography, Surface Chemistry, and Fluid Physics on Evaporation at the Contact Line," Chemical Engineering Communications, **196**(5), pp. 658–696.

[113] Ojha M., Chatterjee A., Dalakos G., Wayner P. C., and Plawsky J. L., 2010, "Role of Solid Surface Structure on Evaporative Phase Change from a Completely Wetting Corner Meniscus," Physics of Fluids, **22**(5), p. 052101.

[114] Cramers C. A., Rijks J. A., and Schutjes C. P. M., 1981, "Factors Determining Flow Rate in Chromatographic Columns," Fried. Vieweg & Sohn Verlagsgesellschaft mbH, **14**(7), pp. 439–444.

[115] Kays W. M., and London A. L., 1984, Compact Heat Exchangers, McGraw-Hill Book Company, New York City.

[116] Hsu Y. Y., 1962, "On the Size Range of Active Nucleation Cavities on a Heating Surface," Journal of Heat Transfer, pp. 207–213.

[117] Rohsenow W. M., 1951, A Method of Correlating Heat Transfer Data for Surface Boiling of Liquids, Cambridge.

[118] Haramura Y., and Katto Y., 1983, "A New Hydrodynamic Model of Critical Heat Flux, Applicable Widely to both Pool and Forced Convection Boiling on Submerged Bodies in Saturated Liquids," International Journal of Heat and Mass Transfer, **26**(3), pp. 389–399.

[119] Kandlikar S. G., 2001, "A Theoretical Model to Predict Pool Boiling CHF Incorporating Effects of Contact Angle and Orientation," Journal of Heat Transfer, **123**(6), p. 1071.

[120] Liaw S. P., and Dhir V. K., 1989, "Void Fraction Measurements During Saturated Pool Boiling of Water on Partially Wetted Vertical Surfaces," Journal of Heat Transfer, **111**, p. 731.

[121] Lienhard J. H., Dhir V. K., and Riherd D. M., 1973, "Peak Pool Boiling Heat -Flux Measurements on Finite Horizontal Plates," Journal of Heat Transfer, pp. 477–482.

[122] Khrustalev D., and Faghri A., 1995, "Heat Transfer in the Inverted Meniscus Type Evaporator at High Heat Fluxes," International Journal of Heat and Mass Transfer, **38**(16), pp. 3091–3101.

[123] Bretherton F. P., 1961, "The Motion of Long Bubbles in Tubes," Journal of Fluid Mechanics, **10**, pp. 166–188.

[124] Ajaev V. S., and Homsy G. M., 2006, "Modeling Shapes and Dynamics of Confined Bubbles," Annual Review of Fluid Mechanics, **38**(1), pp. 277–307.

[125] Ranjan R., Murthy J. Y., and Garimella S. V., 2009, "Numerical Study of Evaporation Heat Transfer From the Liquid-Vapor Interface in Wick Microstructures," Volume 9: Heat Transfer, Fluid Flows, and Thermal Systems, Parts A, B and C, pp. 1323–1333.

[126] Rainey K. N., and You S. M., 2001, "Effects of Heater Size and Orientation on Pool Boiling Heat Transfer from Microporous Coated Surfaces," International Journal of Heat and Mass Transfer, **44**, pp. 2589–2599.

[127] Ahn H. S., and Kim M. H., 2012, "Visualization Study of Critical Heat Flux Mechanism on a Small and Horizontal Copper Heater," International Journal of Multiphase Flow, **41**, pp. 1–12.

[128] Kim S. J., Bang I. C., Buongiorno J., and Hu L. W., 2007, "Surface Wettability Change During Pool Boiling of Nanofluids and its Fffect on Critical Heat Flux," International Journal of Heat and Mass Transfer, **50**, pp. 4105–4116.

[129] Betz A. R., Xu J., Qiu H., and Attinger D., 2010, "Do Surfaces with Mixed Hydrophilic and Hydrophobic Areas Enhance Pool Boiling?," Applied Physics Letters, **97**(14).

[130] You S. M., Simon T. W., Bar-cohen A., and Member S., 1992, "A Technique for Enhancing Boiling Heat Transfer with Application to Cooling of Electronic Equipment," IEEE Transactions on Components, Hybrids, and Manufacturing Technology, **15**(5), pp. 823–831.

[131] Chu R. C., Simons R. E., Ellsworth M. J., Schmidt R. R., and Cozzolino V., 2004, "Review of Cooling Technologies for Computer Products," IEEE Transactions on Device and Materials Reliability, **4**(4), pp. 568–585.

[132] Bar-Cohen A., "NEAR JUNCTION THERMAL TRANSPORT (NJTT)" [Online]. Available: http://www.darpa.mil/Our_Work/MTO/Programs/TMT/Near_Junction_Thermal_Transport_(NJTT).aspx.

[133] Lin S., Member S., Banerjee K., and Member S., 2008, "Cool Chips : Opportunities and Implications for Power and Thermal Management," IEEE Transactions on Electron Devices, **55**(1), pp. 245–255.

[134] Lin S.-C., Basu A., Keshavarzi A., De V., Mehrotra A., and Banerjee K., 2004, "Impact of Off-State Leakage Current on Elctromigration Design Rules for Nanometer Scale CMOSS Technologies," 42nd Annual International Reliability Physics Symposium, Phoenix, pp. 74–78.

[135] Shoji M., 2004, "Studies of Boiling Chaos: A Review," International Journal of Heat and Mass Transfer, **47**(6-7), pp. 1105–1128.

[136] Shoji M., and Takagi Y., 2001, "Bubbling Features from a Single Artificial Cavity," International Journal of Heat and Mass Transfer, **44**, pp. 2763–2776.

[137] Goyal A., Jaeger R. C., Bhavnani S. H., Ellis C. D., Phadke N. K., Azimi-Rashti M., and Goodling J. S., 1993, "Formation of Silicon Reentrant Cavity Heat Sinks Using Anisotropic Etching and Direct Wafer Bonding," IEEE Electron Device Letters, **14**(1), pp. 29–32.

[138] Phadke N. K., Bhavnani S. H., Goyal A., Jaeger R. C., and Goodling J. S., 1992, "Re-entrant Cavity Surface Enhancements for Immersion Cooling of Silicon Multichip Packages," IEEE Transactions on Components, Hybrids, and Manufacturing Technology, **15**(5), pp. 815–822.

[139] Baldwin C. S., Bhavnani S. H., Hall R., and Jaeger R. C., 1998, "Towards Optimizing Enhanced Surfaces for Passive Immersion Cooled Heat Sinks," InterSociety Conference on Thermal Phenomena, pp. 399–408.

[140] Chatpun S., Watanabe M., and Shoji M., 2004, "Nucleation Site Interaction in Pool Nucleate Boiling on a Heated Surface withTriple Artificial Cavities," International Journal of Heat and Mass Transfer, **47**(14-16), pp. 3583–3587.

[141] Calka A., and Judd R. L., 1985, "Some Aspects of the Interaction Among Nucleation Sites During Saturated Nucleate Boiling," International Journal of Heat and Mass Transfer, **28**(12), pp. 2331–2342.

[142] Peng K.-Q., Yan Y.-J., S-P G., and Zhu J., 2002, "Synthesis of Large-Area Silicon Nanowire Arrays via Self-Assembling Nanoelectrochemistry," Advanced Materials, **14**(16), pp. 1164–1167.

[143] Peng K., Yan Y., Gao S., and Zhu J., 2003, "Dendrite-Assisted Growth of Silicon Nanowires in Electroless Metal Deposition," Advanced Functional Materials, **13**(2), pp. 127–132.

[144] Chu K.-H., Enright R., and Wang E. N., 2012, "Structured Surfaces for Enhanced Pool Boiling Heat Transfer," Applied Physics Letters, **100**(24).

[145] Liter S. G., and Kaviany M., 2001, "Pool-Boiling CHF Enhancement by Modulated Porous-Layer Coating: Theory and Experiment," International Journal of Heat and Mass Transfer, **44**(22), pp. 4287–4311.

[146] Sangani A. S., and Acrivos A., 1982, "Slow Flow Past Periodic Arrays of Cylinders with Application to Heat Transfer," International Journal of Multiphase Flow, **8**(3), pp. 193–206.

[147] Xiao R., Enright R., and Wang E. N., 2010, "Prediction and Optimization of Liquid Propagation in Micropillar Arrays," Langmuir : the ACS journal of surfaces and colloids, **26**(19), pp. 15070–15075.

[148] Kenisarin M., and Mahkamov K., 2007, "Solar Energy Storage Using Phase Change Materials," Renewable and Sustainable Energy Reviews, **11**(9), pp. 1913–1965.

[149] Lindley D., 2010, "The Energy Storage Problem," Nature, **463**, pp. 18–20.

[150] Dresselhaus M. S., and Thomas I. L., 2001, "Alternative Energy Technologies," Nature, **414**(6861), pp. 332–7.

[151] Carroll A., and Somerville C., 2009, "Cellulosic Biofuels," Annual Review of Plant Biology, **60**, pp. 165–82.

[152] Tolman W. B., “Photochemistry and Ligand Substitution Chemistry of (Fulvalene)dirutheneum(tetracarbonyl),” University of California Berkeley.

[153] Moth-Poulsen K., Ćoso D., Börjesson K., Vinokurov N., Meier S. K., Majumdar A., Vollhardt K. P. C., and Segalman R. a., 2012, “Molecular Solar Thermal (MOST) Energy Storage and Release System,” Energy & Environmental Science, **5**(9), p. 8534.

[154] Hettiarachchii M. H. D., Golubovic M., Worek W. M., and Ikegami Y., 2007, “Optimum Design Criteria for an Organic Rankine Cycle Using Low-Temperature Geothermal Heat Sources,” Energy, **32**(9), pp. 1698–1706.

[155] Vinokurov N., 2010, New Organometallic Frames for Solar Energy Storage, Berkeley.

[156] Kolpak A. M., and Grossman J. C., 2011, “Azobenzene-Functionalized Carbon Nanotubes as High-Energy Density Solar Thermal Fuels,” Nano letters, **11**(8), pp. 3156–62.

[157] Zhu X.-G., Long S. P., and Ort D. R., 2008, “What is the Maximum Efficiency with which Photosynthesis can Convert Solar Energy into Biomass?,” Current opinion in biotechnology, **19**(2), pp. 153–9.

[158] Coleman H. W., and Steele W. G., 1999, Experimentation and Uncertainty Analysis for Engineers, John Wiley and Sons, New York City.

Appendix A

A1.1 Uncertainty and Error Analysis in Wick Structure Experiments

The primary error in measurement of heat transfer coefficient arises from uncertainty in temperature measurement and estimation of the heat losses to the ambient through non-evaporative heat transfer. The dominant mode of heat loss from the test sample is by conduction from the heater through the silicon wick substrate to the liquid reservoir. To estimate this, experiments are performed with a bare silicon surface with no wick structure and of the same dimensions as all other test samples, with power input and wick surface temperature measured as before. The power input to these bare samples reflects the losses associated with conduction through the wafer into the liquid reservoir, as well as radiation and convection heat transfer to the ambient at each measured substrate temperature. A schematic of the prepared test sample and a corresponding thermal resistance network are shown in Fig. A1.1 For a typical epoxy thickness of t_{epoxy} = 3 mm covering the back of the sample and a conservative estimate of the free convection heat transfer coefficient h_{conv} = 0.01 W/cm^2-K over a 1cm^2 area, the corresponding resistances turn out to be R_{epoxy} = 15 cm^2-K/W and R_{conv} = 100 cm^2-K/W. Therefore, the high evaporative/boiling thermal resistance of the wick always measured to be less than 0.5 cm^2-K/W, and a high thermal resistance through the back side indicate that the heat lost through the back surface is no more than 1 % of the input power for all the samples measured. Figure A1.1 also illustrates the placement of the thermocouples on the sample heater used to measure the average substrate temperature $T_{substrate}$. From experimentally obtained results, the overall heat loss Q_{loss} is correlated as a function of the substrate temperature as

$$Q_{loss}(W) = -4.5*10^{-5}(T_{substrate}-100)^3 + 3.5*10^{-3}(T_{substrate}-100)^2 + 3.32*10^{-2}(T_{substrate}-100) + 6.16*10^{-1} \quad \text{(A1)}.$$

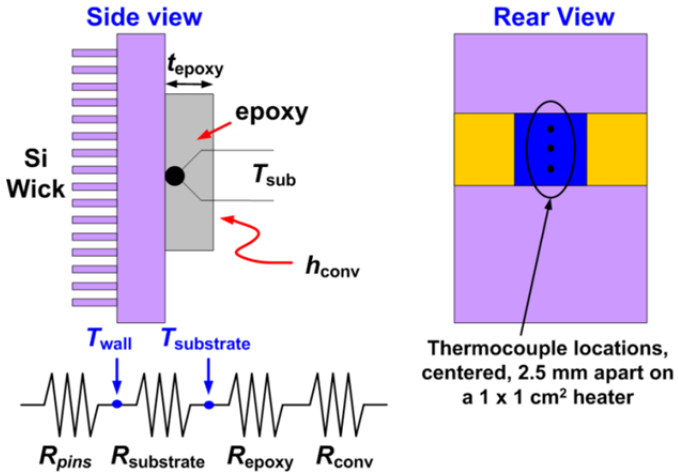

Fig. A1.1 Sketch of resistances to heat flow generated at the back surface of the wick and the placement of the thermocouples for the wall temperature measurement.

For the highest measured temperatures of 130 ^{o}C in the experiments, this value is about 3.5 W which is less than 3 % of the peak heat flow through the samples with a 1cm^2 heater size. Thus, the net power dissipated by phase change heat transfer is

$$Q = Q_{inp} - Q_{loss} \quad \text{(A2)},$$

where Q_{inp} is the electrical power applied to each sample. Here Q_{inp} is also adjusted for the power dissipated in the leads that connect the samples to the power supply.

For all measured samples, we implement standard procedures for uncertainty propagation,[158] where the uncertainty in a calculated quantity S is given by:

$$U_S = \sqrt{\sum_1^N \left(\left(\frac{\partial S}{\partial a_i} \right) U_{a_i} \right)^2} \qquad \text{(A3)},$$

Here S is a calculated parameter, U_S is the uncertainty in S, a_i is a measured parameter and U_{ai} is the uncertainty in parameter a_i. Based on standard procedures in linear regression analysis for estimating the error in slope and intercept of Eq. (A1), the uncertainty in estimating the heat loss (dQ_{loss}) is about 0.2 W for values of $T_{substrate}$ = 130 ^oC. The measured heat flux is defined as $q = Q/A_{heater}$. For large heat fluxes, q >100 W/cm^2 which are of particular interest, the total uncertainty in the heat flux measurement including uncertainty in heater area and heat losses is less than 3.9% for all samples with 1cm^2 heaters.

In order to obtain the heat transfer coefficient of the wick, the temperature at the base of the wick T_{wall} is calculated by accounting for the temperature drop through the silicon wafer using a one dimensional conduction model to yield:

$$T_{wall} = T_{sub} - q(t_{wafer} - H)/k_{Si} \qquad \text{(A4)},$$

Thus T_{wall} is defined in terms of the measured substrate temperature $T_{substrate}$, the total heat flux q corrected for heat losses, the overall wafer thickness t_{wafer}, the wick height H, and the thermal conductivity of silicon k_{Si}. The manufacturer-specified uncertainty in temperature measurement of the thermocouple was 0.6 K. The uncertainty in the temperature drop through the substrate is 3.1% of its value. At the highest heat fluxes, this drop can be up to 5.4 K, leading to uncertainties of 0.16 K. The total uncertainty in T_{wall} remains dominated by the manufacturer-specified uncertainty. The total measurement uncertainty in the heat transfer coefficient from Eq. (A3) from a single sample is estimated using Eq. (3.1). This ranges from values of no more than 12.2% at low superheats (~5K) to no more than 9.5 % at high superheats (> 15 K) for all samples with 1cm^2 heaters.

To verify the assumptions used in the uncertainty estimates, a finite element calculation is performed for representative values of power and temperature observed in the experiment. A rectangular plate of silicon, with area of 2 × 2 cm^2 and of thickness 525 μm is considered representing the entire sample containing the wick and substrate. The central area of 1 × 1 cm^2 on one side of the wafer has an imposed heat flux of 100 W/cm^2, while a heat transfer coefficient of 12 W/cm^2-K is imposed resembling a measured evaporative heat transfer on the coinciding central area on the other side containing the wick. Additional boundary conditions are chosen so that one end face of the plate of dimensions 2 cm × 525 μm is assumed to be maintained at 100 ^oC representing immersion in the large liquid reservoir. A free convection heat transfer coefficient of h_{conv} = 0.01 W/cm^2-K is imposed on all other faces of the plate for heat exchange with the ambient which is assumed to be at 100 ^oC. Figure A1.2 presents temperature contours on the substrate side of the wafer where $T_{substrate}$ is measured. A sharp temperature gradient is observed on one side of the wafer, which corresponds to conduction away from the wick area towards the liquid pool. Numerical integration of the resultant heat flux yields an overall heat

loss of ~3.2 W (3.2 % heat loss), which compares well with measured heat losses from bare silicon samples[8].

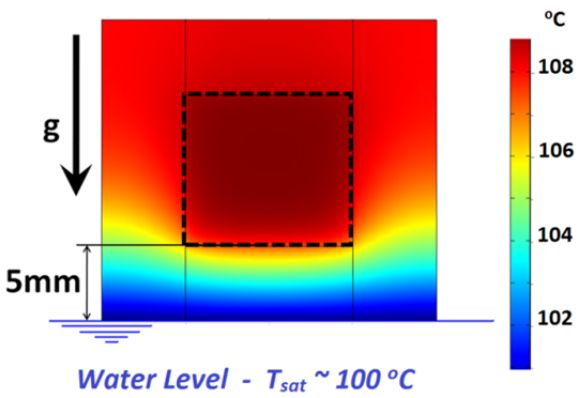

Fig. A1.2 Temperature contours (in °C) from finite element analysis for an imposed heat flux of 100 W/cm^2 and evaporation coefficient of 12 W/cm^2-K; here one end of wafer is assumed to be at the saturation temperature of water T_{sat}=100 °C. Black dashed line indicates relative size of the 1×1 cm^2 heater centered on a 2×2 cm^2 wick. These contours represent the measured substrate temperature field $T_{substrate}$.

A1.2 Uncertainty and Error Analysis in Pool Boiling Experiments

For pool boiling experiments, the uncertainty analysis approach is identical to that shown in Eq. (A3) in section A.1.1. Similarly, the measured heat power input is adjusted for heat losses via thermal spreading in the substrate, heat losses through the back of the sample, and heat losses in the electrical leads via joule heating.

The heat losses are verified by two approaches. In one, a finite element method is employed to determine heat losses due to thermal spreading numerically. Fig. A1.3 demonstrates temperature contours obtained from the finite element analysis. The boundary conditions are applied based on mimicking experimental conditions, until the temperature field mostly resembled that of actual experiments. Summation of all heat dissipated heat from edges other than the top surface indicate total heat loss of 1.8% for a heat flux q = 140 W/cm^2 applied at the back side of the sample of 1×1 cm^2 area with a heat transfer coefficient of h = 6.5 W/cm^2-K applied at the top surface.

[8] The overall heat loss to free convection and conduction estimated by Eq. (A2) and supported by the finite element models are adjusted for in all presented data. In this way we are able to isolate the total heat flux that is dissipated by evaporation/boiling within some uncertainty. Therefore, even though we cannot determine quantitatively the total area over which the bulk of the evaporation/boiling occurs, we can estimate the temperature T_{wall} at the pin fin array base using Eq. (A4). This way of defining the heat transfer coefficient includes the lateral heat spreading in the samples dissipated by evaporation/boiling.

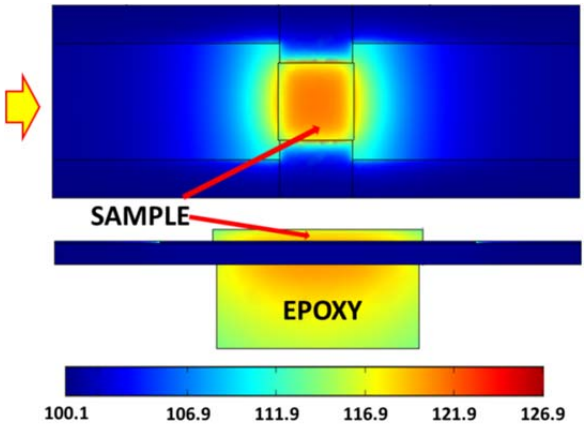

Fig. A1.3 Temperature contours (in ^{o}C) from finite element analysis for an imposed heat flux of 140 W/cm^2 and evaporation coefficient of 6.5 W/cm^2-K for a pool boiling experiment setup according to Fig. 4.3; here boundary conditions are chosen to mimic experimental conditions where the surrounding DI water T_{sat}=100 ^{o}C. The sample is is a 1×1 cm^2 square (top), and the thin rectangular part of the middle image as seen from a side view indicated by the yellow arrow.

The other method employed an actual pool boiling experiment on a nanowire sample where several thermocouples were placed a known distance from the edges aligned centrally with the sample in two directions as shown in Fig. A1.4. At each measured heat flux, a steady state temperature profile is used to approximate heat losses via conduction through the substrate. The results are correlated via a third order polynomial relation Eq. (A5) based on the substrate temperature $T_{\text{substrate}}$.

$$Q_{loss}(W) = 4.57\cdot 10^{-5} T_{substrate}^{3} - 2\cdot 10^{-3} * 10^{-3} T_{substrate}^{2} + 6.95\cdot 10^{-2} T_{substrate} + 5.38 \quad \text{(A5)}.$$

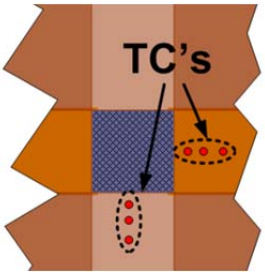

Fig. A1.4 Illustration of the placement of thermocouples (red dots) for heat loss measurements; thermocouples are placed ~2 mm apart, and a conduction model is implemented to estimate heat losses. The heat loss is correlated through a third order polynomial Eq. (A5) based on substrate temperature measured on the back of the actual sample tested. This was also true at lower heat fluxes.

A similar method was employed as in Fig. A1.1 to determine heat losses through the back side of the sample (through the epoxy, air gap, and Teflon block). This analysis indicated that at a heat flux of ~140W/cm^2, the heat lost through the back side was less than 0.25 % for all samples. At the defined heat flux and HTC, the finite element analysis (1.8 % Q_{loss}) agrees well with experimental measurements (2.24 % Q_{loss}). At lower heat fluxes (e.g. q = 21 W/cm^2 and h = 1.5 W/cm^2-K), the finite element analysis and experiments agree also with heat losses of ~14% and ~9.0% respectively. At lower heat fluxes more heat is lost at the heater edges.

Heat losses in the electrical leads are measured at each applied voltage V. The assembly of electrical junctions and all other components is illustrated in a measurement scheme via an electrical resistance model in Fig. A1.5. The voltage V supplied is measured via a multimeter of uncertainty ± 250mV as shown in the figure. The current I is taken from the power supply with the manufacturer provided uncertainty of ± 15mA. The power supplied is determined as $P = VI$. The uncertainty in the area of the sample is ± 0.002 cm^2. Prior to bonding the chip, the total electrical resistance of each lead including junctions is measured. This electrical resistance includes the copper wire lead $\acute{R}_{Cu\_l}$, the silver paste junction used to bond the wire to the copper tape $\acute{R}_{Cu\_t/l}$, the copper tape $\acute{R}_{Cu\_t}$, and the silver paste junction between the tape and sample $\acute{R}_{Cu\_t/s}$. For heat losses due to joule heating, the total resistance (both sides) comprised of leads and junctions never exceeded 0.5 Ω, while the overall resistance with leads and the sample was typically between 20 – 30 Ω indicating that losses due to joule heating never exceed 1 %. When combined, heat lost via joule heating, lost through the back side of the sample, and through the substrate determined from experiments agrees well with the numerical result from Fig. A1.3. All heat flux (q) and HTC (h) data presented in Chapter 3 is adjusted for these losses.

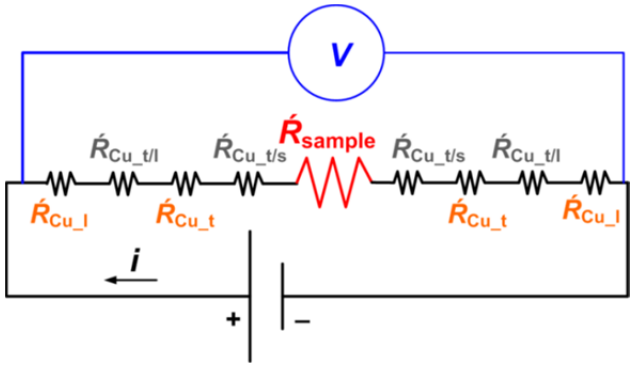

Fig. A1.5 Schematic of electrical resistances involved in heat flux measurements in boiling experiments. Here Ŕ is used to denote electrical resistance in order to distinguish it from thermal resistance discussed in other chapters.

After all heat losses in the sample of area A are accounted for in area normalized heat flux q, Eq. (A6) is employed to determine the wall temperature in contact with the liquid using a one dimensional conduction model

$$T_{wall} = T_{sub} - q\left[(t_{wafer} - H)/k_{Si} - t_{oxide}/k_{SiO_2}\right] \qquad \text{(A6).}$$

In this expression, the temperature drops through the silicon substrate and the grown silicon dioxide layer are accounted for. The wall temperature is then used to define the superheat ($\Delta T = T_{wall} - T_{sat}$) and the heat transfer coefficient as

$$h = \frac{Q/A_{heater}}{T_{wall} - T_{sat}} \qquad \text{(A.7).}$$

For pool boiling measurements the uncertainties in the measurements using Eq. (A3) in the heat flux $q = IV/A$ for high heat flux measurements e.g. V = 56.39V, I = 2.684A, and A = 1cm^2)

$$\frac{\delta q}{q} = \sqrt{\left(\frac{\delta V}{V}\right)^2 + \left(\frac{\delta I}{I}\right)^2 + \left(\frac{\delta A}{A}\right)^2} = 5.6\% \qquad \text{(A8),}$$

and the uncertainty in the calculated HTC is

$$\frac{\delta h}{h} = \sqrt{\left(\frac{\delta V}{V}\right)^2 + \left(\frac{\delta I}{I}\right)^2 + \left(\frac{\delta A}{A}\right)^2 + \left(\frac{\delta(\Delta T)}{\Delta T}\right)^2} = 7.8\% \qquad \text{(A9)}.$$

In the latter expression, the uncertainty in the superheat measurement ΔT is determined from the combined uncertainty in the thermocouple of 0.6K and at the specified conditions is found to be ~ 1K (0.76 %). In figures presented throughout Chapter 3, highest uncertainties are shown based on several measurement repeatability or experimental uncertainties as appropriate.

The rest of the content in this appendix is used to provide additional data or images to aid the content presented in preceding chapters.

A1.3 Repeatability of Measurements

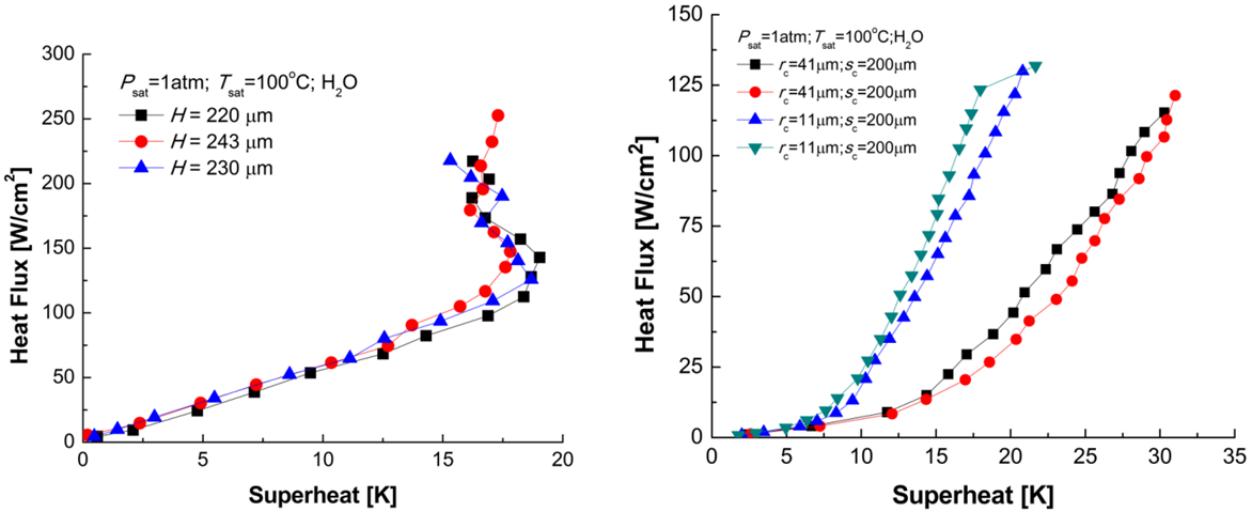

Fig. A1.6 (left) Repeatability of thin liquid film wick structure experiments of same geometry and similar depths. In these experiments nucleate boiling is clearly observed. p = 13.5 μm, d = 17.5 μm; (right) Repeatability of pool boiling experiments on horizontal nanowire + cavity surfaces of same geometry, cross sectional area (A=1cm^2), and similar cavity depths. Here H_{nw} = 35 μm and s_c = 200 μm.

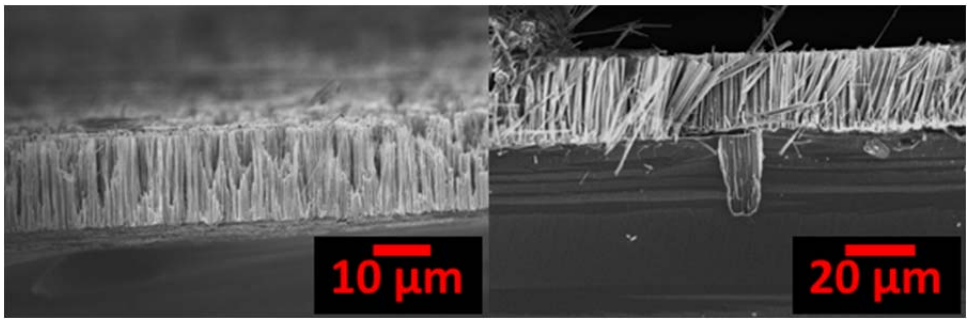

Fig A1.7 Additional SEM images of nanowire surfaces with and without cavities.

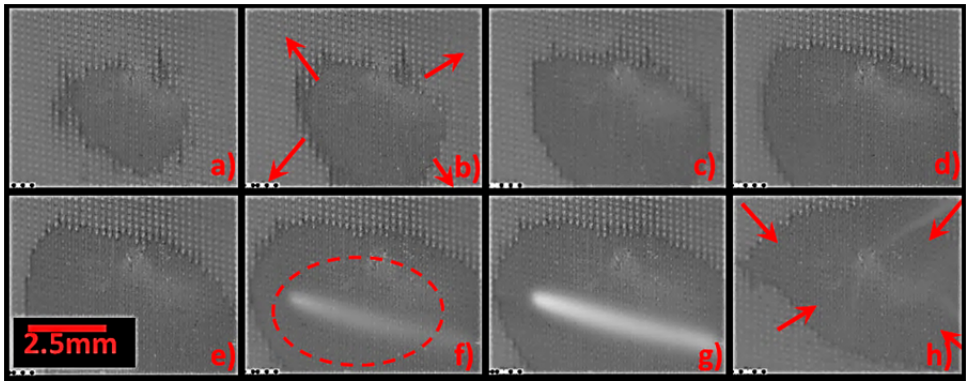

Fig A1.8 Illustration of burnout (a-h) and radial liquid recession over the heater area at CHF; circled bright region is the silicon sample getting red hot due to CHF and meltdown. Images are taken over a range of 1 s. (b) near CHF capillary pressure fails to resupply the heater and the liquid recedes; (f) onset of burnout evinced by a white region; once power is turned off (h) liquid is drawn back to the heater center by capillary pressure. This series of images is used for illustrative purposes only, and has same porosity considered in wicks of Chapters 3 and 4, but different parameters $d \approx 29$ µm, $p \approx 36$ µm, $w \approx 60$ µm, and $H \approx 165$ µm.

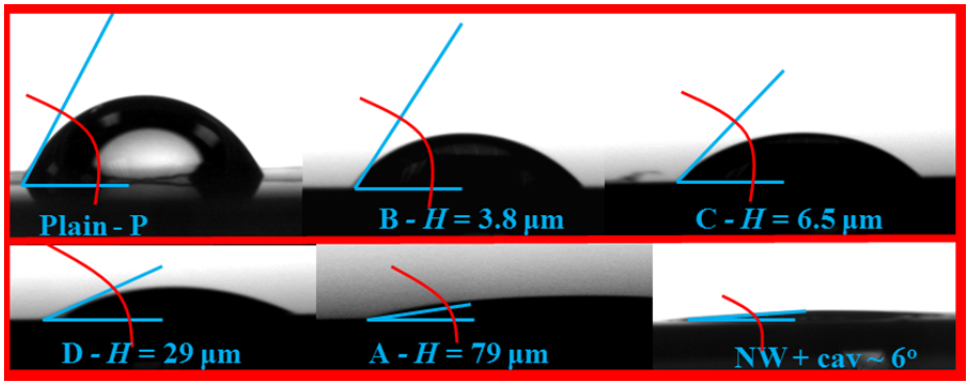

Fig A1.9 Contact Angles for pool boiling samples with angles summarized in Tables 4.1 and 4.2. All micropillar structures with $H > 80$ µm and most nanowire samples had $\theta_\alpha \approx 0^o$.

Table A1.1 Additional characteristics of wick structures of porosity $\phi = 0.79 \pm 0.03$ investigated in Chapter 3 (thermal resistances normalized to 1cm^2 area). Pin tops are excluded under the assumption that they are no covered by liquid during the experiment.

Micropillar d **[µm]**	**Wick depth** H **[µm]**	**Number of pins [thousands/cm^2]**	A_{pins} **(excluding pin tops) [cm^2]**	$R_{substrate}$ **[cm^2-K/W]**	R_{pins} **[cm^2-K /W]**
3.1	135	1344	23.2 ± 1.6	0.034	0.057
6.9	145	343	14.5 ± 1.0	0.033	0.061
13.5	56	116	4.2 ± 0.3	0.041	0.024
	145		9.3 ± 0.6	0.033	0.061
	207		13.1 ± 0.9	0.028	0.087
	243		14.4± 1.0	0.025	0.1
7.1	150	321	14.5 ± 1.0	0.033	0.060
15	149	93	9.1 ± 0.5	0.033	0.060
22.5	152	38	5.9 ± 0.4	0.032	0.061
29	158	22	4.1 ± 0.3	0.032	0.064

Table A1.2 Raw data of Fig. 4.8

Pool Boiling Experiments			
Depth [μm]	**Depth Variation [± μm]**	**CHF [W/cm^2]**	**CHF variation @ 90% confidence level [± W/cm^2]**
3.8	0.1	65.0	3.2
6.5	0.2	94.8	21.5
29.8	0.8	158.1	6.7
79.7	3.3	156.9	9.0
146.7	6.8	150.7	3.3
178.8	8.5	150.2	7.5
Plain Si	N/A	56.4	2.3
Thin Liquid Film Experiments			
Depth [μm]	**Depth Variation [± μm]**	**CHF [W/cm^2]**	**CHF variation based on Eq. (A8) [± W/cm^2]**
56	2.8	29.5	1.5
51	2.6	24.7	1.3
95	4.8	84.5	3.5
145	7.3	117.1	5.1
157	7.9	124.9	4.9
169	8.5	167.3	6.5
215	10.8	191.7	7.4
215	10.8	188.3	7.2
220	11.0	220.6	8.3
243	12.2	255.9	10.1
230	11.5	219.9	8.7